Doctoral Dissertation (Censored)

博士論文 (要約)

Structural insights into the mechanisms behind the maintenance of cellular homeostasis by membrane transport proteins via ATP.

(ATP を利用する膜タンパク質による細胞内恒常性維持機構の構造基盤の解明)

A Dissertation Submitted for the Degree of Doctor of Philosophy
December 2021

令和 3 年 12 月博士（理学）申請

Department of Biological Sciences, Graduate School of Science,
The University of Tokyo

東京大学大学院 理学系研究科

生物科学専攻

Atsuhiro Tomita

富田 篤弘

Abstract

The maintenance of cellular homeostasis by membrane transport proteins is one of the most important properties of living organisms. In the cellular homeostasis by membrane transport proteins, ATP plays a crucial role in two main ways: Intracellular modulatory element or energy to drive substrate transport. In this thesis, I focused on the mechanisms behind the maintenance of cellular homeostasis by membrane transport proteins via ATP.

Firstly, I focused on the Mg^{2+} channel MgtE which utilizes ATP as a modulatory element to maintain intracellular Mg^{2+} homeostasis. MgtE is a Mg^{2+} channel involved in the maintenance of intracellular Mg^{2+} homeostasis, whose gating is regulated by intracellular Mg^{2+} levels. In this thesis, I revealed that ATP binds to MgtE, regulating its Mg^{2+}-dependent gating by functional analysis. Moreover, I determined crystal structures of full length and cytosolic domain of MgtE-ATP complex. In the crystal structures, ATP binds to the intracellular CBS domain of MgtE. These structures, together with structure based mutational analysis revealed molecular basis of ATP-dependent modulation of MgtE in Mg^{2+} homeostasis.

Secondly, I focused on the lysosomal polyamine exporter ATP13A2, which utilizes the energy of ATP hydrolysis to drive polyamine transport into the cytosol. As the cytoplasmic polyamines maintain cellular homeostasis by chelating toxic metal cations, regulating transcriptional activity, and protecting DNA, cellular polyamine homeostasis maintained by ATP13A2 is crucial for life, and its dysfunction is associated with Alzheimer's disease and other neural degradation diseases. ATP13A2 belongs to the P5 subfamily of the P-type ATPase family, but its substrate recognition and transport mechanisms remain unknown. In this thesis, I determined cryo-electron microscopy (cryo-EM) structures of human ATP13A2 in complex with substrate polyamine. Polyamine was bound at the luminal tunnel and recognized through numerous electrostatic and π-cation interactions, explaining substrate specificity. Moreover, I determined the cryo-EM structures of human ATP13A2 in four different transport intermediates. These structures, together with molecular dynamics simulations revealed the structural coupling between the polyamine binding and the dephosphorylation. These findings revealed the distinct mechanism of P5B ATPases, thereby paving the way for neuroprotective therapy by activating ATP13A2.

Through this thesis, I revealed molecular mechanism of ATP modulated Mg^{2+} homeostasis by MgtE and ATP dependent SPM transport by ATP13A2 from the perspective of structural biology. These findings provide structural insights into the mechanisms behind the maintenance of cellular homeostasis by membrane transport proteins via ATP.

Contents

インターネット公表に関する共著者全員の同意が得られていないため、本章については非公開

インターネット公表に関する共著者全員の同意が得られていないため、本章については非公開

Abbreviations

Abbreviation	Full name
A600	Absorbance (measured at 600 nm)
ADP	Adenosine diphosphate
AlF_4^-	Aluminum tetrafluoride
AMPPCP	β,γ-Methyleneadenosine 5′-triphosphate
ATP	Adenosine triphosphate
BeF_3^-	Beryllium trifluoride
CHS	Cholesteryl hemisuccinate
Cryo-EM	Cryogenic electron microscopy
DDM	*n*-dodecyl β-D-maltoside
DNA	Deoxyribonucleic acid
DTT	Dithiothreitol
EGFP	Enhanced green fluorescent protein
FSC	Fourier shell correlation coefficient
FSEC	Fluorescence-detection size-exclusion chromatography
GDN	Glyco-diosgenin
GTP	Guanosine triphosphate
HEK293S cells	Human embryonic kidney 293S cell
HEPES	4-(2-Hydroxyethyl) piperazine-1-ethanesulfonic acid
HRV	Human rhinovirus
IPTG	Isopropyl β-D-1-thiogalactopyranoside
ITC	Isothermal titration calorimetry
LB	Luria-Bertani
LMNG	Lauryl maltose neopentyl glycol
Ni-NTA	Nickel-nitrilotriacetic acid
NTM	*n*-nonyl-β-D-thiomaltopyranoside
MES	2-(N-morpholino)ethanesulfonic acid
MD simulation	Molecular dynamics simulation
PEG	Polyethylene glycol
PMSF	Phenylmethylsulfonyl fluoride
RMSD	Root mean square deviation
RMSF	Root mean square fluctuation
ROS	Reactive oxygen species
SERCA	Sarco-endoplasmic reticulum Ca^{2+}-ATPase
SPM	Spermine
TEV	Tobacco etch virus
Tris	Tris(hydroxymethyl)aminomethane

Chapter 1 General introduction

1.1 Cellular homeostasis

The maintenance of intracellular homeostasis is one of the most important properties of living organisms, and all life maintain a constant intracellular environment by interacting with the environment inside and outside the cell[1]. Membrane transport proteins play a crucial role in the maintenance of cellular homeostasis by transporting substrates across lipid bilayer[2–4].

Membrane transporters are classified into pumps, transporters, and channels according to the mode of transport of substrates (Figure 1-1). Pumps actively transport substrates against its concentration gradient formed across the lipid bilayer utilizing energy from various sources including ATP hydrolysis, light excitation[5]. Both transporters and channels use substrate concentration gradients as a driving force for substrate transport[6]. Transporters permeate substrates by undergoing structural changes involving multiple steps[7]. On the other hand, the channel can be closed or open, and in the open state, it forms a small pore that penetrates the lipid bilayer and transports the substrate without undergoing major structural changes. Reflecting the scale of structural change, the transport rate of substrates is reported to be 10^3–10^4 per second for transporters and 10^6–10^8 per second for channels, channels could transport substrates faster than transporters[6].

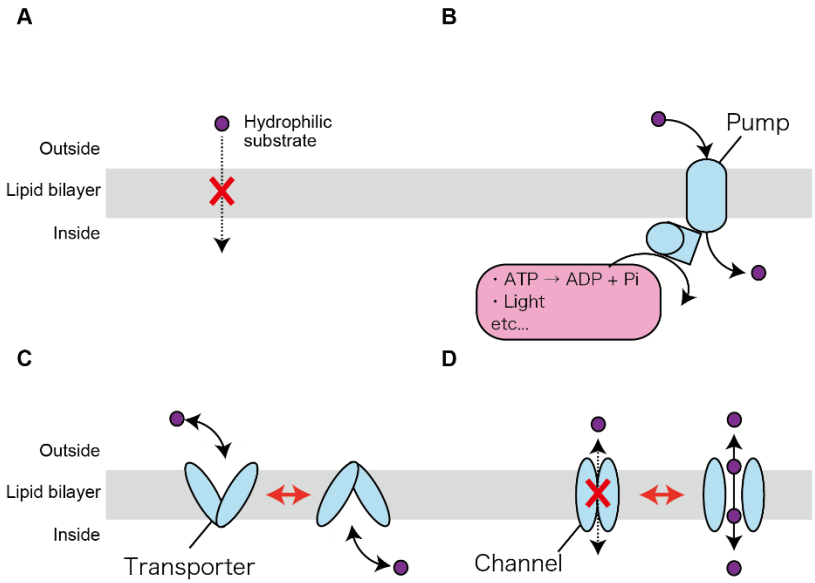

Figure 1-1 | Classification of membrane transport proteins

(**A**) Hydrophilic substrates cannot penetrate the lipid bilayer directly. (**B**) Pumps actively transport substrate using the energy from various sources including ATP hydrolysis, light excitation. (**C**) Transporters permeate substrates by undergoing structural changes involving multiple steps called altering access mechanism. (**D**) channels permeate the substrates without undergoing major structural changes.

1.2 Cellular homeostasis and adenosine triphosphate (ATP)

ATP plays a crucial role in many biological processes by interacting with proteins in the cell. In the following, I will describe the chemical and biological properties of ATP, and relationship between ATP and the maintenance of intracellular homeostasis by membrane transport proteins.

1.2.1 Chemical and biological property of ATP

ATP is an organic compound consisting of an adenine ring with 9-nitrogen atoms attached to the 1′ carbon atom of sugar (ribose) and triphosphate group attached to the 5′ carbon atom of sugar (Figure1-2). The three phosphate groups are called alpha (α), beta (β), and gamma (γ), in order of proximity to the 5′ carbon atom of sugar. Since ATP has chelating phosphate groups, it binds strongly to metal ions. In particular, ATP binds strongly to Mg^{2+}, which is the most abundant divalent cations in the cell[8]. Therefore, ATP exists in the cell mainly as a complex with Mg^{2+} bound to the phosphate oxygen center[8–10]. ATP exists stably in aqueous solution at pH 6.8-7.4, and ATP is rapidly hydrolyzed to ADP and phosphate under acidic conditions. The hydrolysis and transfer of the phosphate group of ATP are energy releasing reactions that involve in decrease in the net free energy. For such reasons, P-O-P bonds are often referred to as high-energy bonds[11]. The hydrolysis of ATP into ADP and inorganic phosphate releases 36-38 kJ/mol of free energy at a standard state of 1M ATP, 1M ADP, and 1M phosphate[12].

From a biological point of view, ATP is essential compound for all living cells and maintenance of ATP homeostasis is crucial of life. All living cells have mechanism to maintain concentration of ATP in the range of 1–10 mM, with a normal ratio of ATP/ADP of approximately 5–10 (Figure 1-3)[13–20].

In bacteria and eukaryotes, ATP is synthesized mainly by F-type ATPase, while ATP is synthesized mainly by A-type ATPase in archaea. Both F-type ATPase and A-type ATPase share similar structures[21–25]. F-type and A-type ATPases catalyze the synthesis of ATP from ADP and inorganic phosphate utilizing the energy of an electrochemical gradient of proton or Na^+ (refs [21–25]) (Figure 1-3).

The electrochemical potential of protons and Na^+ is formed by the active transport of protons and Na^+. The pathway of formation of the electrochemical potential differs depending on the species. The electrochemical potential is formed mainly by following three pathways.

Active transport of protons by the respiratory-chain enzymes of mitochondria, inner membrane of aerobic bacteria and aerobic archaea. Active transport of protons by the light-driven proton pumps from plants or phototrophic bacteria. Active transport of Na^+ utilizing the energy of decarboxylation reactions in some anaerobic bacteria[21–25] (Figure 1-3).

Intracellular ATP maintained at such a high concentration is utilized by membrane transporters in two main ways: Intracellular modulatory element of channels/transporters/pumps or energy to drive substrate transport by pumps.

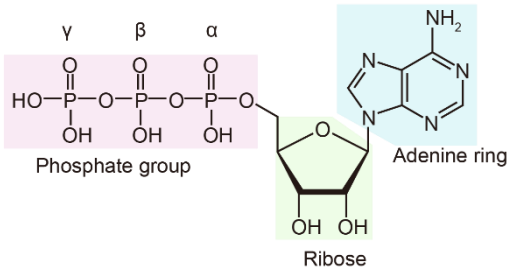

Figure 1-2 | Chemical property of ATP

The chemical structure of ATP is illustrated for each component. Adenine ring is colored blue, ribose is colored green, phosphate group is colored red. The three phosphate groups are called α-, β-, and γ-phosphate, respectively, as shown in the figure.

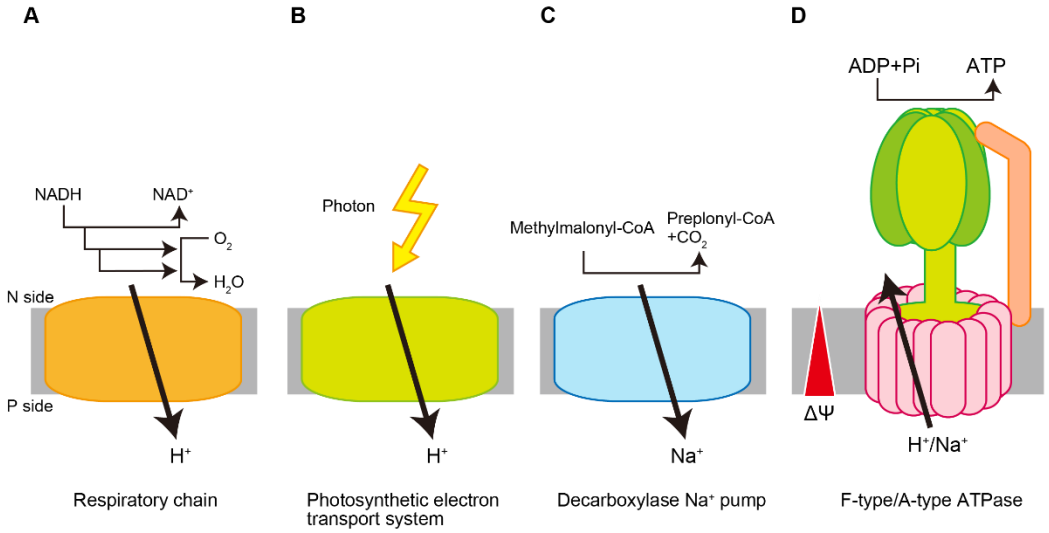

Figure 1-3 | ATP synthesis in all kingdoms of life

The major ATP synthesis pathways from prokaryotes to eukaryotes are illustrated. Electro chemical gradients of protons and Na^+ are stored (**A–C**) and ATP is finally synthesized by F-type or A-type ATPases (**D**). (**A**) In the eukaryotes and aerobic bacteria and archaea, proton gradient is stored by respiration chain in mitochondrial inner membrane or prokaryotic inner cell membrane. (**B**) In the plants and phototrophic bacteria, proton gradient is stored by photosynthetic electron transport system in the thylakoid membrane or bacterial inner cell membrane. (**C**) In the anaerobic bacteria, Na^+ gradient is stored by decarboxylase Na^+ pump in the bacterial inner cell membrane. The N side indicates the negatively charged side of the membrane, and the P side indicates the positively charged side of the membrane. Δψ represents stored electrochemical potential.

1.3 ATP as an Intracellular modulatory element of channels and transporters

ATP serves as an intracellular modulatory element in some proteins, regulating functional role to maintain intracellular conditions suitable for life. In the study of ATP-mediated functional modulation, proteins containing CBS domains have long been studied.

1.3.1 CBS domain

CBS domain was first reported as a conserved sequence in 1997 and the name "CBS domain" is derived from Cystathionine Beta Synthase (CBS), one of the proteins it is found in[26]. CBS domain is an evolutionarily conserved nucleic acid binding domain widely spread among prokaryotes and eukaryotes[26]. CBS domain is found in enzymes and membrane transport proteins. CBS domain in the enzymes and membrane transport proteins regulates enzyme and substrate transport activities in response to binding nucleic acids including ATP[27]. CBS domain is composed of a β-α-β-α secondary structure pattern and exists in pairs (CBS1, CBS2) within the protein sequence, with each pair tightly bound together in a pseudo-dimeric sequence via the β-sheet[27–29] (Figure 1-4A). The function and structure of membrane proteins with CBS domains have long been studied for the Cl^- channels/transporters ClC family and the Mg^{2+} channel MgtE[30–32]. ClC-5 is a Cl^- transporter responsible for maintenance of pH and ion homeostasis in the endosome[33,34]. Functional and structural analyses revealed that nucleotides including ATP regulates Cl^- permeability of ClC-5[30,35] (Figure 1-4). MgtE is Mg^{2+} channel responsible for intracellular Mg^{2+} homeostasis. Similar to ClC-5, the functional role of the CBS domain in MgtE has been well studied. However, the functional role of the CBS domain in MgtE is different to the ClC-5. In the next section, I will describe the mechanism of Mg^{2+} homeostasis by MgtE regulated by CBS domain, and remaining issues about Mg^{2+} homeostasis by MgtE.

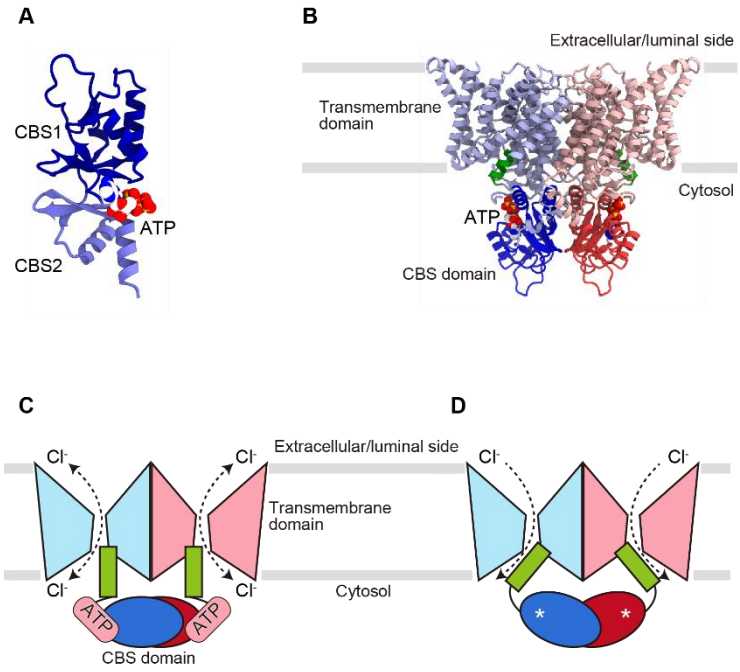

Figure 1-4 | CBS domain regulates Cl^- permeability of ClC-5

(**A**) Crystal structure of CBS domain of ClC-5 in complex with ATP (PDB ID: 2J9L). ATP was bound between CBS1 and CBS2. (**B**) I modeled the structure of ATP-bound ClC-5 as proposed by previous study[30]. The Cryo-EM structure of chicken CLC-7 (PDB ID: 7JM6) was used to model the transmembrane domain[36]. (**C-D**) Cl^- permeation mechanism of ClC-5 mutant regulated by binding of ATP to the CBS domain as proposed by mutational analysis of ClC-5. In the ATP-bound state, the conformation is stabilized to allow Cl^- ions flow equally in both directions (**C**). In the mutant with compromised ATP-binding ability, CBS domains induce conformational change of the transmembrane domain through the regulatory helix (colored green), reducing the flow of Cl^- ions from the cytosolic side (**D**).

1.3.2 Mg^{2+} homeostasis by MgtE

Mg^{2+} is the most abundant divalent cation in the cell and an essential element for numerous physiological activities, such as catalysis by hundreds of enzymes, cell membrane stabilization, and ATP utilization[37,38]. Therefore, abnormalities in Mg^{2+} homeostasis are associated with various diseases including diabetes, obesity, and cardiovascular disease, and maintenance of Mg^{2+} homeostasis by Mg^{2+} channels and transporters is crucial for life[3,39,40].

MgtE is a Mg^{2+} channel widely distributed from prokaryotes to eukaryotes[41]. The bacterial MgtE channels are highly selective for Mg^{2+}, and are involved in the maintenance of the intracellular Mg^{2+} homeostasis[42,43]. Likewise, the eukaryotic homologs of MgtE, the solute carrier 41 (SLC41) family proteins, also permeate Mg^{2+} ions and are implicated in Mg^{2+} homeostasis[44–47]. For the MgtE and SLC41 family proteins play crucial role in Mg^{2+} homeostasis, several mutations in the SLC41 genes are related to Parkinson's disease[48], diabetes[49], and nephronophthisis[50].

Previous studies reported the crystal structures of the full-length Thermus thermophilus MgtE (TtMgtE, referred to simply as MgtE in the following) in the presence of Mg^{2+}, its transmembrane domain in the presence of Mg^{2+}, and its cytosolic domain in the presence and absence of Mg^{2+} (refs. [31,43,51]) (Figure 1-5). The full-length structure in the presence of Mg^{2+} revealed that MgtE forms a homodimer, consisting of five transmembrane helices, one plug helix, and the cytosolic region composed of the N-terminal domain and the tandemly repeated CBS domains (Figure1-5A). Structural comparison of the Mg^{2+}-bound and Mg^{2+}-free cytosolic domain structures, together with molecular dynamic simulations[32], revealed that Mg^{2+} binding to the cytosolic domain stabilizes the closed conformation of MgtE, suggesting a Mg^{2+} homeostasis mechanism in which the MgtE cytosolic domain acts as a Mg^{2+} sensor to regulate the Mg^{2+} influx (Figure1-5B-D). Consistently, the subsequent electrophysiological analysis demonstrated that intracellular Mg^{2+} binding to the cytosolic domain of MgtE inhibited the channel opening of MgtE[43].

However, in the previously reported electrophysiological analysis of MgtE, the threshold of intracellular Mg^{2+} for the channel gating was between 5 and 10 mM, which is much higher than the physiological intracellular Mg^{2+} concentration (~1 mM)[43,52]. Therefore, this discrepancy implied the existence of additional regulatory factors for the Mg^{2+}-dependent channel gating of MgtE under physiological conditions.

The CBS domain in the cytosolic domain of MgtE possesses regulatory sites for Mg^{2+} (refs. [31,43]) and includes a probable nucleotide binding sequence to regulate the activity of associated enzymes or transporters. Therefore, the CBS domain of MgtE may utilize ATP or other nucleotides as modulatory element to regulate channel gating, such as the human ClC-5 Cl^- transporter which regulates the Cl^- permeability in response to the binding of ATP or other nucleotides[30]. However, it remains unclear whether and how Mg^{2+} channels are modulated by ATP

or other nucleotides for Mg^{2+} homeostasis, further functional and structural analysis of MgtE in complex with ATP or other nucleotides are needed.

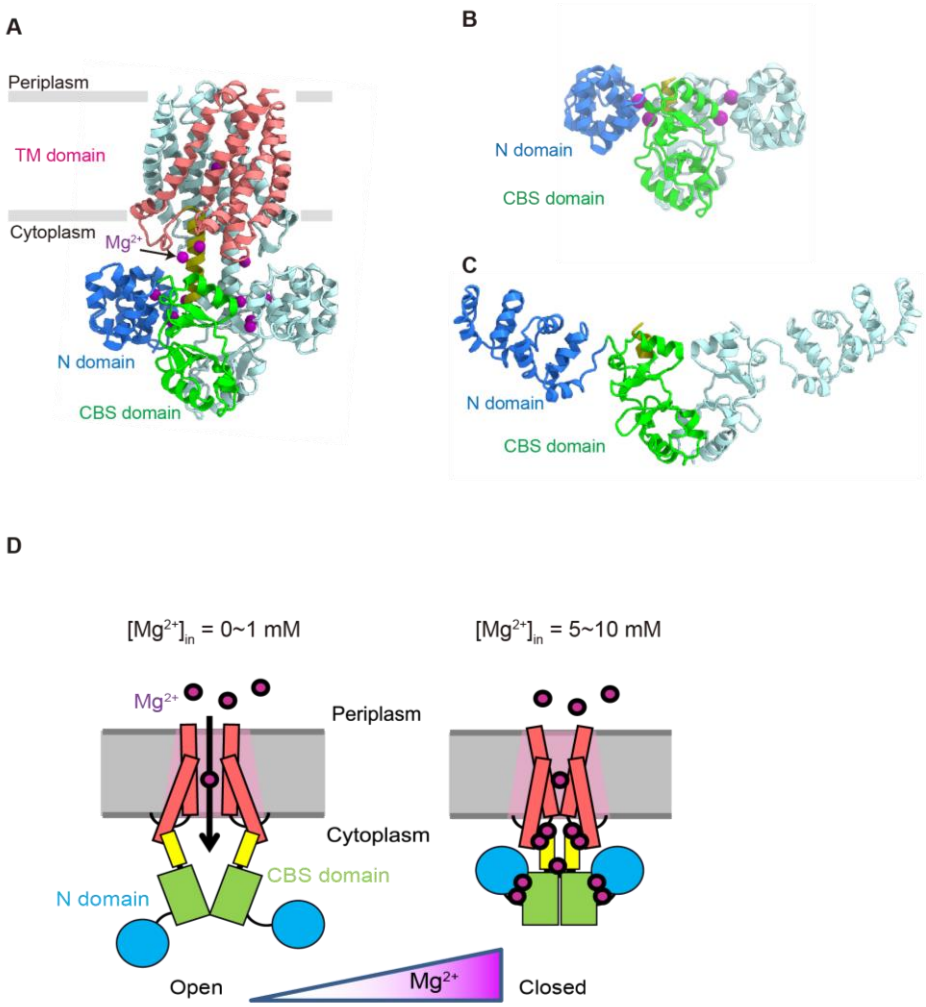

Figure 1-5 | Crystal structures of MgtE and Mg^{2+} sensing mechanism by MgtE

(**A-C**) Crystal structure of full length MgtE in the presence of Mg^{2+} (**A**), cytosolic domain of MgtE in the presence of Mg^{2+} (**B**), cytosolic domain of MgtE in the absence of Mg^{2+} (**C**). (**D**) Mg^{2+} sensing mechanism proposed by a comparative analysis of the Mg^{2+}-bound and Mg^{2+}-free cytosolic domain structures, together with molecular dynamic simulations. Further electrophysiological analysis proved Mg^{2+} binding to the cytosolic domain stabilizes the closed conformation of MgtE when $[Mg^{2+}]_{in}$ = 5–10 mM.

1.4 ATP as an energy to drive substrate transport by pumps

One of the well-known roles of ATP in the cell is driving active transport of substrates by pumps via serving energy of ATP hydrolysis. The active transport of substrates using ATP hydrolysis is mainly conducted by ABC transporters, V-type ATPases, and P-type ATPases[53–56].

ABC transporters export toxic compounds and import nutrients to maintain cellular environment suitable for life[53]. V-type ATPases are mainly expressed in acidic intracellular organelles, such as lysosomes, and use the energy from ATP hydrolysis to uptake protons to maintain intracellular organelles in acidic conditions[54]. P-type ATPases transport various substrates into and out of the cell, contributing to the maintenance of intracellular homeostasis[56,57]. I will describe the biological property and molecular mechanism of the P-type ATPases in detail below.

1.4.1 P-type ATPase superfamily

The P type ATPase super family is a large group of ion and lipid pump widely conserved among bacteria, archaea, and eukaryotes[57].

The first report of a P-type ATPase was the discovery of Na^+/K^+ ATPase in 1957, and Dr. Jens Christian Skou was awarded the Nobel Prize in 1977 for the discovery of Na^+/K^+ ATPase[58].

P-type ATPases are composed of transmembrane domain (TM domain) with at least six transmembrane helices (M1-M6) and ATPase domain consist of Nucleotide binding domain (N domain), Phosphorylation domain (P domain) and Actuator domain (A domain) [56,57,59] (Figure 1-6). Some P-type ATPase have additional regulatory element at N- and C-termini[60–62].

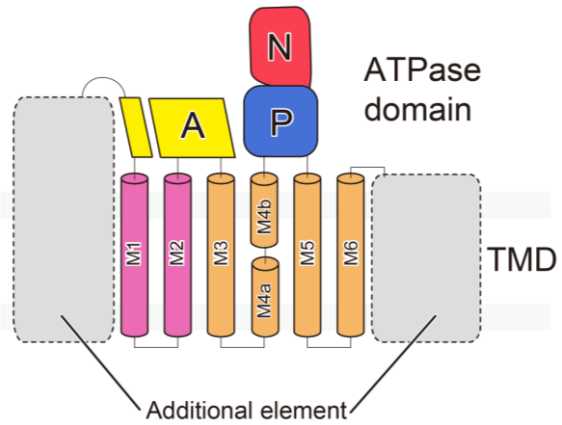

Figure 1-6 | Topology diagram of common domain architecture of P-type ATPases

Conserved domains and transmembrane (TM) helices are schematically illustrated. In the cytoplasmic regions, the A, N, and P domains, are colored yellow, red, blue, respectively. M1–M2 and M3–M6 are pink and orange, respectively. Additional elements at the N- and C-termini are indicated in gray.

1.4.2 Transport mechanism of P-type ATPase

The name "P-type ATPase" is derived from its substrate transport mechanism. P-type ATPases utilize ATP for autophosphorylation (P) and following dephosphorylation to transport the substrate, hence the name P-type ATPase[59,63]. The typical transport mechanism of P-type ATPase is described by Post-Albers scheme[64,65]. I will illustrate the Post-Albers scheme using the most well-studied SERCA as a representative. In this cycle, ATP and Ca^{2+} dependent autophosphorylation and proton dependent dephosphorylation alternately induce the transition of the different enzymatic states, referred as E1 and E2, and consequently allow substrate transport[66–71] (Figure1-7).

In a series of cycles, kinking of the M4 helix and large movements of the M1-2 helix are known to play a major role in substrate transport in P-type ATPases in general. The phosphoreceptor is the carbonyl oxygen of aspartic acid in the DKTG motif, which is universally conserved in the P domain; dephosphorylation of the P domain occurs by direct hydrolysis with water molecule activated by the conserved TGES motif in the A domain[59] (Figure 1-7).

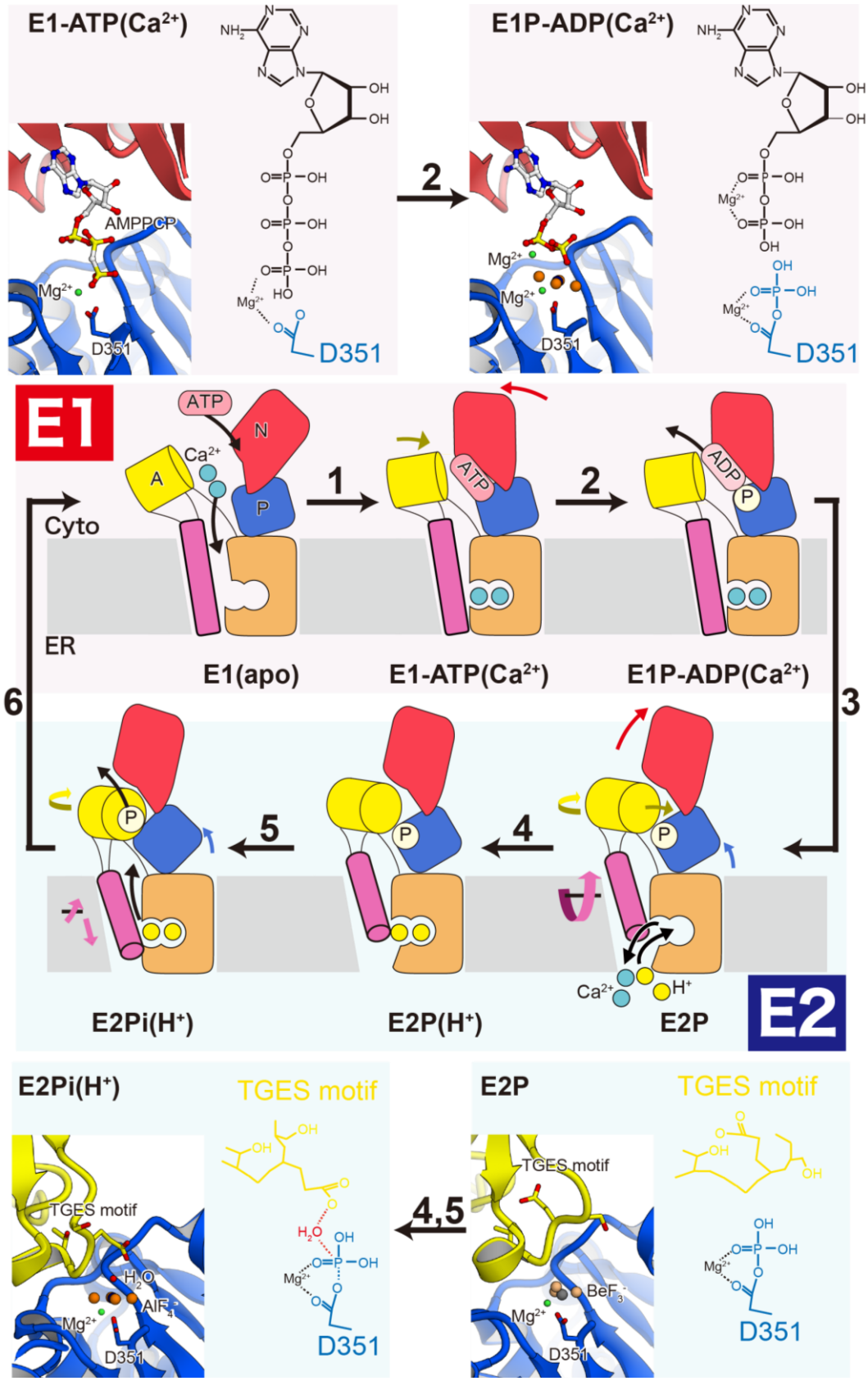

Figure 1-7 | Post-Albers scheme in SERCA (continued, see next page for caption)

Figure 1-7 | Post-Albers scheme in SERCA

A schematic picture of Post-Albers scheme in SERCA is shown. The crystal structures corresponding to the E1-ATP, E1P-ADP, E2P, E2Pi(H^+) states are captured using non-hydrolyzable analogs of ATP (AMPPCP), ADP+phosphate analog (ADP+AlF_4^-), covalently-bonded phosphate analog (BeF_3^-), phosphate analog (AlF_4^-) respectively. For intermediates in the phosphorylation and dephosphorylation processes, the active sites of the ATPase domain in the crystal structures and the corresponding structural formulas are shown in the figure. A step-by-step overview of the transportation cycle follows the process below.

1. The cycle starts in the E1(apo) state. Ca^{2+} binds to the TM domain, ATP binds to the N domain to bridge the N and P domains.
2. Gamma-phosphate of ATP is transferred to conserved aspartate in the P domain.
3. ADP is released and the A domain moves closer to the P domain. The entire TM domain moves significantly according to the movement of the ATPase domain, resulting the luminal gate opens to release Ca^{2+}.
4. The proton binds.
5. Proton binding to the luminal gate facilitates closing of the luminal gate. A domain rotates slightly according to the closing of the luminal gate, resulting dephosphorylation of the P domain by direct hydrolysis with water molecule activated by the conserved TGES motif in the A domain.
6. Phosphate and the proton are released to return to the E1(apo) state.

1.4.2 Diversity in P-type ATPase superfamily

Based on many biochemical, genetic, and bioinformatic studies of the P-type ATPases until recently, P-type ATPases are divided into five classes, P1-P5 ATPases[72].

The P1–P3 ATPases are well studied subtypes and generally transport metal cations and protons. P1 ATPases transport heavy metals and their structures have been reported previously[73,74]. The P2 ATPases are the most studied subtype and transport metal cation and proton as substrate[70,75–82]. The P2 subtype includes a sarcoplasmic reticulum Ca^{2+} pump (SERCA)[70,75–77], Na^+/K^+-ATPase[78–81], and H^+/K^+-ATPase[82], and a considerable number of structural and biochemical studies have revealed their transport mechanism. P3 ATPases generally transport proton and Mg^{2+} and their structures have been reported previously[83–85].

The P4 and P5 ATPases have been recently identified as large substrate transporters, whose substrates are very different from those of P1–P3 ATPases. The molecular mechanisms of these "large substrate" P-type ATPases have been a long-standing question since their discovery. P4 ATPases transport lipids as substrate. Structural and biochemical analysis of P4 ATPases have revealed their unique mechanisms of lipid recognition and flipping[86–90]. P5 ATPases can be divided in two subclades, P5A and P5B, which have totally different physiological substrates. P5A ATPases probably catalyze the dislocation of incorrectly delivered peptides (α helix dislocase)[91]. Structural and biochemical analysis suggested substrate peptides recognition mechanisms unique to P5A ATPases[91]. For P5B ATPases, their substrates are unknown for long time. Among the P5B ATPases, ATP13A2 has been the most studied. Recently, biochemical and *in vivio* analysis reported ATP13A2 transports polyamines to maintain intracellular polyamine homeostasis[92]. I will describe importance and remaining issues of polyamine homeostasis by ATP13A2 in the next section.

1.4.3 Polyamine homeostasis by ATP13A2

Polyamines are essential organic compounds for various biological activities in all eukaryotes[93,94]. Among the various polyamine species, spermine (SPM) plays especially important roles in cells, such as interacting with nucleic acids to regulate transcriptional activity[95], stabilizing chromatin structure[96,97], and protecting DNA[98–100]. In addition, intracellular SPM protects cells from damages caused by toxic heavy metals and reactive oxygen species (ROS)[101–103]. Accordingly, abnormalities in cellular SPM homeostasis lead to various diseases, including neurological disorders[102]. Cellular SPM homeostasis is maintained by both the intracellular biosynthesis and SPM uptake from external sources[104]. As the amount of intracellular SPM biosynthesis decreases with aging, external SPM uptake is important for maintaining SPM homeostasis in the long run[104]. Recent biochemical and *in vivo* analysis reported that SPM is transported to lysosome via endocytosis in the SPM uptake pathway[92]. Furthermore, the P-type ATPase of type V subfamily

B (P5B-ATPase) ATP13A2 was identified as the lysosomal polyamine exporter that plays a crucial role in SPM release to the cytoplasm[92] (Figure 1-8). For such importance, several mutations in ATP13A2 are also associated with Parkinson's disease[105,106].

As described in the previous section, structural and biochemical property of P1–P5A ATPase have revealed recognition and transport mechanism of small ions and large hydrophobic substrates[70,73–91]. However, recognition and transport mechanism of large hydrophilic polyamines by ATP13A2 has remained unsolved due to lack of structural information of P5B ATPases including ATP13A2.

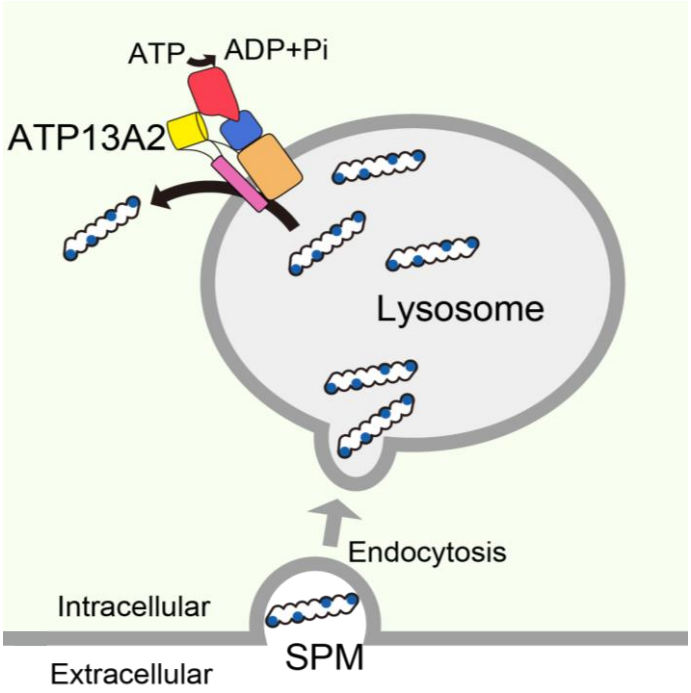

Figure 1-8 | Polyamine uptake by ATP13A2.

Schematic picture of SPM uptake by ATP13A2. In the SPM uptake, SPM is transported to lysosome via endocytosis. After uptake into the lysosome, SPM is exported to cytosol by ATP13A2, which belongs to the P-type ATPase superfamily.

1.5 Aim of the thesis

In this study, I aimed to obtain structural insights into the ATP-dependent cellular homeostasis mechanism through functional and structural analyses of the following two membrane transport proteins that utilize ATP in different ways. Specifically, I focused on ATP modulated Mg^{2+} homeostasis by MgtE, and ATP dependent SPM uptake by ATP13A2. These membrane transport proteins play important roles in cellular homeostasis in ATP dependent manner, but are poorly understood at the molecular levels. Therefore, I performed structural, functional, and computational studies on these membrane transport proteins, by using X-ray crystallography,

cryo-EM single particle analysis, biochemical and *in vivo* assays, and molecular dynamics simulation.

Chapter 2 X-ray crystallographic analysis of MgtE in complex with ATP

インターネット公表に関する共著者全員の同意が得られていないため、本章については非公開

Cryo-EM structures and MD simulations of ATP13A2 reveal transport mechanism of polyamines

3.1 Introduction

As discussed in Chapter 1, polyamines are essential organic compounds for life and spermine (SPM) plays especially important roles in cells[93,94,96–102]. the P-type ATPase of type V subfamily B (P5B-ATPase) ATP13A2 is the lysosomal polyamine exporter that plays a crucial role in SPM uptake to the cell[92]. ATP13A2 belongs to the P-type ATPase family, which is a major group of ion and lipid pumps conserved among all kingdom of life[133]. P-type ATPases are divided into 5 major subtypes (P1−P5), which share the similar architecture composed of cytoplasmic ATPase domains (N, P, and A-domains) and a transmembrane region, while their transport substrates and physiological roles vary among the subtypes[57]. As described in the Chapter 2, structural and biochemical property of P1–P5A ATPase have revealed recognition and transport mechanism of small ions and large hydrophobic substrates[70,73,82–91,74–81]. However, recognition and transport mechanism of large hydrophilic polyamines by ATP13A2 has remained unsolved due to lack of structural information of P5B ATPases including ATP13A2.

In this thesis, I determined the cryo-electron microscopy (cryo-EM) structures of human ATP13A2 under four different conditions: the non-hydrolyzable ATP analog AMPPCP-bound state (E1-ATP), the ADP-Pi (Pi: inorganic phosphate) analog AlF_4^--ADP-bound state (E1P-ADP), the BeF_3^--bound state in complex with spermine (E2P(SPM)), and the AlF_4^--bound state in complex with SPM (E2Pi(SPM)). These structures, together with Molecular dynamics simulation and biochemical analyses, have revealed the unique mechanisms of polyamine recognition and transport by ATP13A2.

3.2 Materials and methods

3.2.1 Cloning

The human ATP13A2 transcription variant 2 (Uniprot: Q9NQ11-2) cDNA was purchased from Kazusa DNA Research Institute. The human ATP13A2 cDNA was first cloned into the pEG BacMam vector, with an N-terminal His_8 tag and EGFP followed by a tabaco etch virus protease (TEV protease) recognition site. In the optimization process of purification system, tabaco etch virus protease (TEV protease) recognition site was replaced by a human rhinovirus 3C protease (HRV3C protease) recognition site by QuikChange (Figure 3-1).

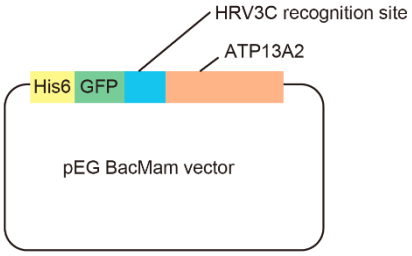

Figure 3-1 | Expression and Purification Construct of ATP13A2

Expression and purification construct of human ATP13A2.

3.2.2 Fluorescence-detection size-exclusion chromatography analysis

The GFP-based screening and optimization were performed based on published protocols. The plasmids outlined in Section 3.2.1 were transformed into HEK293T cells (American Type Culture Collection, catalog no. CRL-3216) using Lipofectamine® 3000 Reagent (Thermo Fisher Scientific) following manufacturer's protocol. Transformed cells were grown in a Dulbecco's Modified Eagle's Medium (Sigma, catalog no. D5786) containing 10% fetal bovine serum (Sigma), at 37°C in the presence of 8% CO_2 for 48h. The cells were collected by centrifugation (5,000 × g, 10 min, 4°C) and lysed in buffer, containing 50 mM Tris (pH 8.0), 150 mM NaCl, 5 mM DTT, and 20% (v/v) glycerol.

Expression levels and solution behaviors of human ATP13A2 were evaluated by the following procedure. Collected cells were solubilized in a 300 μL buffer containing 50 mM Tris (pH 8.0), 150 mM NaCl, 5 mM DTT, and 1–2% (w/v) of specified detergents. After solubilization for 60 min at 4ºC, insoluble materials were removed by ultracentrifugation. 70 μL of supernatants were subjected to a fluorescence-detection size-exclusion chromatography on a ENrich™ SEC 650 10 x 300 Column (Bio-Rad Laboratories), equilibrated with a buffer containing 10 mM Tris-HCl, pH 8.0, 150 mM NaCl, and 0.03% DDM. The elution profile was monitored by a fluorescence detector RF-20Axs (Shimadzu) with the excitation wavelength at 480 nm and emission wavelength at 512 nm.

3.2.3 Overexpression and Protein purification

For large-scale protein purification, human ATP13A2 was overexpressed in BacMam system. The recombinant baculovirus of human ATP13A2 was prepared using the Bac-to-Bac baculovirus expression system (Invitrogen). HEK293S GNTI$^-$ (N-acetylglucosaminyl-transferase I–negative) cells (American Type Culture Collection, catalog no. CRL-3022) were infected at a density of 3.0 × 10^6 cells ml^{-1} with one-hundredth volume of a solution containing the virus encoding the above construct. The infected HEK293S cells were incubated in FreeStyle 293 Expression medium (Gibco) with 2% fetal bovine serum (Sigma), at 37°C in the presence of 8% CO_2. After 8-12 h, 10 mM valproic acid (Sigma) was added, and the cells were further incubated at 30°C in the presence of 8% CO_2 for 48 h. The cells were collected by centrifugation (5,000 × g, 10 min, 4°C) and lysed in buffer, containing 50 mM Tris (pH 8.0), 150 mM NaCl, 5 mM DTT, and 20% (v/v) glycerol. The collected cells were solubilized for 1 h at 4°C in buffer, containing 50 mM Tris (pH 8.0), 150 mM NaCl, 1.5% (w/v) N-dodecyl β-D-maltoside (DDM), 0.15% (w/v) cholesterol hemisuccinate CHS, 5 mM DTT, and 20% (v/v) glycerol.

After ultracentrifugation, the supernatant was incubated with AffiGel 10 (Bio-Rad) coupled with a GFP-binding nanobody for 1 h at 4°C. The resin was washed five times with four column volumes of wash buffer, containing 50 mM Tris (pH 8.0), 300 mM NaCl, 1.5% (w/v) glyco-

diosgenin (GDN), 5 mM DTT, and 20% (v/v) glycerol, and then gently suspended overnight with HRC3C Protease to cleave the His_8-EGFP tag. After HRV3C protease digestion, the flowthrough was collected, mixed with Ni-NTA Superflow resin (QIAGEN) and incubated for 1 min at 4°C to remove the HRV3C protease. The collected flowthrough was then concentrated using an Amicon Ultra filter (molecular mass cut-off 100 kDa, Millipore), and further purified by chromatography on a gel filtration column (Superose 6 Increase 10/300 GL, GE Healthcare) equilibrated with gel filtration buffer, containing 20 mM Tris (pH 8.0), 150 mM NaCl, 0.06% (w/v) glyco-diosgenin (GDN), and 5 mM DTT. The peak fractions of the protein were pooled and concentrated to ~10 mg ml^{-1} with a centrifugal device (Millipore 30 kDa MW cutoff).

3.2.4 Electron microscopy preparation

The purified ATP13A2 was mixed with inhibitor at the following final concentrations (Figure 3-2): E1-ATP, 5 mM $MgCl_2$ and 2 mM AMPPCP; E1P-ADP, 5 mM $MgCl_2$, 5 mM NaF, 1 mM $AlCl_3$, and 5 mM ADP; E2P(SPM), 5 mM spermine, 5 mM $MgCl_2$, 10 mM NaF, and 2 mM $BeSO_4$; E2Pi(SPM), 5 mM spermine, 5 mM $MgCl_2$, 10 mM NaF, and 2 mM $AlCl_3$. After an incubation for 1 h on ice, the protein solutions were applied to a freshly glow-discharged Quantifoil holey carbon grid (R1.2/1.3, Cu/Rh, 300 mesh), using a Vitrobot Mark IV (FEI) at 4°C with a blotting time of 4s under 99% humidity conditions, and then the grids were plunge-frozen in liquid ethane.

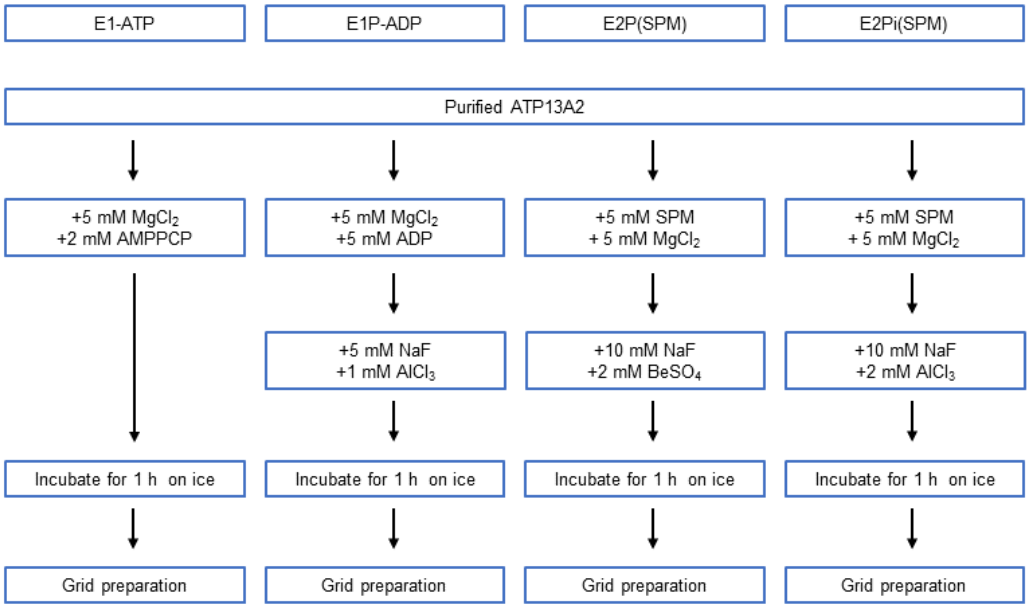

Figure 3-2 | Flowchart of electron microscopy preparation of ATP13A2

Flowchart of electron microscopy preparation of ATP13A2 in E1-ATP, E1P-ADP state, E2P(SPM), and E2Pi(SPM) states are shown. Concentrations in the figure are shown as final concentrations.

3.2.5 Electron microscopy data collection

The grids with the E1-ATP and E1P-ADP samples were transferred to a Titan Krios G3i microscope (Thermo Fisher Scientific), running at 300 kV and equipped with a Gatan Quantum-LS Energy Filter (GIF) and a Gatan K3 Summit direct electron detector, operated in the electron counting mode. Imaging was performed at a nominal magnification of 105,000×, corresponding to a calibrated pixel size of 0.83 Å/pix (The University of Tokyo, Japan). Each movie was recorded for 2.55 seconds and subdivided into 48 frames. The electron flux was set to 14 e^-/s at the detector, resulting in an accumulated exposure of 50 e^-/Å^2 at the specimen. The data were automatically acquired by the image shift method using the SerialEM software[134], with a defocus range of -0.8 to -1.6 μm. More than 3,500 movies were acquired for each grid condition, and the numbers of total images are described in Table 3-1.

The grids of the E2P(SPM) and E2Pi(SPM) samples were transferred to a Titan Krios G3i microscope (Thermo Fisher Scientific), running at 300 kV and equipped with a Gatan Quantum-LS Energy Filter (GIF) and a Gatan K3 Summit direct electron detector, operated in the electron counting CDS mode. Imaging was performed at a nominal magnification of 105,000×, corresponding to a calibrated pixel size of 0.83 Å/pix (The University of Tokyo, Japan). Each movie was recorded for 5.96 seconds and subdivided into 64 frames. The electron flux was set to 7.55 e^-/s at the detector, resulting in an accumulated exposure of 60 e^-/Å^2 at the specimen. The data were automatically acquired by the image shift method using the SerialEM software[134], with a defocus range of -0.8 to -1.6 μm. More than 3,000 movies were acquired for each grid condition, and the numbers of total images are described in Table 3-1.

3.2.6 Image processing

For all datasets, the dose-fractionated movies were subjected to the beam-induced motion correction implemented in RELION-3.1[135], and the contrast transfer function (CTF) parameters were estimated using CTFFIND4[136].

For the E1-ATP state in the presence of AMPPCP, 1,989,286 particles were initially picked from the 3,114 micrographs by using the Laplacian-of-Gaussian picking function in RELION-3.1[135], and extracted with down-sampling to a pixel size of 3.32 Å/pix. These particles were subjected to several rounds of 2D and 3D classifications. The best class contained 345,121 particles, which were then re-extracted with a pixel size of 1.51 Å/pix and subjected to 3D refinement. The resulting 3D model and particle set were subjected to per-particle defocus refinement, beam-tilt refinement, Bayesian polishing[137], micelle subtraction and 3D refinement. The final 3D refinement and postprocessing of the three classes yielded a map with a global resolution of 3.6 Å, according to the FSC = 0.143 criterion[138]. The local resolution was estimated by RELION-3.1.

The processing strategy is described in Figure 3-6A-C. For the E1P-ADP state dataset in the presence of AlF_4^- and ADP, 1,950,094 particles were initially picked from the 3,303 micrographs, and extracted with down-sampling to a pixel size of 3.32 Å/pix, as described above. These particles were subjected to three rounds of 3D classifications. The best class from the 3D classification contained 121,731 particles, which were then re-extracted with a pixel size of 1.51 Å/pix and subjected to 3D refinement, using a soft mask covering the proteins and micelles. The resulting 3D model and particle set were subjected to per-particle CTF refinement, beam-tilt refinement, and Bayesian polishing before the final 3D refinement and postprocessing, yielding a map with a global resolution of 3.5 Å according to the Fourier shell correlation (FSC) = 0.143 criterion. Finally, the local resolution was estimated using RELION-3. The processing strategy is described in Figure 3-7A-C. For the E2P(SPM) state in the presence of BeF_3^-, 1,762,758 particles were initially picked from the 3,289 micrographs, and extracted with a pixel size of 3.37 Å/pix, as described above. These particles were subjected to several rounds of 3D classifications. The best class from the 3D classification contained 22,952 particles, which were then re-extracted with a pixel size of 1.34 Å/pix and subjected to 3D refinement. The resulting 3D model and particle set were subjected to Bayesian polishing and 3D refinement. The final 3D refinement and postprocessing of the best particles yielded a map with a global resolution of 3.9 Å, according to the FSC = 0.143 criterion. The local resolution was estimated using RELION-3. The processing strategy is described in Figure 3-8A-C. For the E2Pi(SPM) state in the presence of AlF_4^-, 1,958,257 particles were initially picked from the 3,834 micrographs, and extracted with a pixel size of 3.37 Å/pix, as described above. These particles were subjected to several rounds of 3D classification. The best class from the 3D classification contained 53,403 particles, which were then re-extracted with a pixel size of 1.34Å/pix and subjected to 3D refinement. The resulting 3D model and particle set were subjected to Bayesian polishing and 3D refinement. The final 3D refinement and postprocessing of the best particles yielded a map with a global resolution of 3.8 Å, according to the FSC = 0.143 criterion. The local resolution was estimated, and the processing strategy is described in Figure 3-9A-C.

3.2.7 Model building and refinement

The quality of the density maps of the E1-ATP and E2P(SPM) states was sufficient to build a model manually in COOT[139]. These models were used as the template for the modeling of other states. The model building was facilitated by the crystal structure of the sodium-potassium pump (PDB ID: 2ZXE)[140] and previous crystal structures of SERCA (PDB IDs: 3B9B, 3B9R)[69] and cryo-EM structures of P5A ATPase Spf1 (PDB IDs: 6XMQ, 6XMT)[91]. The model building was also facilitated by maps postprocessed by deepEMhancer[141], a deep learning-based post-processing tool. For the NTD, the model predicted by RaptorX[142] was fitted into the map and

manually adjusted with COOT. After manual adjustment of the models, structure refinement was performed with phenix.real_space_refine ver. 1.18[143]. The refined models were further processed using Refmac5[144] and servalcat[145] with ProSMART[146] distance restraints generated from the cryo-EM structures of P5A ATPase Spf1 (PDB IDs: 6XMQ, 6XMT)[91] as the templates. The sequence alignment was generated using HHpred[147] server and the models were prepared using phenix.mr_model_preparation. The statistics of the 3D reconstruction and model refinement are summarized in Table 3-1. All molecular graphics figures were prepared with CueMol (http://www.cuemol.org) and UCSF ChimeraX[148].

3.2.8 ATPase activity assay

The ATPase activity assay was performed mainly performed by Dr. Daiho, in collaboration with Dr. Daiho from the Asahikawa Medical University. The rate of ATP hydrolysis was determined at 37 °C for 30 min in 10 μL of a mixture containing 0.8 μg of microsomal protein, 1 mM [γ-^{32}P]ATP, 0.125 mM PIP_2, 0.125 mM PA, various concentrations of SPM, 200 mM KCl, 5 mM DTT, 0.03% GDN, and 20 mM MOPS/KOH (pH 7.0). The reaction was chased by the addition of HCl, and the released $^{32}P_i$ was quantified as described previously[149]. The SPM dependence (Fig. 3-5) was calculated by the least fitting of ATPase activities to the complex Hill equation.

$$v = V_{max}\left(\frac{1}{1+\left(\frac{K_1}{[SPM]}\right)^{n_1}}\right)\left(1-\frac{1}{1+\left(\frac{K_2}{[SPM]}\right)^{n_2}}\right)$$

To measure the amount of EP formation at steady state without substrate, phosphorylation of ATP13A2 in microsomes with [γ-^{32}P]ATP was performed under conditions described in the figure legends essentially as described previously[149]. The amount of EP was determined by acid quenching. Precipitated proteins were separated by 5% SDS-PAGE at pH 6.0. The radioactivity associated with the separated ATP13A2 was quantified by digital autoradiography. The amount of EP for expressed ATP13A2 was obtained by subtracting the background radioactivity determined with the microsomes from the mock-transfected cells. The background radioactivity was less than 9% of the total radioactivity of the microsomes expressing wild-type ATP13A2.

3.2.9 Molecular dynamics simulation

The system included the ATP13A2, SPM, 1-phosphoryl-2-oleoylphosphatidylcholine (POPC), TIP3P water and 150 mM NaCl. The initial model of ATP13A2 containing amino acids 191-1173 was created with MODELLER[150], using the cryo-EM structure of ATP13A2 in E1-ATP state (for E1(apo) condition), E2P(SPM) state (for E2P and E2P(SPM) condition) or E2Pi(SPM) state (for E2Pi(SPM) condition) as the template. Since the NTD is a regulatory domain and ATP13A2

lacking the NTD has the same SPM-dependent ATPase activity as the wild type, the NTD was excluded in the initial model for MD simulation[151]. The missing hydrogen atoms were built with the program VMD[152]. The protein was embedded into the POPC membrane, using the MemProtMD pipeline[153]. The net charge of the simulation system was neutralized through the addition of 150 mM NaCl. The simulation system was 120 × 120 × 144 $Å^3$ and contained 195,442 atoms for E1(apo) condition, 195,136 atoms for E2P condition, 195,166 atoms for E2P(SPM) condition, 195,180 atoms for E2Pi(SPM) condition. The molecular topologies and parameters from the Charmm36 force field[154,155] were used for the protein, lipid, and water molecules. The molecular topology and parameters for SPM were prepared using the CHARMM-GUI ligand reader and modeler[156,157].

Molecular dynamics simulations were performed with the program NAMD 2.13. The simulation systems were energy minimized for 1,000 steps with fixed positions of the non-hydrogen atoms. After minimization, another 1,000 steps of energy minimization were performed with 10 kcal mol^{-1} restraints for the non-hydrogen atoms, except for the lipid molecules within 5.0 Å of the proteins. Next, equilibrations were performed for 0.1 ns under NVT conditions, with 10 kcal $mol^{-1}Å^{-2}$ restraints for the heavy atoms of the proteins. Finally, equilibration was performed for 2.0 ns under NPT conditions, with the 1.0 kcal $mol^{-1}Å^{-2}$ restraints for all Cα atoms of the proteins. The production runs were performed for 200 ns without restraints, while maintaining constant temperature at 310K using Langevin dynamics and constant pressure at 1 atm using a Nosé-Hoover Langevin piston[158]. The long-range electrostatic interactions were calculated by the particle mesh Ewald method[159]. The simulations were performed twice each for the E1 apo state, E2P state in the absence of SPM, E2P state in the presence of SPM, and E2Pi state in the presence of SPM. The simulation results were analyzed and visualized with mdtraj[160], seaborn[161] and CueMol (http://www.cuemol.org).

3.3 Results

3.3.1 Expression and purification of the ATP13A2

Since the functional role of ATP13A2 has only been identified in humans, I limited my study to human ATP13A2. To confirm the expression of ATP13A2 and to examine the detergent conditions suitable for purification, I conducted fluorescence-detection size-exclusion chromatography (FSEC) analysis. Our construct contained ATP13A2, N-terminal His_8 tag and enhanced green fluorescent protein (EGFP) for purification. As a result of FSEC analysis, I confirmed ATP13A2 expressed in HEK293T cells, monodisperse profile was observed when solubilized with DDM-CHS and GDN, while broad and polydisperse profile was observed when solubilized with LMNG-CHS (Figure 3-3).

After optimization, I succeeded in obtaining purified ATP13A2 by following procedure described in 3.2.3 (Figure 3-4). Moreover, I confirmed our expression and purification construct of ATP13A2 maintain SPM dependent ATPase activity, in collaboration with Dr. Daiho from the Asahikawa Medical University, as detailed in the next section (Figure 3-5).

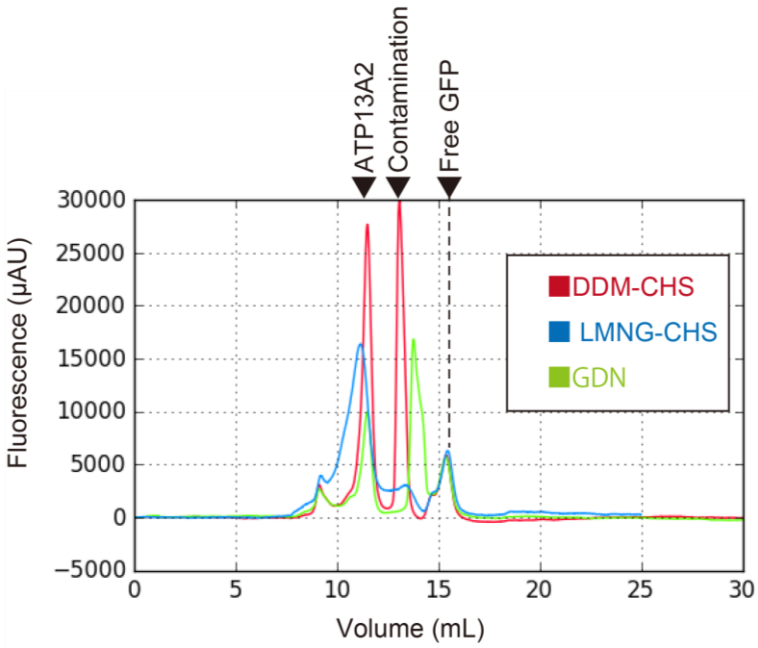

Figure 3-3 | FSEC profiles of ATP13A2

Superposition of fluorescence traces of ATP13A2 solubilized with DDM-CHS(red), LMNG-CHS(blue), GDN (green) in size exclusion chromatography. ENrich™ SEC 650 10 x 300 Column (Bio-Rad Laboratories) was used for chromatography.

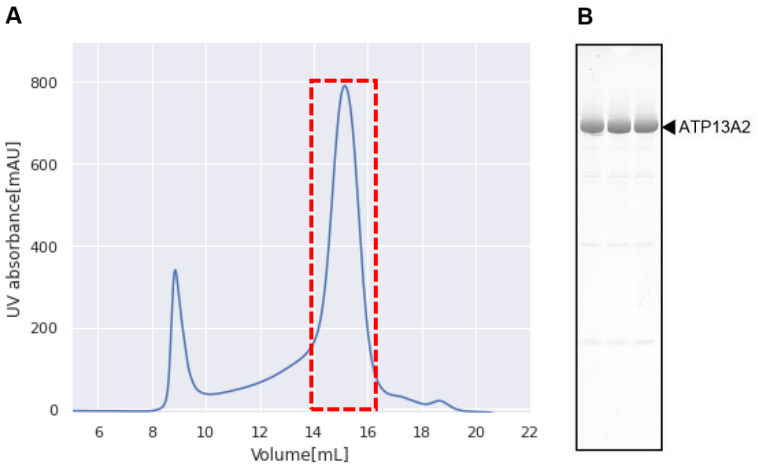

Figure 3-4 | Purified ATP13A2

(**A**) Final gel filtration profile of the ATP13A2. Superose 6 Increase 10/300 GL (GE Healthcare) was used for gel filtration.

(**B**) SDS-PAGE gel of peak fraction indicated by red square in (**A**).

3.3.2 Confirmation of SPM-dependent ATPase activity

To confirm that our constructs maintain SPM-dependent ATPase activity, I performed ATPase assay using ATP13A2-expressing microsomes, in collaboration with Dr. Daiho from the Asahikawa Medical University. The N-terminally GFP-tagged, full-length human ATP13A2 was expressed in human embryonic kidney–293 (HEK293) cells. Microsomes prepared from the cells showed SPM-dependent ATPase activity (Figure 3-5).

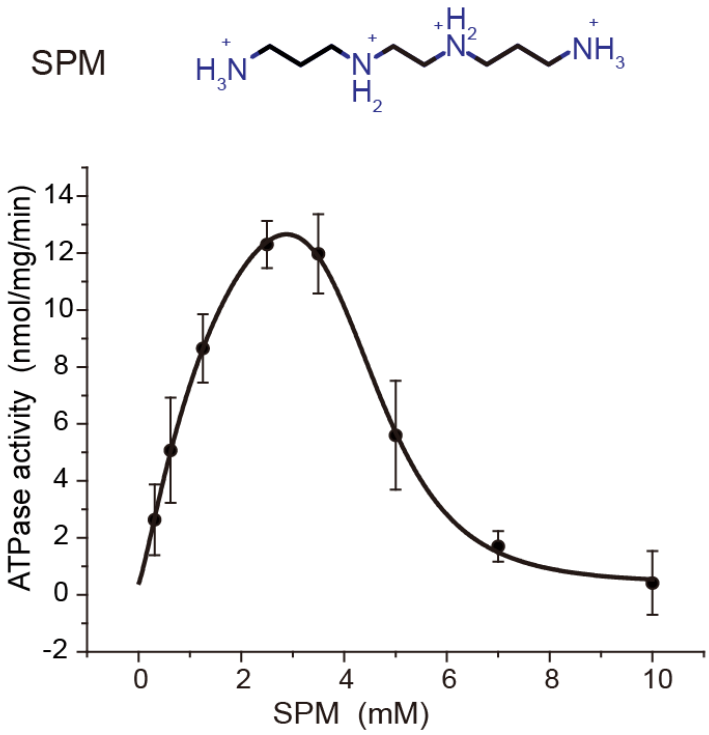

Figure 3-5 | Functional analysis of ATP13A2

Chemical structural formula of spermine (SPM) (upper panel) and dose-response curves (lower panel) showing the SPM-dependent ATPase activities of ATP13A2-expressing microsomes. Phosphatidic acid and phosphatidylinositol 3,5-bisphosphate (PtdIns(3,5)P_2, PIP_2) were added to facilitate the ATPase activity of ATP13A2. Data points represent the mean ± SEM of three to six measurements. SPM-dependent ATPase activity of ATP13A2 was measured by subtracting the ATPase activity in the absence of SPM. The solid line for the SPM dependence shows the least fit of ATPase activities (v) to the complex Hill equation (Methods). The obtained K_1, K_2 and Hill coefficients n_1, n_2 were 1.7 ± 0.5, 4.5 ± 0.1 mM and 1.2 ± 0.2, 5.9 ± 0.5, respectively. V_{max} is 20.0 ± 3.7 nmol mg^{-1} min^{-1}.

3.3.3 Electron microscopy preparation and data collection

To understand the molecular mechanisms of SPM transport by P5B ATPase, I performed a cryo-EM analysis of the human P5B ATPase polyamine exporter, ATP13A2 (Figures 3-6–3-9). The N-terminally GFP-tagged, full-length human ATP13A2 was expressed in human embryonic kidney–293 (HEK293) cells. The ATP13A2 protein was purified in glyco-diosgenin (GDN) and subjected to cryo-EM single-particle analyses under several different conditions, in the presence of AMPPCP, AlF_4^--ADP, BeF_3^-, and AlF_4^- (Figures 3-6–3-9, Table 3-1).

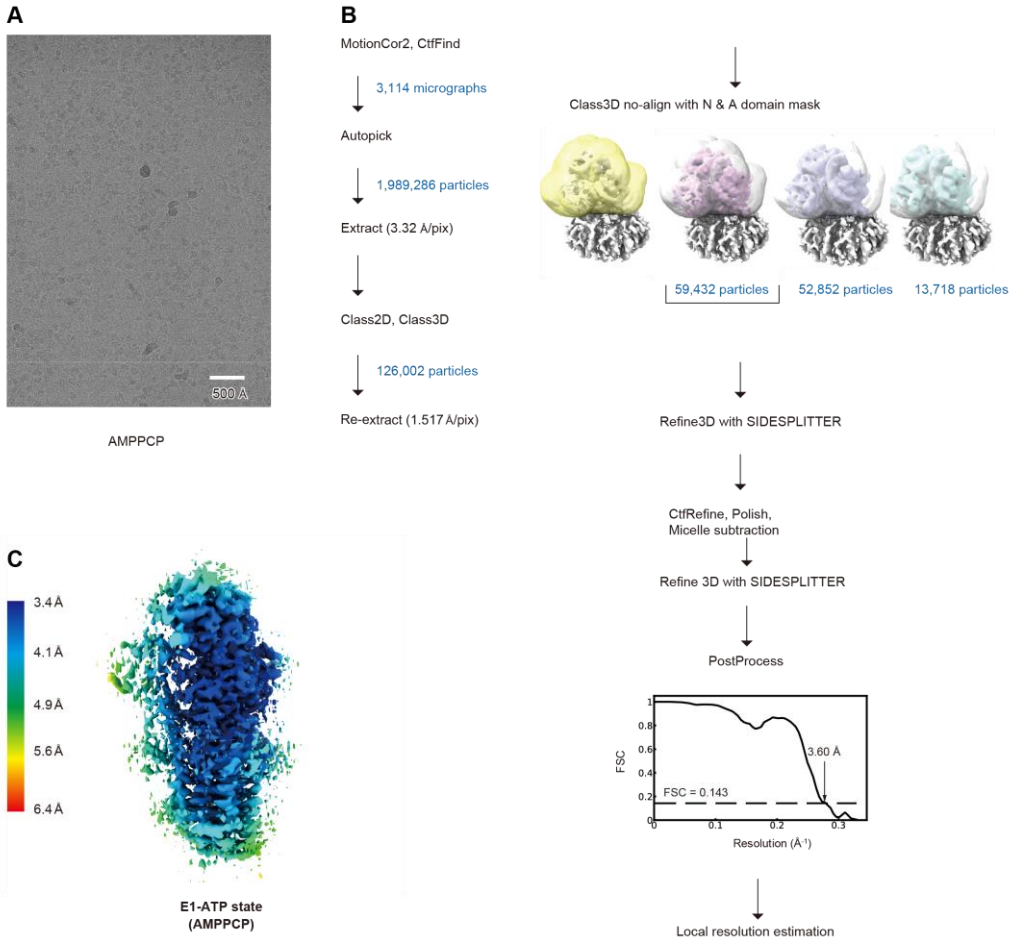

Figure 3-6 | Data processing of ATP13A2 in complex with AMPPCP.

(**A-C**) Data processing of ATP13A2 in complex with AMPPCP. (**A**) Representative cryo-EM image of ATP13A2 in the presence of AMPPCP. (**B-C**) Data processing workflow of image processing (**B**), and local resolution analysis (**C**) of ATP13A2 in the presence of AMPPCP.

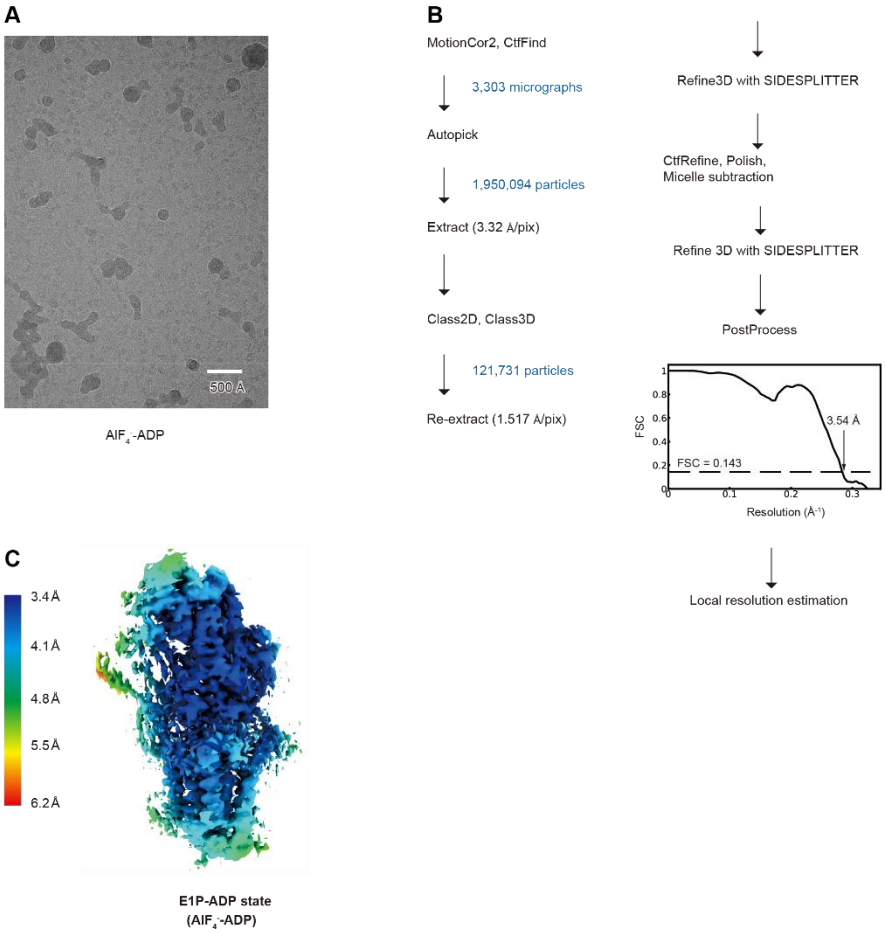

Figure 3-7 | Data processing of ATP13A2 in complex with AlF_4^--ADP.

(**A-C**) Data processing of ATP13A2 in complex with AlF_4^--ADP. (**A**) Representative cryo-EM image of ATP13A2 in the presence of AlF_4^--ADP. (**B-C**) Data processing workflow of image processing (**B**) and local resolution analysis (**C**) of ATP13A2 in the presence of AlF_4^-ADP.

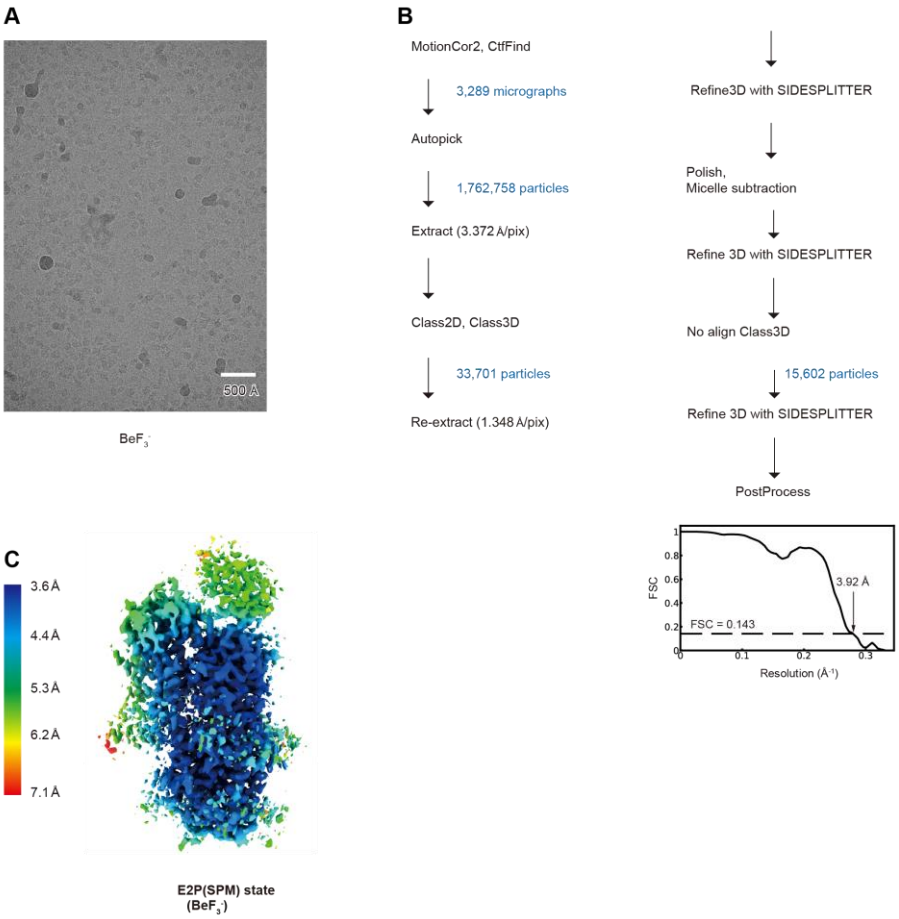

Figure 3-8 | Data processing of ATP13A2 in complex with BeF_3^-

(**A-C**) Data processing of ATP13A2 in complex with BeF_3^-. (**A**) Representative cryo-EM image of ATP13A2 in the presence of BeF_3^-. (**B-C**) Data processing workflow of image processing (**B**) and local resolution analysis (**C**) of ATP13A2 in the presence of BeF_3^-.

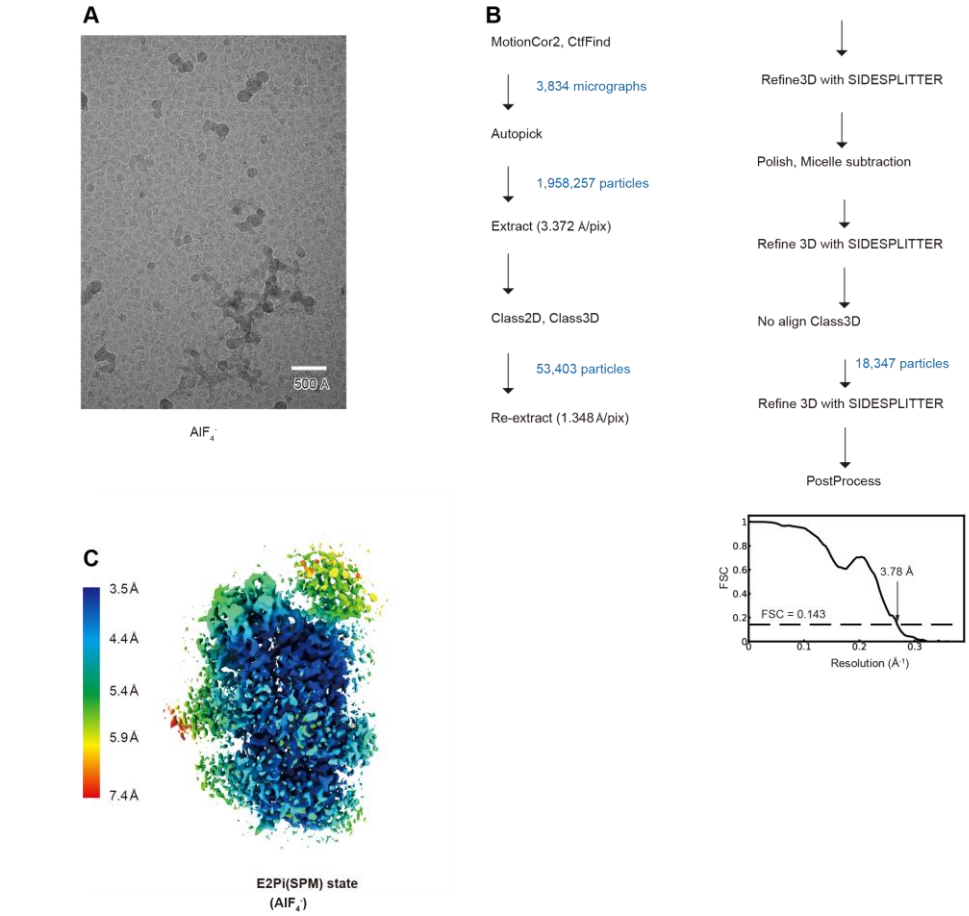

Figure 3-9 | Data processing of ATP13A2 in complex with AlF_4^-.

(**A-C**) Data processing of ATP13A2 in complex with AlF_4^-. (**A**), Representative cryo-EM image of ATP13A2 in the presence of AlF_4^-. (**B-C**) Data processing workflow of image processing (**B**) and local resolution analysis (**C**) of ATP13A2 in the presence of AlF_4^-.

3.3.4 Image processing and structural determination

The acquired movies were motion-corrected and processed in RELION 3.1[135], which eventually provided cryo-EM maps at overall resolutions of 3.54 to 3.92 Å, according to the gold-standard Fourier shell correlation 0.143 criterion (Figures 3-6–3-9). The cytoplasmic ATPase domains are well-resolved in the AMPPCP- and BeF_3^--bound states, thus allowing *de novo* modeling of the almost entire ATP13A2 structure, except for some minor disordered regions (residues 1–33, 114–160, 587–595, 611–617, 798–819, 1174–1180 in the BeF_3^--bound state, residues 1–179, 590–595, 611–617, 798–819, 1174–1180 in the AMPPCP-bound state), and these models were used as the template for the modeling of other states (Figures 3-10, 3-11).

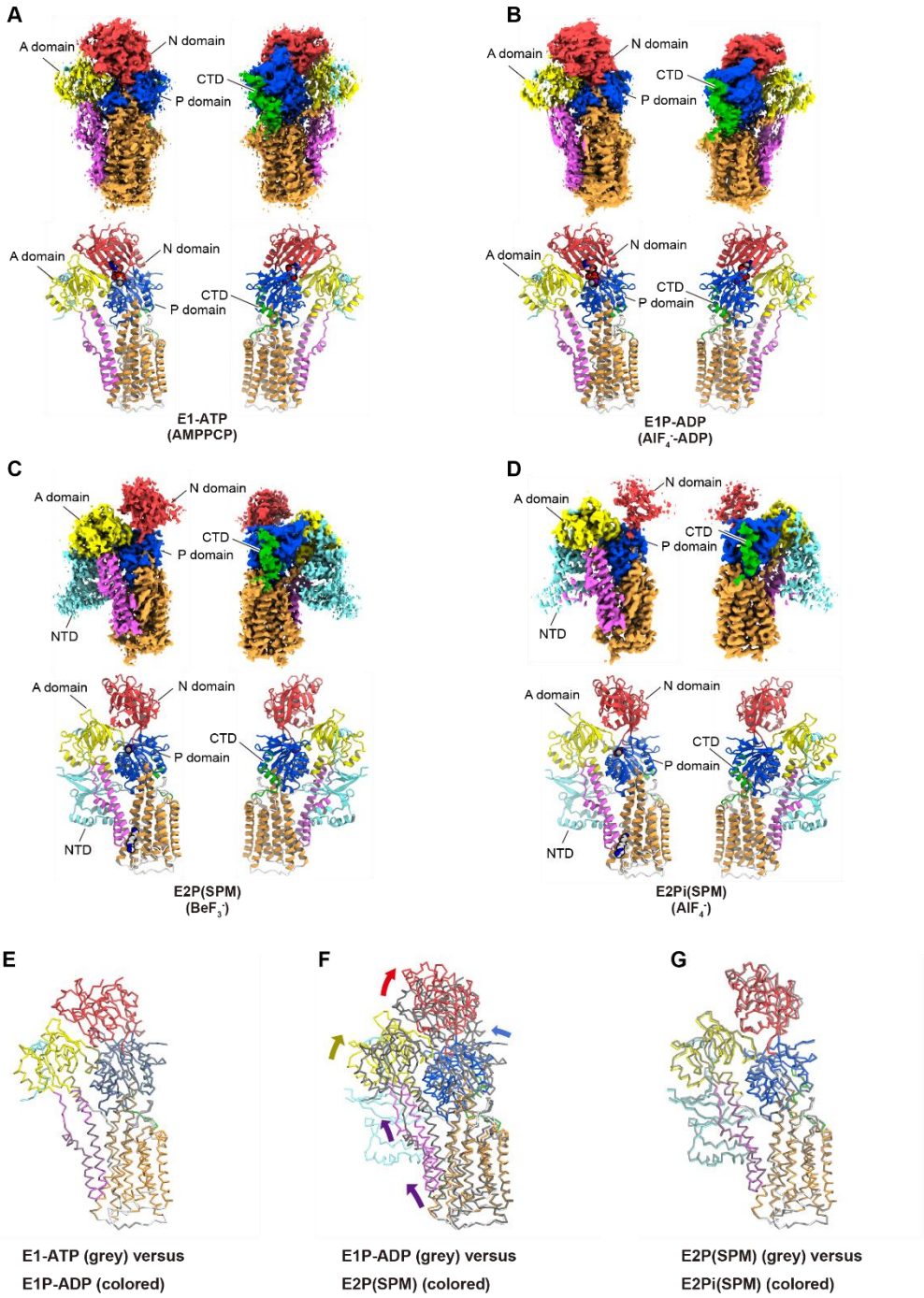

Figure 3-10 | Cryo-EM maps and structures of ATP13A2 in complex with AMPPCP, AlF_4^--ADP, BeF_3^- and AlF_4^-.

(**A-D**) Cryo-EM maps (upper) and atomic models (lower) of ATP13A2 in complex with AMPPCP (**A**), AlF_4^--ADP (**B**), BeF_3^- (**C**), and AlF_4^- (**D**), viewed from the two opposite sides. Colors are according to Figure 3-12A. (**E-G**) Structural comparison of ATP13A2 between E1-ATP and E1P-ADP states (**E**), E1P-ADP and E2P(SPM) states (**F**), E2P(SPM) and E2Pi(SPM) states (**G**). Structures are shown in the backbone-trace representation.

Table 3-1 | Cryo-EM data collection and refinement statistics

	E1ATP	E1P-ADP	E2P(SPM)	E2Pi(SPM)
Data collection and processing				
EMDB-ID	EMD-32066	EMD-32067	EMD-32068	EMD-32069
PDB ID	7VPI	7VPJ	7VPK	7VPL
Inhibitor	AMPPCP	AlF_4^--ADP	BeF_3^-	AlF_4^-
Microscope	Titan Krios G3i			
Detector	Gatan K3 Camera with Quantum LS energy filter			
Data acquisition mode	Counting mode		CDS counting mode	
Magnification	105,000			
Voltage (kV)	300			
Electron exposure ($e^-/Å^2$)	50	50	60	60
Defocus range (μm)	-0.8 to -1.6			
Pixel size (Å)	0.83			
Symmetry imposed	C1			
Number of movies	3,114	3,303	3,289	3,834
Initial particle images	1,989,286	1,950,094	1,762,758	1,958,257
Final particle images	59,432	121,731	15,602	18,347
Map resolution (Å)	3.60	3.54	3.92	3.78
FSC threshold	0.143			
Map sharpening B factor ($Å^2$)	-128.0	-148.0	-90.6	-93.2
Model building and refinement				
Model composition				
Protein atoms	7,343	7,343	8,150	8,150
Metals	1	2	2	2
Other atoms	31	44	45	46
R.m.s deviations				
Bond lengths (Å)	0.0172	0.0174	0.0175	0.0173
Bond angles (°)	2.37	2.38	2.29	2.29
Validation				
Clashscore	3.60	3.59	2.58	2.40
Rotamer outliers (%)	29.79	28.69	19.91	14.93
Ramachandran plot				
Favoured (%)	95.58	95.48	95.98	96.94
Allowed (%)	4.00	4.10	3.92	2.97
Outliers (%)	0.42	0.42	0.10	0.10

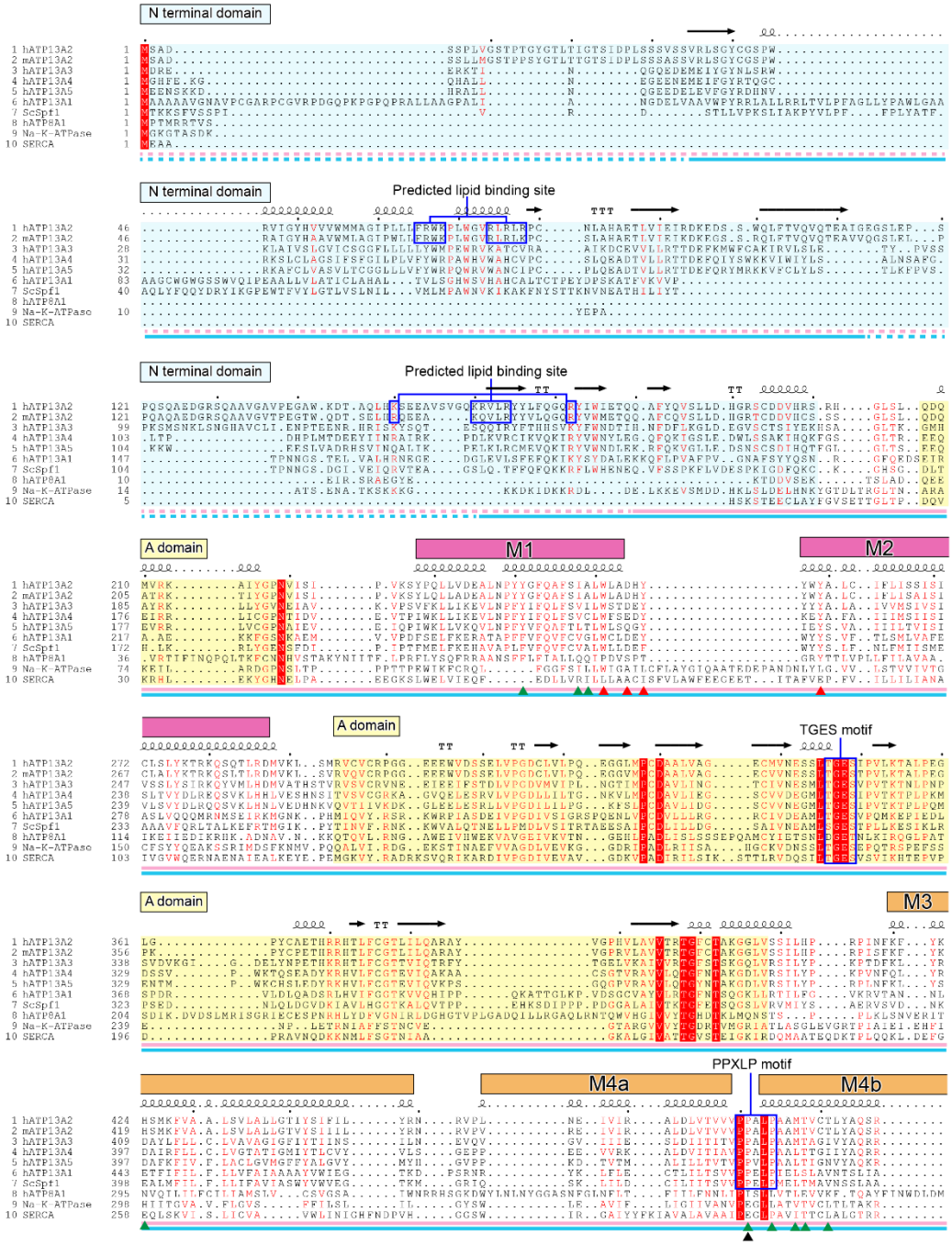

Figure 3-11 | Sequence alignment of human and mouse ATP13A2, P5 ATPases and P4 ATPases with known structures, and canonical P2 ATPases (see next page for caption)

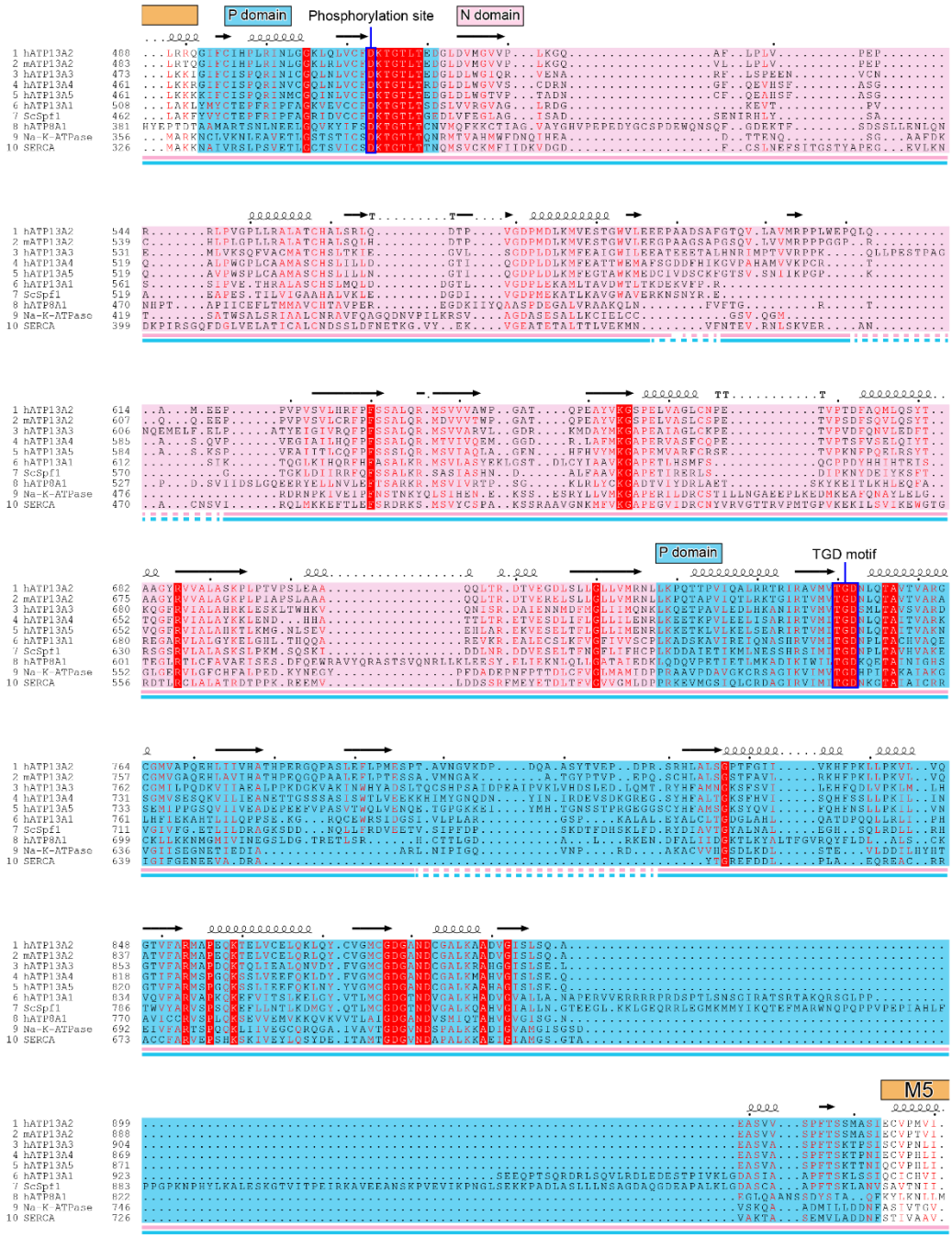

Figure 3-11 | Sequence alignment of human and mouse ATP13A2, P5 ATPases and P4 ATPases with known structures, and canonical P2 ATPases (continued, see next page for caption)

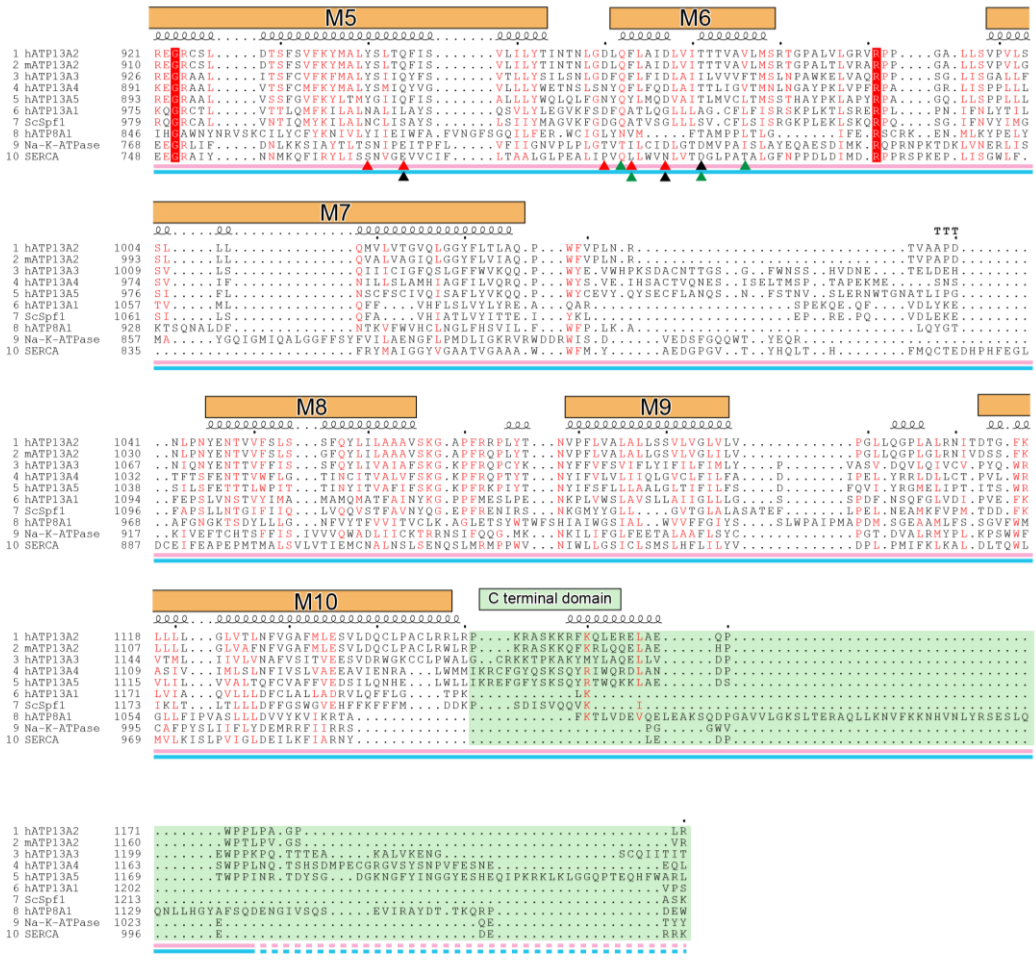

Figure 3-11 | Sequence alignment of human and mouse ATP13A2, P5 ATPases and P4 ATPases with known structures, and canonical P2 ATPases

Sequence alignment of human ATP13A2 (UniProt: Q9NQ11) and mouse ATP13A2 (UniProt: Q9CTG6); other P5B ATPases: human ATP13A3 (UniProt: Q9H7F0), human ATP13A4 (UniProt: Q4VNC1) and human ATP13A5 (UniProt: Q4VNC0); P5A ATPases: human ATP13A1 (UniProt: Q9HD20) and Saccharomyces cerevisiae SPF1 (UniProt: P39986); P4 ATPase with known structure: human ATP8A1; canonical P2 ATPases: shark Na^+/K^+-ATPase (UniProt: Q4H132) and sarcoplasmic reticulum Ca^{2+}-ATPase (SERCA) isoform 1a (UniProt: P04191). The sequence alignment was generated using MSAProbs[162] and ESPript 3.0[163]. The secondary structure, conserved domains and transmembrane helices of hATP13A2 are indicated above the sequences. Blue boxes: the predicted PIP binding site[62], the conserved TGES motif, PPXLP motif, phosphorylation site, and TGD motif. Red arrowheads: amino acids involved in SPM recognition in hATP13A2. Black arrowheads: amino acids involved in the Ca^{2+} and H^+ binding in SERCA. Green arrowheads: amino acids involved in the phospholipid recognition in ATP8A1. The modeled regions (E1-ATP state: pink line, E2P(SPM) state: blue line) and disordered region (E1-ATP state: dashed pink line, E2P(SPM) state: dashed blue line) are indicated below the sequence.

3.3.4 Overall structure

The overall structure shows the typical P-type ATPase fold, composed of three large cytoplasmic domains (A, actuator; N, nucleotide binding; P, phosphorylation) and ten membrane-spanning helices (M1 to M10) (Figure 3-12A-C). ATP13A2 has extra C-terminal and N-terminal domains (CTD and NTD, respectively), which are not present in P1–P4 ATPases[70,73–91]. The CTD adopts a short α-helix that lines and stabilizes the P domain, whereas the NTD is extended from the A domain and anchored to the lipid membrane (Figure 3-12B, C). According to the hydropathy plot, the NTD contains a pair of short membrane-embedded helices[62] but density of this region is week and almost disordered in the AMPPCP- and AlF_4^--ADP-bound states. A similar NTD structure was also observed in a yeast P5A-ATPase[91], and the NTD structure is likely to be a common feature in the P5 ATPases, based on the amino acid sequence alignment (Figure 3-11).

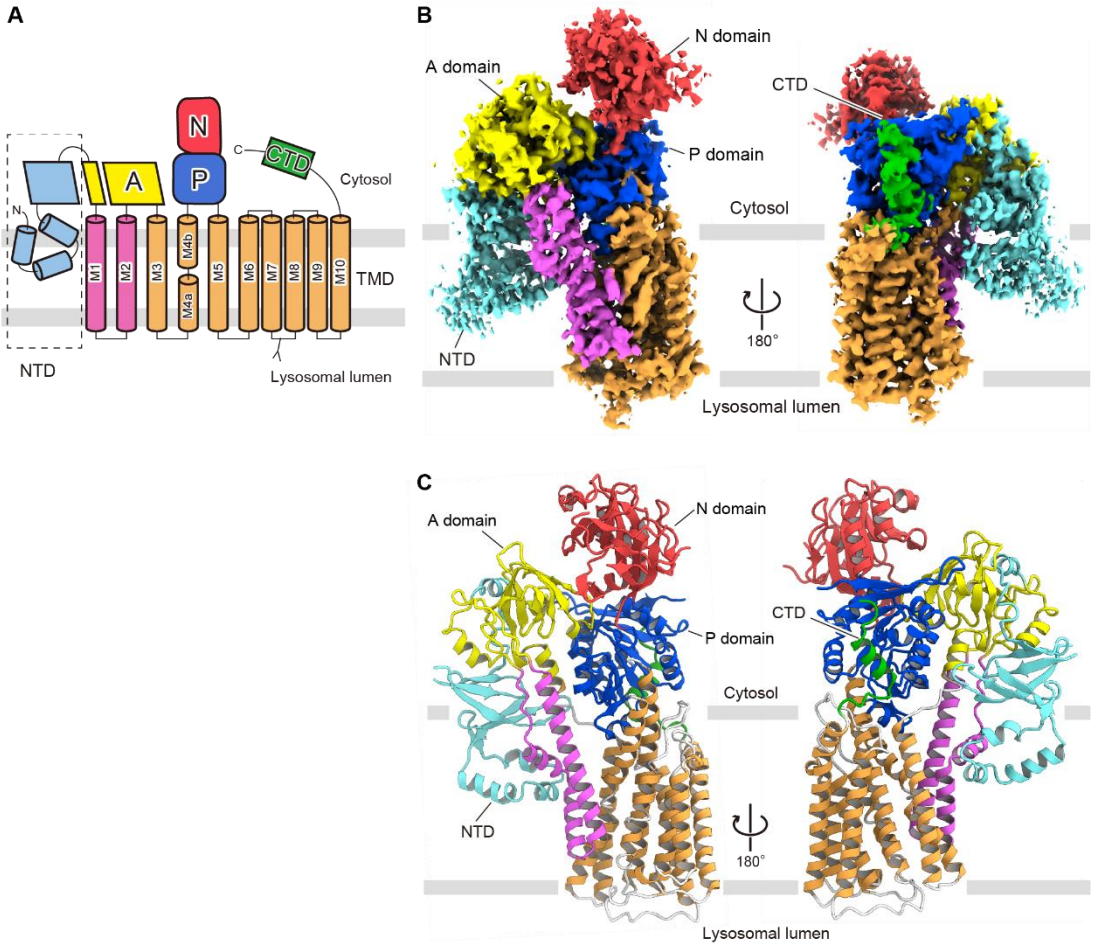

Figure 3-12 | Overall structure of ATP13A2

(**A**) Topology diagram of human ATP13A2. Conserved domains and TM helices are schematically illustrated. In the cytoplasmic regions, the A, N, and P domains, N-terminal domain (NTD), and the C-terminal regulatory domain (CTD) are colored yellow, red, blue, cyan, and green, respectively. M1-M2 and M3-10 are pink and orange, respectively. The N-glycosylation site is shown as sticks. (**B,C**) Overall structure of ATP13A2. Cryo-EM maps (**B**) and ribbon models (**C**), shown with the same color scheme as in (**A**).

3.3.5 Ligand binding cavity and transport pathway

ATP13A2 generally follows the Post-Albers scheme[64,65] (Figure 3-13A). In this model, ATP-dependent autophosphorylation and polyamine-dependent dephosphorylation alternately induces the transition of the different enzymatic states, referred as E1 and E2, and consequently allows polyamine transport. The cryo-EM maps revealed the densities of the respective inhibitors at the catalytic site, which stabilize the ATPase domains in respective conformations (Figure 3-13A,B). The AMPPCP- and AlF_4^--ADP-bound structures, which correspond to the E1-ATP and E1P-ADP states, respectively, represent the ATP-dependent autophosphorylation step in the Post-Albers scheme (Figures 3-10A, B, 3-13A). The ATP analog is recognized by the conserved motifs. The adenine ring interacts with Phe630 of the N domain, whereas the γ-phosphate group interacts with Asp513 and Thr515 (DKTG motif), Asn881, and Asp878 at the phosphorylation site of the P domain, in cooperation with a Mg^{2+} ion (E1-ATP and E1P-ADP in Figure 3-13B). All of these domains adopt the same rearrangement in the AlF_4^--ADP-bound structure, but the N and P domains are more tightly bridged by ADP and AlF_4^-. The two structures are almost identical with a 0.99 Å RMSD and both represent the E1 state (Figure 3-10E), which is defined as a low affinity state to the substrate polyamines. Moreover, MD simulation of E1 state in the absence of nucleotides (E1(apo) state) showed essentially similar structures to E1-ATP state and E1P-ADP state except fluctuation in ATPase domain, representing autophosphorylation without notable structural changes in E1 states (Figure 3-13A). In contrast, the two phosphate analogues, BeF_3^- and AlF_4^-, captured ATP13A2 in the substrate-bound E2P(SPM) (modeled as a likely substrate, spermine: SPM) and E2Pi(SPM) states, respectively (Figures 3-10C-D, 3-13A). BeF_3^- is covalently attached to the carboxylate side chain of Asp513, in coordination with a Mg^{2+} ion, and tethers the A domain to the phosphorylation site through the backbone carbonyls of Thr346 and Gly347 in the conserved TGES motif (E2P(SPM) in Figure 3-13B). AlF_4^- similarly occupies the phosphorylation site (E2Pi(SPM) in Figure 3-13B). Due to the moderate resolutions of the two structures, it was difficult to determine the exact coordination of BeF_3^- and AlF_4^-. Therefore, I modeled these analogues according to the previous high-resolution structures of SERCA bound to the same analogues (PDB IDs: 3B9B, 3B9R)[69]. The two structures are almost identical with a 0.80 Å RMSD and both represent the E2 state (Figure 3-10G), which is defined as a high affinity state to the substrate polyamines.

In both E2P(SPM) and E2Pi(SPM) structures, a long tunnel is created between the M1-M2 and M4-M5 segments, in which an elongated density probably corresponding to substrate polyamine was observed (Figures 3-14A, 3-15A). This tunnel is rendered electronegative by several carboxylate residues, such as Asp254, Asp463, Asp960 and Asp967, and polyamine is directly recognized by these residues and additionally by aromatic residues, such as Trp251, Tyr256, Tyr940, and Phe963 (Figure 3-14B,C). The observed elongated density is likely SPM added to

the specimen, as similarly observed in the recently-reported structure of yeast homologous protein[164]. However, I cannot exclude the possibility of SPD or other endogenous polyamines contaminated in the sample. The substrate binding cavity of ATP13A2 is larger than those of P2-type ATPases, such as SERCA[67], and a P4-ATPase (ATP8A1)[86], but rather smaller than that of P5A ATPase (yeast Spf1)[91], which is suggested to catalyzes the translocation of α-helical peptides (Figure 3-15B-E).

To assess the functional roles of the residues constituting the substrate-binding cavity of ATP13A2, I measured the ATPase activities of their mutants in collaboration with Dr. Daiho from the Asahikawa Medical University. Almost all ATP13A2 mutant showed decreased SPM-dependent ATPase activity, while retaining the ability to form EP (phosphoenzyme) (Figure 3-14D,E), confirming the integrity of the mutant proteins and thus revealing their substantial contributions to the ATPase activity. In general, the transport substrate of P-type ATPases is recognized by specific interactions near the central TM4 kink[66,80–82,86]. In contrast, in ATP13A2, SPM is recognized by broad interactions through several negatively-charged and aromatic residues surrounding the luminal tunnel (Figure 3-14B). This recognition manner is unique in ATP13A2 and explains its broad specificity, with the preference for longer polyamine species[92].

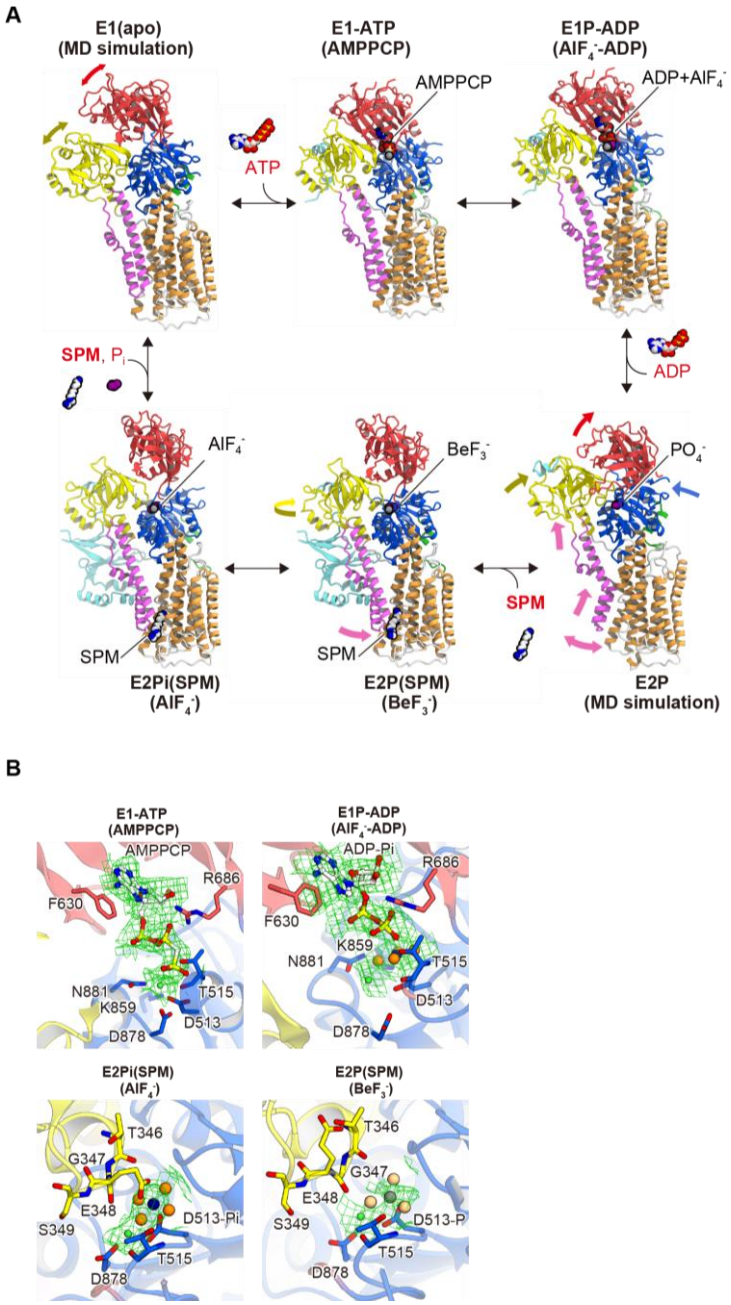

Figure 3-13 | Conformational changes of ATP13A2 during the transport cycle.

(**A**) Transport cycle of ATP13A2. Respective conformations are captured by AMPPCP (E1-ATP state), AlF_4^--ADP (E1P-ADP state), BeF_3^- (E2P(SPM) state), and AlF_4^- (E2Pi(SPM) state). For the E1(apo) state, the snapshot at 200ns of the MD simulation of the E2P state in the absence of nucleotide is indicated. For the E2P state, the snapshot at 200ns of the MD simulation of the E2P state in the absence of SPM is indicated.

(**B**) Cryo-EM densities of the inhibitors are shown. AMPPCP and ADP are shown as sticks, and AlF_4^- and BeF_3^- are shown as spheres. Magnesium ion is shown as a small green ball. Densities are shown as green meshes, contoured at 3.5σ. Residues involved in the inhibitor binding are shown in sticks.

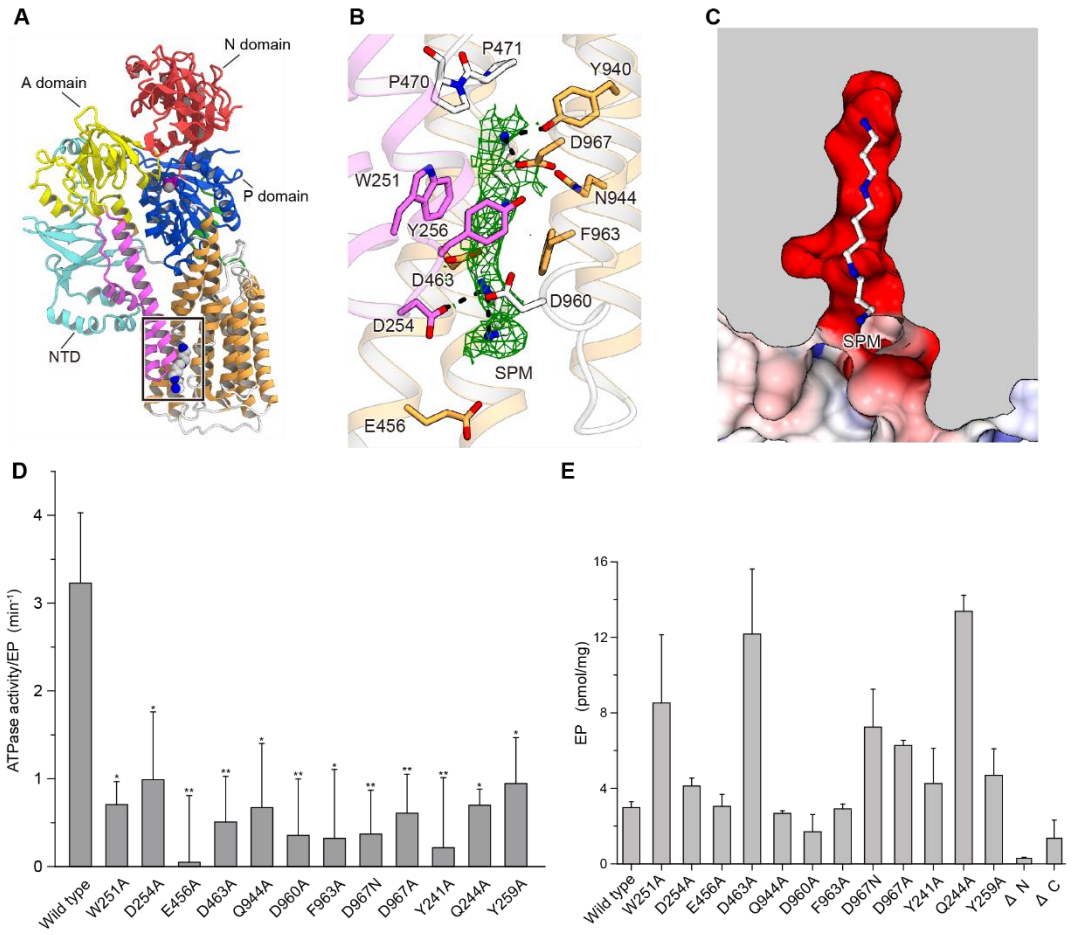

Figure 3-14 | SPM recognition by ATP13A2.

(**A**) Overall structure of ATP13A2 in the BeF_3-stabilized SPM-bound state. The ribbon representation of the BeF_3-bound state is viewed parallel to the membrane. The SPM binding site is highlighted by a black rectangle. (**B**) Close-up view of the SPM binding site in the BeF_3-bound ATP13A2 cryo-EM map. Amino acid residues involved in SPM recognition and two proline residues (Pro470 and Pro471) in the PPAL motif are shown as stick models. Dashed black lines indicate the hydrogen bonds between ATP13A2 and SPM. (**C**) Cut-away molecular surface representation of the SPM binding site. The molecular surface is colored according to the electrostatic potential, ranging from blue (+20 kT/e) to red (−20 kT/e), where kT is the thermal energy and e is the elementary charge. (**D**) ATPase activities of ATP13A2 for the wild type and mutants. The SPM-dependent ATPase activities of each mutant are normalized by the amount of the phosphoenzyme (EP) formation. These values show the turnover rates of the accumulated E2P in the wild type and mutants. The amount of EP formation for each mutant is shown in Figure 3-14E. Data represent the mean ± SEM of three to six measurements. Statistical significance compared with the wild type is shown: *, $p < 0.05$; **, $p < 0.005$. (**E**) The amount of phosphoenzyme (EP) formation was measured using microsomes expressing wild type or mutant ATP13A2. Microsomes were incubated with [γ-^{32}P]ATP at

37 °C for 1 min without substrate polyamines, but in the presence of 0.125 mM PIP_2 and 0.125 mM PA. Under these conditions, all of the mutants, as well as the wild type, accumulate the phosphoenzyme at the steady state. The steady level of EP reflects that of the active, expressed ATP13A2. The reaction was quenched with ice-cold trichloroacetic acid containing P_i. The amount of EP formation was determined as described in the Methods section. Data represent the mean ± SEM of three to five measurements.

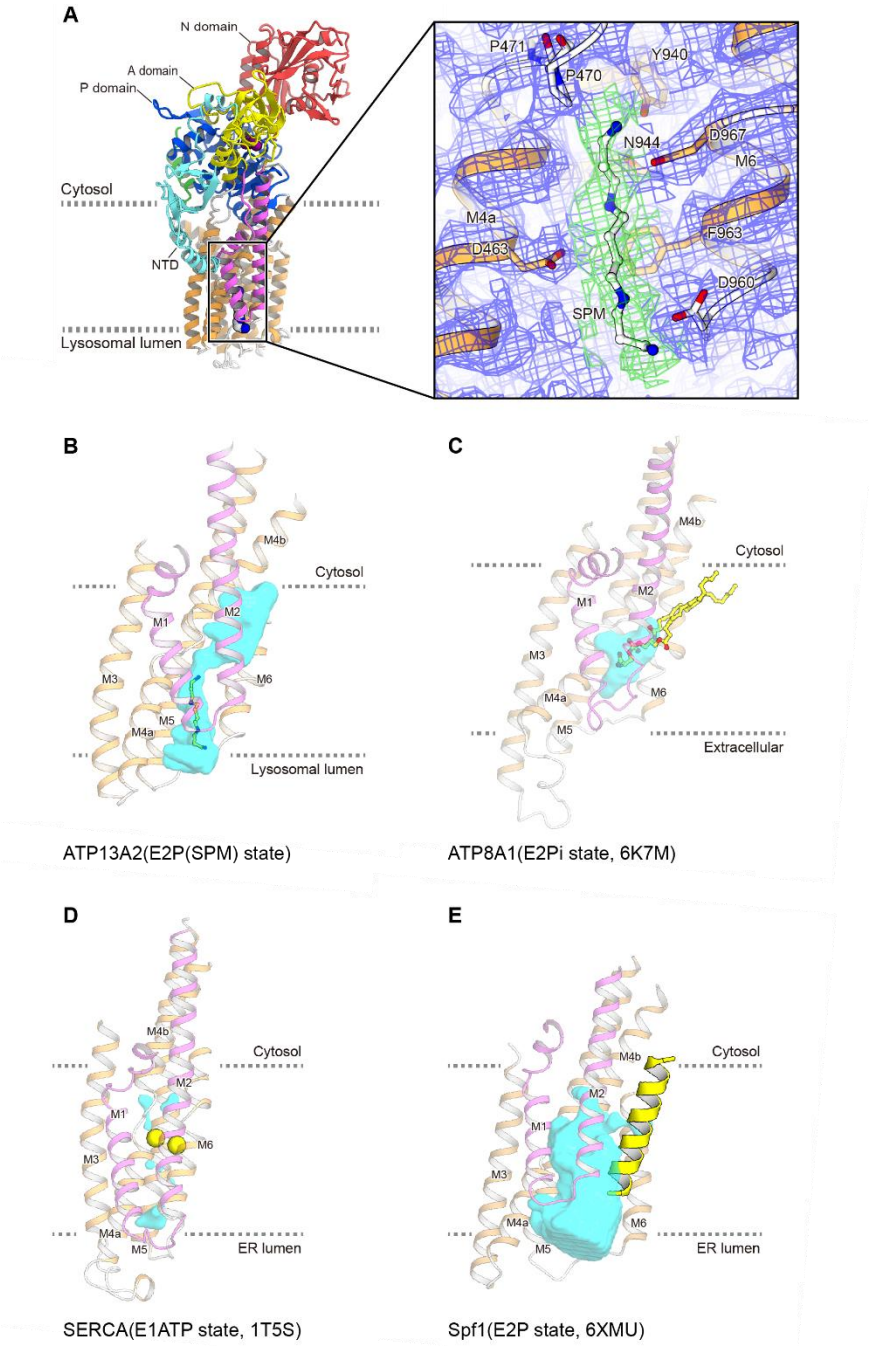

Figure 3-15 | Substrate binding pockets of ATP13A2 and other P type ATPases.

(**A**) Cryo-EM density of the bound SPM and the surrounding residues of ATP13A2. Densities are shown as blue (ATP13A2) and green meshes (SPM). (**B-E**) Protein internal cavities of ATP13A2 (BeF_3^--bound E2P(SPM) state) (**B**), ATP8A1 (PDB ID: 6K7M, AlF_4^--bound E2Pi state) (**C**), SERCA (PDB ID: 1S5T, AMPPCP-bound E1ATP state) (**D**), Spf1 (PDB ID: 6XMU, BeF_3^--bound E2P state) (**E**) were analyzed by the program HOLLOW[165]. The cavities are illustrated as cyan surface representations. Transporting substrates are shown in yellow.

3.3.6 Polyamine Transport Mechanism

The structural comparison of the E2P(SPM) (BeF_3^-) and E1P-ADP (AlF_4^--ADP) states revealed the conformational changes upon the E1 to E2 transition: a large dislocation of the N domain, an inclination of the P domain against the membrane plane, and upward (toward the cytoplasmic side) and rotational movements of the A domain (Figures 3-16A, 3-10F, SI Movie1 in the original paper). The rearrangement of these cytoplasmic domains induces extensive rearrangements in the TM region; specifically, a slight inclination of the cytoplasmic portions of the M5 and M4b segments and a large upward and rotational movement of the M1-M2 segments (Figure 3-16B). The latter changes in the M1-2 segments directly induce the luminal gate opening, by creating a tunnel between the M1-M2 and M4-M5 segments, and thereby allowing SPM entry (Figure 3-17 A,B).

In most P-type ATPases, substrate binding from the extracellular/luminal side (protons in SERCA, phospholipids in P4-ATPase) involves sequential steps (Figure 3-17 C,D) through the E1P, E2P and E2Pi intermediates, which structurally involve the A domain rearrangement toward the phosphorylation site, and the binding of substrates. While the first step is coupled to (or induced by) the phosphorylation, the extracellular/luminal substrate binding in the second step is coupled to the dephosphorylation reaction (Figure 3-18)[69,70,76]. The two phosphate analogues, BeF_3^- and AlF_4^-, have different coordination geometries, which accordingly allow the enzyme to be captured in different intermediate states; namely, the phosphorylated E2 state (E2P) and its hydrolyzed intermediate (E2Pi) (Figure 3-18C,D)[69,70,86]. In SERCA, the dephosphorylation reaction during this E2P to E2Pi transition is coupled to the luminal proton binding (and simultaneous Ca^{2+} release into the lumen), which involves the rearrangement of the hydrogen bonding network in the substrate binding site (Figures 3-17C, 3-18C)[69,70]. In P4-ATPase (ATP8A1), phospholipid binding only induces the sliding of the M1-2 segments, which is coupled to the A domain rearrangement and thus facilitates dephosphorylation (Figures 3-17D, 3-18D). However, in ATP13A2 the current BeF_3^-- and AlF_4^--stabilized SPM-bound structures are essentially the same, including the A domain orientation toward the P domain (Figure 3-10C,D). Furthermore, Glu348 (TGES motif) is in the proximity of the phosphoryl group attached to Asp513 (DKTG motif) in both structures, which is a signature coordination for dephosphorylation (E2P(SPM) and E2Pi(SPM) in Figure 3-13B). Considering the SPM-dependent ATPase activity of ATP13A2, it is most likely that the substrate binding stabilizes the M1-2 segments and the A domain in their current positions, to facilitate the dephosphorylation reaction. (Figure 3-18A,B). MD simulations using the structure of the E2P(SPM) state as the initial model revealed that the M1-2 segments adopt flexible conformations in the absence of SPM but become stabilized with the SPM in the positions observed in the cryo-EM structures (Figure 3-19), further supporting our notion. It should also be noted that, in ATP13A2, Tyr259 on the M2 segment, participating in the

hydrogen bonding network in the E1 state, dislocates upon the E2 transition and constitutes the luminal tunnel for the SPM binding (Figure 3-17A,B), suggesting that it plays an essential role in the SPM-dependent dephosphorylation. Consistently, the mutation of Tyr259 greatly decreases the ATPase activity of ATP13A2 (Figure 3-14D). These results together indicate that the M1-2 segments serve as the "connector" that enables the structural coupling between the polyamine binding and the A domain rearrangement in ATP13A2. This mechanism somewhat resembles that of ATP8A1, as it also induces the M1-2 shift upon phospholipid binding (Figure 3-18D), consistent with the evolutional relationship between the P4 and P5 subfamilies (SI Movies2 and 3 in the original paper).

ATP13A2 has the unique N- and C-terminal domains (NTD and CTD), which are both likely to contribute to the structural stability. However, while the NTD deletion severely affects the phosphoenzyme (EP) formation, the CTD deletion only moderately affects the EP formation (Figure 3E), suggesting their distinct roles. The NTD contains several clusters of positively-charged residues, which presumably constitute binding sites for PA and PIP_2 (Figure 3-11)[62]. The current structures reveal the proximity of these residues to the lipid boundary (Figure 3-20A). According to the previous study, phosphorylated ATP13A2 preferentially adopts the E1P conformation, but supplementation with these lipids advances the reaction cycle to the E2P conformation[62]. Therefore, the binding of specific lipids, such as PA and PIP_2, probably stabilizes the interaction of the NTD with the lipid membrane and thereby affects the E1P to E2P transition upon phosphorylation (Figure 3-20B). Consistently, the NTD is visible only in the E2P conformations (BeF_3^- and AlF_4^-), whereas it is almost completely disordered in the E1 conformations (AMPPCP and AlF_4^--ADP) (Figure 3-10), indicating the role of the NTD in the stabilization of the E2P conformation, although I cannot rule out the possibility that it is merely an artifact derived from the GDN micelles.

In the current SPM-bound structures, SPM is stuck at the central kink in the M4 helix and still exposed to the lumen (Figure 3-14B,C). According to our simulation, the water solvent access cavity is discrete near the M4 kink, and the polyamine-permeating tunnel is sealed on the cytoplasmic side by several lipid molecules (Figure 3-21A–D). Therefore, further conformational changes are required to transport SPM completely to the cytoplasmic side. ATP13A2 has two sequential Pro residues, which create a larger M4 kink, whereas other P-type ATPases have only a single Pro residue at the corresponding position (Figure 3-22A–C). Yeast P5A ATPase (Spf1) similarly has two Pro residues and undergoes a large sliding of the cytoplasmic M4b segment upon substrate transport (Figure 3-22D). Our mutation analysis has illustrated the cytoplasmic exit pathway of ATP13A2 (Figure 3-14D, Figure 3-21). For example, mutations of the hydrophilic and aromatic residues on the M2 helix, such as Tyr241 and Gln244, decreased the SPM-dependent ATPase activity (Figure 3-14D). Altogether, these results suggest that SPM is transported along

the cleft between the M1-2 and M4-6 helices, and this transport is probably associated with the sliding of the cytoplasmic M4b segment that restricts the exit pathway in the current E2P and E2Pi structures (Figure 21E,F).

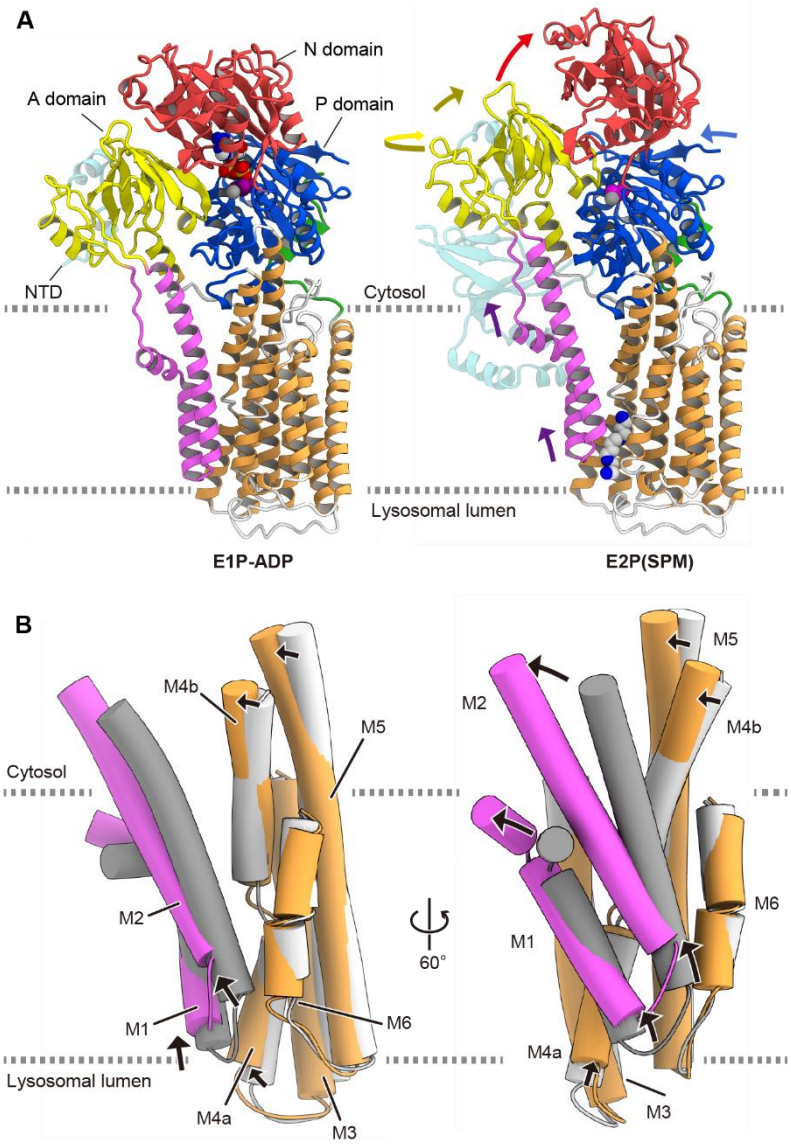

Figure 3-16 | Structural dynamics of E1P-ADP state to E2P(SPM) state transition in ATP13A2.

(**A**) Ribbon model representation of the E1P-ADP state and the BeF_3^--bound E2P(SPM) state are shown. Structural changes of the A, N, and P domains and the M1-2 helices are indicated by arrows with the same colors as the model. (**B**) Close-up view of the TM segments. Conformational changes of M1-6 from the E1P-ADP state (grey) to the E2P(SPM) state (colored). Structures are aligned on the M5-M10 helices. The rearrangements of the TM helices are indicated by black arrows.

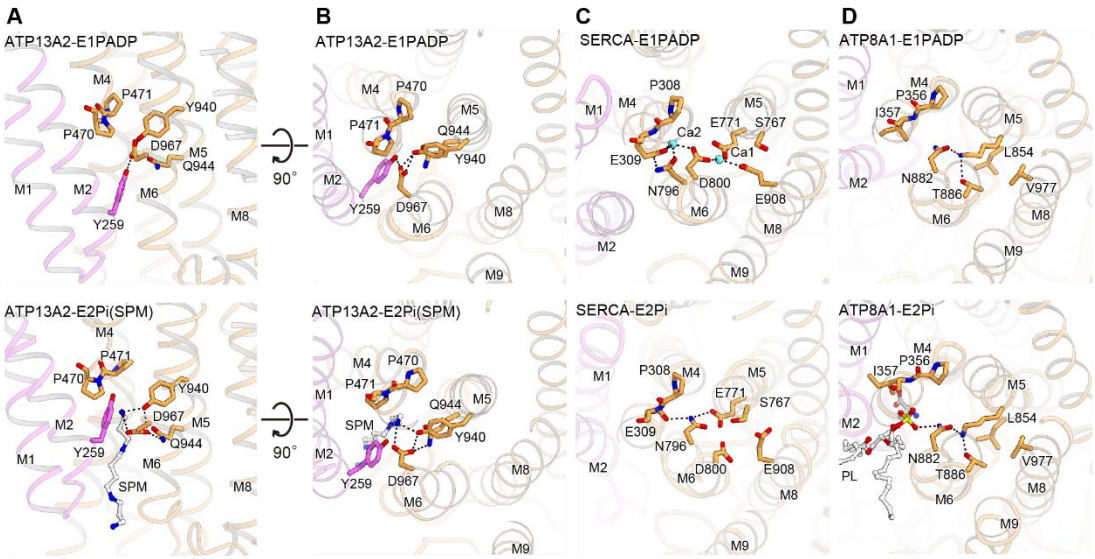

Figure 3-17 | Comparison of the substrate binding sites.

(**A**,**B**) Polyamine binding site of ATP13A2 in the SPM-unbound state (top: E1P-ADP) and the SPM-bound state (bottom: E2Pi(SPM)), viewed from within lipid membrane (**A**) and from the cytoplasmic side (**B**). Residues involved in SPM transport are shown as ball-and-stick representations. Hydrogen bonds are shown as black dashed lines. (**C**) Ca^{2+}/H^{+} binding site of SERCA in the Ca^{2+}-bound state (top: PDB ID 1T5T) and the counter-transporting H^{+}-bound state (bottom: PDB ID 3B9R), viewed from the same viewpoints as in (**B**). Residues involved in the substrate binding are shown as ball-stick representations. Hydrogen bonds are shown as black dotted lines, and the bound Ca^{2+} ions are cyan spheres. (**D**), Phospholipid binding site of ATP8A1 in the E1PADP phospholipid unbound state (top: 6K7K) and the E2Pi phospholipid-bound state (bottom: 6K7M), from the same viewpoints as in (**B**). Residues involved in phospholipid translocation are shown as ball-and-stick representations. Hydrogen bonds are shown as black dotted lines.

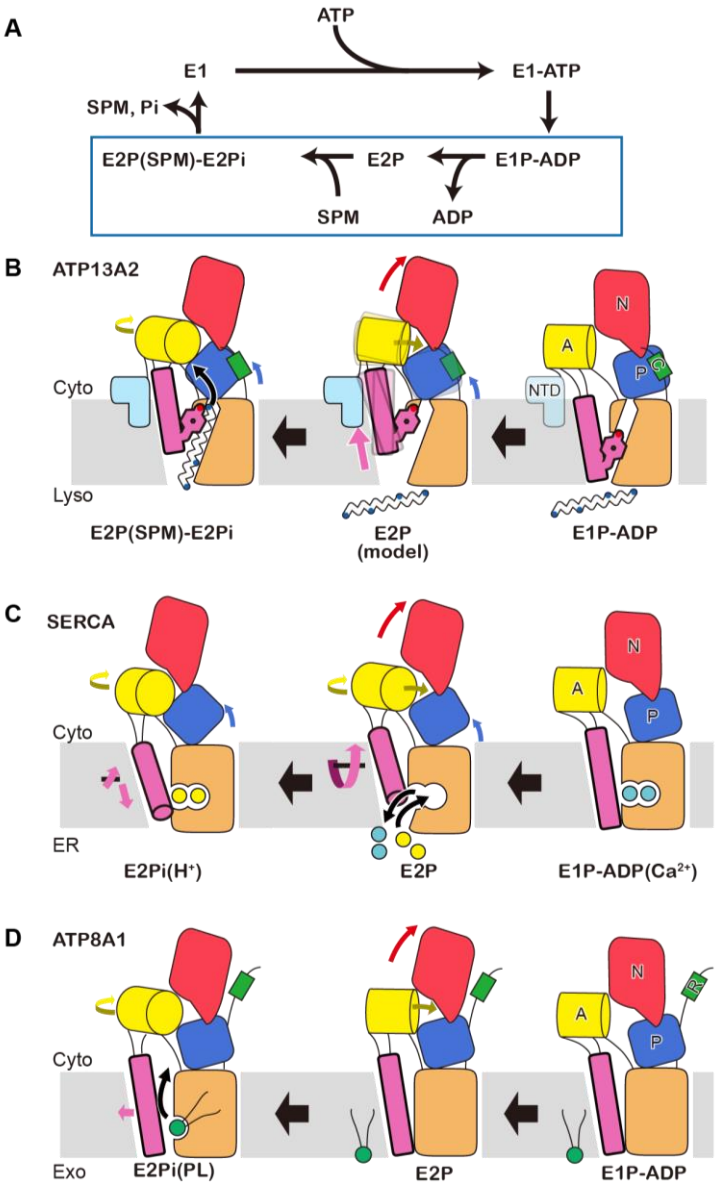

Figure 3-18 | Proposed mechanism of SPM transport by ATP13A2.

(**A**) Transport cycle of ATP13A2. P-type ATPases generally follow the Post-Albers scheme. Phosphorylation induces the transition of the two states, E1 and E2, which are defined as high affinity states for cytoplasmic and luminal/extracellular substrates, respectively. Binding of the luminal/extracellular substrate (SPM in ATP13A2) requires sequential steps in most P-type ATPases, through E1P, E2P and E2Pi intermediates, as indicated in the blue rectangle. (**B**-**D**) Schematic models of luminal/extracellular substrate binding during the transport cycles in ATP13A2 (**B**), SERCA (**C**), and ATP8A1 (**D**). Rearrangements of the cytoplasmic domains are indicated by arrows. Domain movement is coupled to the phosphorylation and dephosphorylation of the P domain, which alternately changes the substrate affinity of the enzyme. Despite the overall similarity in the reaction scheme, there are variations in the conformational changes among the members.

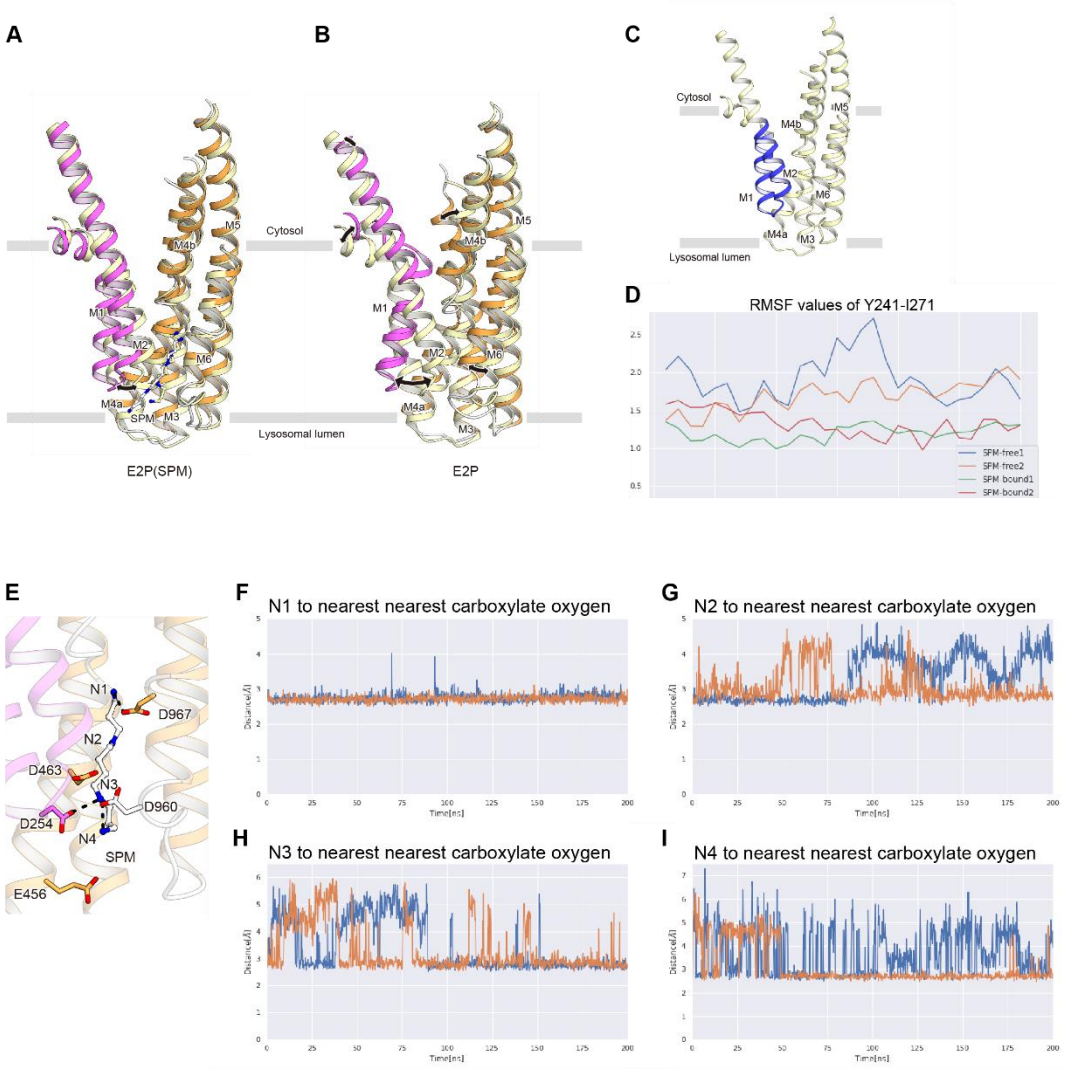

Figure 3-19 | Stabilization of the M1-2 helix upon SPM binding.

(**A-B**) Close-up view of the TM segments during MD simulations of ATP13A2 in complex with SPM (A) and in the absence of SPM (**B**). Conformational changes of M1-6 from the 0 ns (cream) to the 200 ns (colored) in 200 ns non-equivalent MD simulations are represented. Structures are aligned on the M5-M10 helices. The rearrangements of the TM helices are indicated by black arrows. (**C-D**) The flexible region (Y241-I271) of the M1-2 helices is indicated in blue. These residues show high flexibility during the simulation in the absence of SPM (**C**). RMFSs of the residues Y241-I271 during the 200ns MD simulations of ATP13A2 in complex with SPM (green and red lines) and in the absence of SPM (blue and orange lines). The simulations were performed twice for each condition. Structures are aligned on the M5-M10 helices for the RMFS calculation. (**E**) Close-up view of the SPM binding site. Acidic residues involved in SPM recognition are shown as stick models. (F-I) Distance from the nearest carboxylate oxygen is shown for four nitrogen atoms of SPM, N1 (**F**), N2 (**G**), N3 (**H**), and N4 atom (**I**).

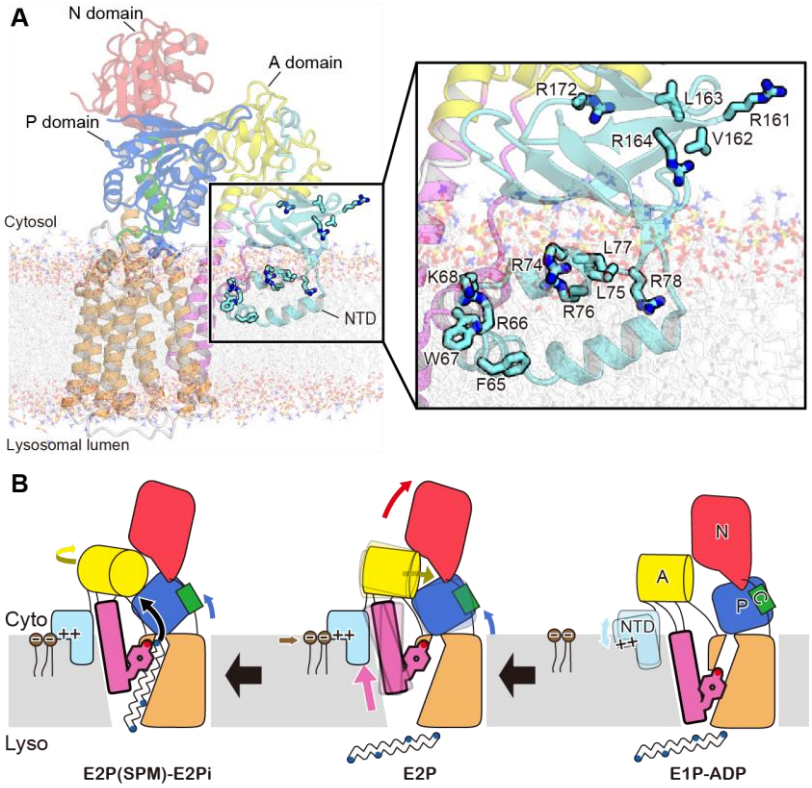

Figure 3-20 | Proposed model for lipid-facilitated transport of ATP13A2 mediated by NTD.

(**A**) ATP13A2 embedded in a lipid bilayer, using coarse-grained simulation, is shown. Lipids are shown in ball and stick representations. Amino acid residues in the predicted lipid binding sites are shown in thick stick representations.

(**B**) Proposed model for the lipid-facilitated E1P to E2P transition during the transport cycles in ATP13A2. Binding of negatively charged lipids, such as PA and PIP2, stabilize NTD to facilitate the E1P to E2P transition upon phosphorylation. Schematic model of ATP13A2 is illustrated as in Figure 3-18B, and PA and PIP2 are shown in brown.

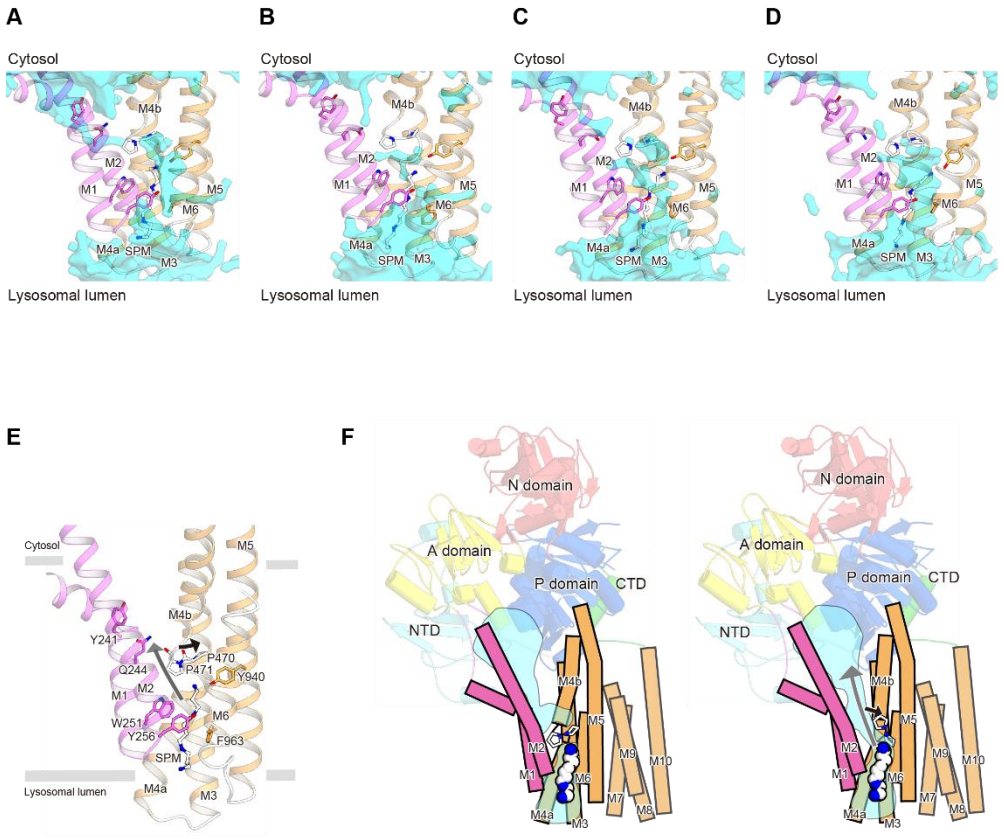

Figure 3-21 | SPM permeation pathway of ATP13A2.

(**A-D**) Water accessible cavity of ATP13A2 in the MD simulation under E2Pi(SPM) condition. Each picture represents 50 ns (**A**), 100 ns (**B**), 150 ns (**C**), and 200 ns (**D**), in 200 ns MD simulations. (**E**) Proposed model of the SPM exit pathway. Amino acid residues important for the SPM-dependent ATPase activity are shown in stick representations. The predicted SPM exit pathway and the conformational change of M4b associated with SPM transport are illustrated with gray and black arrows, respectively. (**F**) Schematic model of the SPM transport by ATP13A2. The predicted SPM permeation pathway is illustrated with a grey arrow in the current E2Pi(SPM) structure. The proposed conformational change is shown as cartoons. The M4b shift coupled to the SPM transport is indicated by a black arrow.

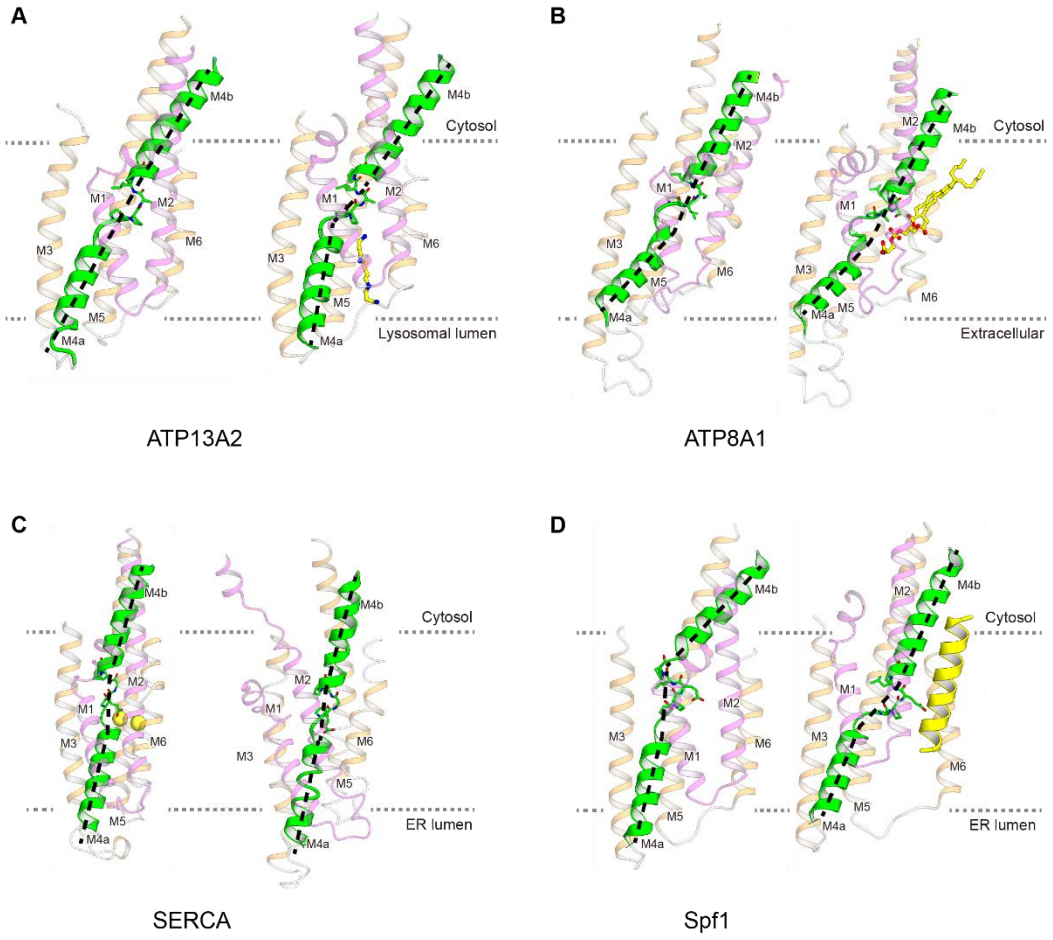

Figure 3-22 | M4 kink in ATP13A2 and other P type ATPases.

Conformational changes of the M4 helix upon the E1 to E2 transition are shown for ATP13A2 (**A**), ATP8A1 (E1-ATP: PDB ID 6K7J and E2P: PDB ID 6K7M) (**B**), SERCA (E1-ATP: PDB ID 1T5S and E2P: PDB ID 3B9R) (**C**), and Spf1 (E1-ATP: PDB ID 6XMQ and E2P: PDB ID 6XMU) (**D**). M1-6 helices are shown with M4 highlighted in green, and the helix kink is indicated by the dashed lines.

3.4 Discussion

3.4.1 Comparison between P5A and P5B ATPases

ATP13A2 consists of a general P-type ATPase fold and additional NTD and CTD domains. While the overall architecture is similar to that of yeast P5A-ATPase (Spf1), there are significant differences between the two P5 ATPase clades, P5A and P5B. Firstly, each transporter adopts the suitable binding cavity conformation for the respective substrate. ATP13A2 has a long negatively-charged tunnel for polyamine permeation, whereas Spf1 would have a wide cavity beside the TM segments, which enables the translocation of incredibly large α-helical peptide substrates (Figure 3-22)[91]. Most notably, the current structures of ATP13A2 revealed that the NTD adopts a stable conformation only in the E2P state with its hydrolyzed intermediate, E2Pi, thus highlighting its role in facilitating the E1P to E2P transition. The NTD is likely to activate the transport activity by stabilizing the high affinity state for the polyamines. Furthermore, the facilitating role of the NTD is accelerated by the binding of specific lipids, such as PA and PIP_2, and the activation switching by these lipids is implicated in the protection from mitochondria stress and thus in Parkinson's disease[62]. While the NTD is commonly conserved in the P5 ATPases, this regulatory role of the NTD is only proposed in the P5B ATPases, including ATP13A2, and not in the P5A ATPases, indicating the distinct functions between the two sub-clades. Furthermore, the current findings may offer a rational strategy for neuroprotective therapy, by activating ATP13A2.

3.4.2 SPM transport cycle and remaining issues

In this thesis, I determined the cryo-electron microscopy (cryo-EM) structures of human ATP13A2 under four different conditions: the non-hydrolyzable ATP analog AMPPCP-bound state (E1-ATP), the ADP-Pi (Pi: inorganic phosphate) analog AlF_4^--ADP-bound state (E1P-ADP), the BeF_3^--bound state in complex with spermine (E2P(SPM)), and the AlF_4^--bound state in complex with SPM (E2Pi(SPM)). These structures, together with biochemical and computational analyses, have revealed the unique mechanisms of polyamine recognition and transport by ATP13A2 (Figure 3-23).

In the transport cycle, the M1-2 helices played an important role. The structural comparison between the E1 and E2 states showed upward movement of M1-2 helices upon phosphorylation in the E2 states. This upward movement of the M1-2 helices forms a SPM binding pocket on the luminal side of the lysosome, resulting in the formation of the E2 states with high SPM affinity. Furthermore, I proposed SPM binding to the SPM binding pocket leads to the formation of intermediates (E2P(SPM)-E2Pi(SPM)) that promote dephosphorylation, explaining SPM dependent ATPase activity. After dephosphorylation, Phosphate and SPM were released to cytosol and returns to the E1 state. In summary, I have elucidated the SPM transport cycle driven by the energy of ATP hydrolysis.

However, how ATP13A2 release SPM is still elusive due to lack of structural information of E2 state just after release of phosphate and SPM. Considering SPM transport mechanism described above, two types of SPM release models can be proposed. In the first model, similar to other P-type ATPases, ATP13A2 also adopts altering access mechanism to release SPM (Figure 3-24A). In this model, ATP13A2 opens SPM binding pocket to either the lysosomal luminal side (outward open, E2P-E2P(SPM) state) or cytoplasmic side (inward open, E2 state (model)) and simultaneously seals the opposite side. Most transporter adopting altering access mechanism forms an occluded state, in which substrate binding pocket is inaccessible from either side of the transport direction[166]. Considering the size of SPM and SPM binding pocket, it is difficult to form a complete occluded state. Therefore, it is reasonable that ATP13A2 would forms partially occluded state to achieve altering access mechanism. This altering access mechanism is consistent with previously reported P-type ATPases, explaining uphill SPM transport mechanism[70,73–91]. In the second model, unlike other P-type ATPases, ATP13A2 adopts channel-pump mechanism to release SPM (Figure 3-24B). In this model, ATP13A2 forms open channel-like state, in which SPM binding pocket is accessible from both lysosomal luminal side and cytoplasmic side. This opening pore may allow continuous SPM flux to the cytosol like other cation channels. The ATP dependent channel-pump mechanism in ATP13A2 is similar to that of the ATP-binding cassette (ABC) transporter cystic fibrosis transmembrane conductance regulator (CFTR), a Cl^- channel gated by ATP hydrolysis[167]. However, there is a difference between the channel-pump mechanism in ATP13A2 and channel mechanism in CFTR. ATP13A2 requires lysosomal SPM binding to facilitate dephosphorylation and transport cycle, while CFTR does not require Cl^- to facilitate transport cycle. This SPM dependency and physiological ATP conditions and membrane potential could facilitate unidirectional transport cycle, explaining unidirectional SPM transport mechanism. To verify which model is true, further studies on the structure and stoichiometry of the coupling between SPM transport and ATP hydrolysis are needed.

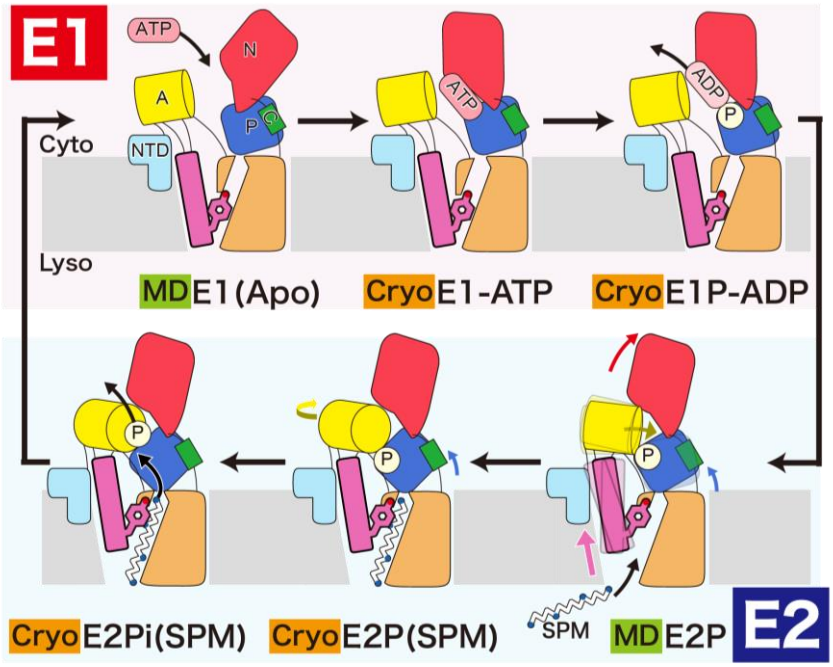

Figure 3-23 | Schematic picture of ATP driven SPM transport cycle by ATP13A2.

ATP13A2 follows Post-Albers scheme common in P-type ATPases. Phosphorylation induces the transition of the two states, E1 and E2, low affinity states for SPM and high affinity states for SPM, respectively. The upward movement of M1-2 helices upon phosphorylation forms the E2 states with high SPM affinity. SPM binding to the E2P state leads to the formation of intermediates (E2P(SPM)-E2Pi(SPM)) that promote dephosphorylation, facilitating transport cycle.

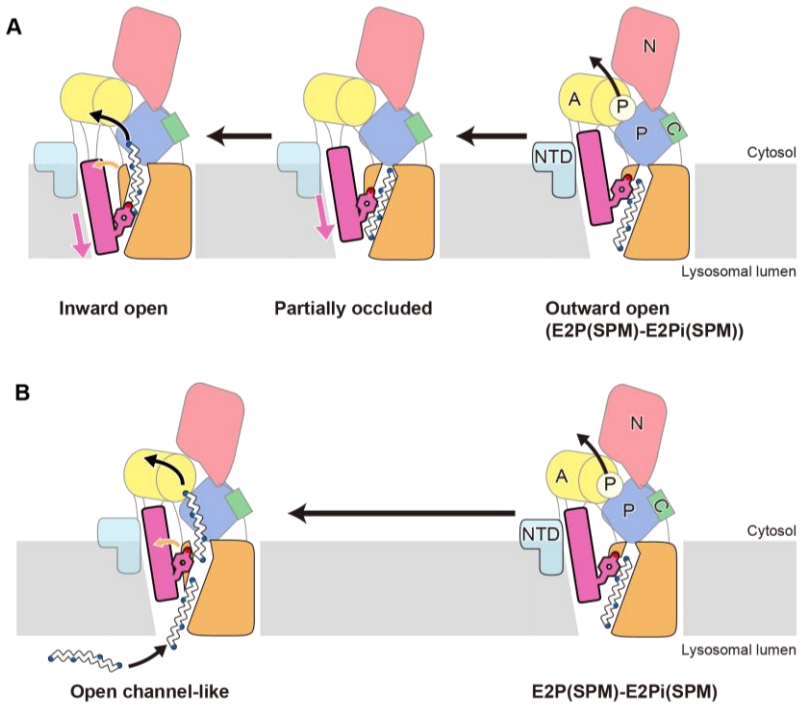

Figure 3-24 | Two proposed SPM release models in ATP13A2.

Schematic pictures of two proposed SPM release models in ATP13A2 are shown. (**A**) SPM release model based on Altering access mechanism. In this model, SPM binds to ATP13A2 in the outward open E2P(SPM) state, facilitating dephosphorylation and phosphate release. Following structural changes form partially occluded state to close luminal gate, further structural changes completely close luminal gate and open cytosolic side to release SPM. (**B**) SPM release model based on channel-pump mechanism. In this model, SPM binding to E2P(SPM) state induces structural changes to form open channel-like pore to the SPM binding pocket. This opening pore may allow continuous SPM flux to the cytosol like other cation channels.

3.4.3 Limitation of this study

First, our assay of the SPM-dependent ATPase activity in microsomes showed an unexpected inhibition by high-concentration SPM, which is not reported previously. It seems that the transport and/or ATPase activity of ATP13A2 could be affected by several factors, such as specific lipid binding to the NTD. The result might also suggest unidentified regulators contaminated in the microsomes sample. Complicated regulation in cellular context would be the remaining issues in the studies of P5-ATPases.

Second, probably due to the flexible nature of ATP13A2 in GDN micelles, only the two distinct conformations could be captured, even under four different conditions. Most notably, the two phosphate analogs, BeF_3^- and AlF_4^-, capture ATP13A2 in the almost same conformations, corresponding to the SPM-bound hydrolyzing intermediate, indicating the high flexibility of ATP13A2 in the E2P conformation without polyamines. In addition, the elongated shape of the density in such moderate resolution maps is not sufficient to identify detailed interactions and to understand precise mechanism for the polyamine recognition. Particularly, the structural information upon substrate release to the cytosol is completely lacking. Therefore, further investigation of structural and biochemical studies is required.

Chapter 4 Concluding remarks

4.1 Summary of the thesis

In this thesis, I succeeded in obtaining structural insights into the molecular mechanism of membrane transport proteins that maintain intracellular homeostasis by utilizing ATP in different ways: ATP modulated Mg^{2+} homeostasis by MgtE, and SPM transport by ATP13A2 driven by the energy of ATP hydrolysis.

In this thesis, I employed various approaches including structural analysis, ITC, electrophysiological analysis, biochemical analysis, in vivo assay, and MD simulation. In particular, the structural analysis was performed by making the best use of the advantages of two methods: X-ray crystallographic analysis and cryo-EM single particle analysis.

In Chapter 2, I employed X-ray crystallography to reveal the detailed molecular mechanism of ATP modulated Mg^{2+} homeostasis by MgtE. X-ray crystallography has been used for many years as a royal method for structural analysis[168]. X-ray crystallography has the advantage of elucidating molecular interactions and side chain orientations in detail using high-resolution density maps. In addition, X-ray crystallography also has the advantage that we could obtain structural information of specific domains at higher resolution using constructs containing specific domains of the protein. In Chapter 2, I combined the X-ray crystal structure analysis of the full-length MgtE-ATP complex and the higher-resolution X-ray structural analysis of the cytoplasmic domain of MgtE-ATP complex to discuss the detailed coordinates of ATP and Mg^{2+} in the MgtE-ATP complex. These structures, together with functional studies revealed that the negative charges derived from the phosphate groups of ATP would allow the MgtE cytosolic domain to attract more positive charges, thus tuning the affinity of the MgtE cytosolic domain for Mg^{2+} within a physiological range. Our findings revealed intracellular Mg^{2+} homeostasis is modulated by ATP at the functional and structural levels, providing significant insights into the modulatory effects of ATP on intracellular homeostasis.

In Chapter 3, I employed cryo-EM single particle analysis to reveal recognition and structural dynamics of ATP13A2 in SPM transport cycle. Cryo-EM single particle analysis had been used for many years as a method to capture low-resolution structures of large proteins. However, with the recent development including advanced detectors and software, the "resolution revolution" was accomplished, cryo-EM is now commonly used to determine the structures of membrane proteins with molecular a mass of ~100 kDa, such as the P-type ATPases discussed in this thesis[169]. Compared to X-ray crystallography, cryo-EM has the advantage of being able to reveal flexible and dynamic protein structures. In Chapter 3, I performed cryo-EM single particle analysis of transport intermediates of ATP13A2. These structures, together with the molecular dynamics

simulations, revealed recognition of SPM and structural dynamics of ATP13A2 in the transport cycle of SPM. SPM was bound at the luminal tunnel and recognized through numerous electrostatic and π-cation interactions, explaining its broad specificity. The upward (toward the cytoplasmic side) movement of M1–2 segments upon auto-phosphorylation forms SPM binding pocket, and following SPM binding would stabilize M1–2 segments, facilitating dephosphorylation. This study provides functional, structural, and molecular dynamics insights into the ATP-dependent transport of polyamines by ATP13A2. These findings may offer a rational strategy for neuroprotective therapy, by activating ATP13A2.

4.2 Insights from other studies

Around the same time as original paper that constitute this thesis, other groups published papers on the functional and structural analysis of the human ATP13A2 and yeast ATP13A2 homolog [151,164,170,171]. In this section, I will discuss further findings and implications obtained from comparison of our original paper with other papers.

4.2.1 Functional role of NTD

From previous studies, NTD was reported as a domain that promotes E1 to E2 transition in a lipid-dependent manner, such as PIP_2 and PA[62]. In our original paper, I determined the cryo-EM structures of the ATP13A2 in the transport intermediates in the absence of PIP_2 and PA. These structures showed that the NTD was flexible in the E1 states while NTD was fixed in the E2 states. Furthermore, in the E2 states, positively charged lipid binding sites were located at the interface of the lipid membrane. From these results, I proposed that NTD would to be anchored in order to form the E2 states, and that the binding of lipids such as PIP_2 and PA would promote the formation of the E2 states by more strongly anchoring the NTD (Figure 3-20).

The other group performed structural analysis of the ATP13A2 in the transport intermediates in the presence of PIP_2 and PA[151,170,171]. Those structures were essentially the same as ours for the ATPase domain, TM domain, and CTD, except for the NTD. In the structures reported by other groups, the structure of the NTD was fixed at the same position during all the transport cycles from the E1 to E2 states (Figure 4-1). Furthermore, the position of the fixed NTD was the essentially similar to the position of NTD in our E2 states.

In addition, cryo-EM structures of Ykp9, an ATP13A2 homologue expressed in yeast vacuoles, was reported (Figure4-2)[164]. While the detailed molecular mechanism of substrate dependence and lipid dependence of Ykp9 has not been elucidated, the structure of Ykp9 in the SPM-bound state was reported in this study. Ykp9 showed the similar structures to the human ATP13A2. However, the lipid-binding sites of human ATP13A2 were not conserved, and the NTD has a long

loop region (auto-inhibitory tail) at the tip. The reported structure suggests that the long loop at the tip of the NTD regulates the activity of yeast Ypk9 by self-inhibition, which would be activated by signals such as lipids. Such a long loop involved in self-inhibition is also observed in P4-ATPase, but not in human ATP13A2. This difference in the function of the NTD may be due to differences in the environment and function of the yeast vacuole and human lysosome.

Since PIP_2 and PA are abundant lipids in normally functioning lysosomes, the role of NTD in human ATP13A2 might be maintaining SPM transport activity of ATP13A2 only when ATP13A2 is present in lysosomes with proper function. Further studies into the lipid regulated transport mechanism would offer insights into the neurological diseases caused by mutations in ATP13A2.

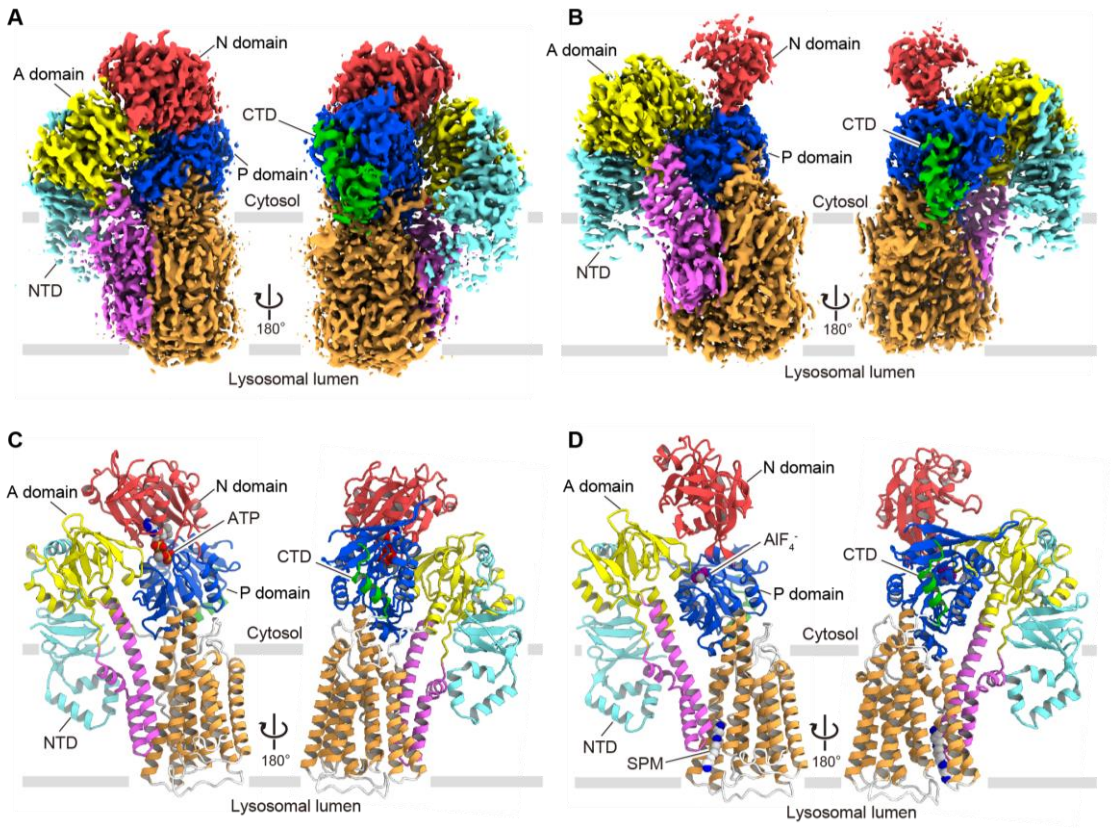

Figure 4-1 | Cryo-EM maps and structures of ATP13A2 in the presence of PIP_2 and PA. (**A-B**) Cryo-EM maps of ATP13A2 in E1-ATP state (EMDB-ID: EMD-24219) (**A**) and E2Pi(SPM) state (EMDB-ID: EMD-24217) (**B**) in the presence of PIP_2 and PA. (**C-D**) Ribbon models of ATP13A2 in E1-ATP state (PDB ID: 7N74) (**C**) and E2Pi(SPM) state (PDB ID: 7N72) (**D**) in the presence of PIP_2 and PA. All models are shown with the same color scheme as in 3-14A.

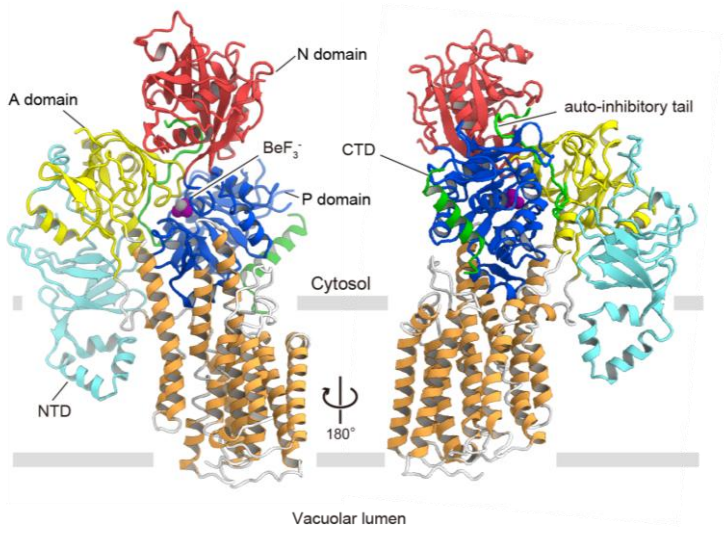

Figure 4-2 | Cryo-EM structures of yeast Ypk9 in the E2P-inhibited state.

Ribbon models of the thermophilic yeast *Chaetomium thermophilum* Ypk9 in E2P-inhibited state (PDB ID: 7OP8). The autoinhibitory tail, which is unique to yeast Ypk9, is shown in light green, and other domains in common with ATP13A2 are shown with the same color scheme as in 3-14A.

4.2.2 Transport mechanism of polyamines by ATP13A2

In this study, I determined cryo-EM structures of ATP13A2 in the transport intermediates in the absence of PIP_2 and PA. These structures were determined under GDN condition, which is more likely to mimic physiological lipidic environment than other typical detergents including DDM, LMNG. Moreover, I obtained structural insight into the structure of the E1(apo) state and E2P state by MD simulation, which was difficult to determine due to their high flexibility.

Among the four groups, Sim et al. succeeded in determining the structures of the E1(apo) and E2P states by stabilizing the structures with DDM-CHS, PIP_2 and PA, and introducing a mutation to the conserved aspartic acid in P domain[151]. Furthermore, it is worth noting that Sim et al. used insect cells as the expression host for ATP13A2. Other three groups including us used human-derived cells as the expression host as proper function of ATP13A2 is confirmed in human cells. It should be also noted that ATP13A2 obtained by Sim et al.'s expression and purification system was highly stable in the E2 states (E2P, E2P(SPM), E2Pi(SPM) states), resulting the structures of E1 states (E1(apo), E1-ATP, E1P-ADP states) could not be obtained in the wild type. Although structures of ATP13A2 in E1(apo) and E2P states in Sim et al. might be artifacts due to the lipids in the insect cells and the conditions of constructs and purification, these structures provide indispensable the structural information of the experimentally obtained E1(apo) and E2P states.

Comparing the snapshot of our MD simulations at 200ns with cryo-EM structure in Sim et al, the structures of the E1(apo) and E2P states are similar conformations (Figure 4-3). In particular, the flowchart of the structural analysis of the E2P state shows an equilibrium with the E2P and E2Pi states, which is consistent with our claim that the E2P state was fluctuating, and SPM binding stabilizes the dephosphorylated intermediate.

It is also very interesting that Tillinghast et al. claimed that ATP13A2 transport protons as a counter ion of SPM, while other groups suggest ATP13A2 does not require any counter ions[171]. Tillinghast et al. claimed that ATP13A2 forms an occlusion pocket in E1 states and the proton acceptor in the occluded pocket is protonated in the E1-states. Indeed, the occlusion pocket was also observed in our structures of ATP13A2 in E1 states and Sim et al.'s structures of ATP13A2 in E1 states. However, the pKa of the Asp967, a probable proton acceptor in the occluded pocket is around 6.0 in our cryo-EM structures of ATP13A2 in the E1 states, indicating that Asp967 does not need to be protonated under physiological conditions. In addition, our MD simulation of the E1(apo) state showed that the occluded structure in the E1(apo) state is stable under unprotonated conditions (Figure 4-4). These results support that occluded structure in the E1 states does not require proton binding. However, further functional and structural analysis of the ATP13A2 in E1 states under various pH conditions is necessary to reach a final conclusion on the proton pumping activity of the ATP13A2.

In summary, the model proposed in this thesis is consistent with other studies.

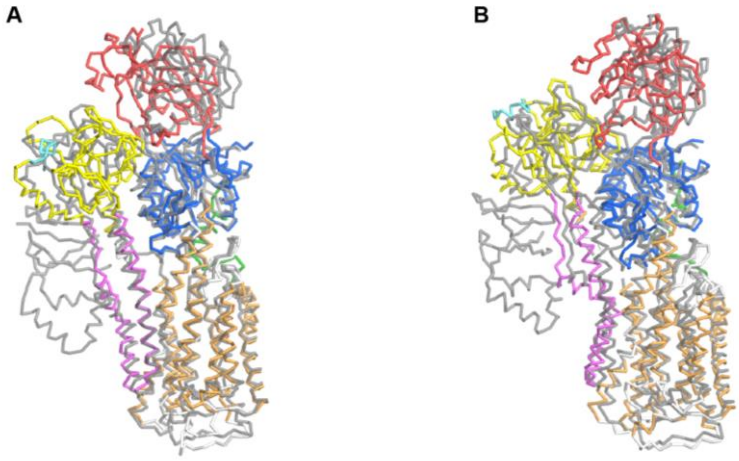

Figure 4-3 | Structural comparison of MD simulations in our original paper with cryo-EM structures of E1(apo) and E2P states.

(**A**) Structural comparison of ATP13A2 between snapshot of MD simulation of E1(apo) state at 200ns (colored) and cryo-EM structure of E1(apo) state (grey). (**B**) Structural comparison of ATP13A2 between snapshot of MD simulation of E2 state at 200ns (colored) and cryo-EM structure of E2 state (gray). Structures are shown in the backbone-trace representation.

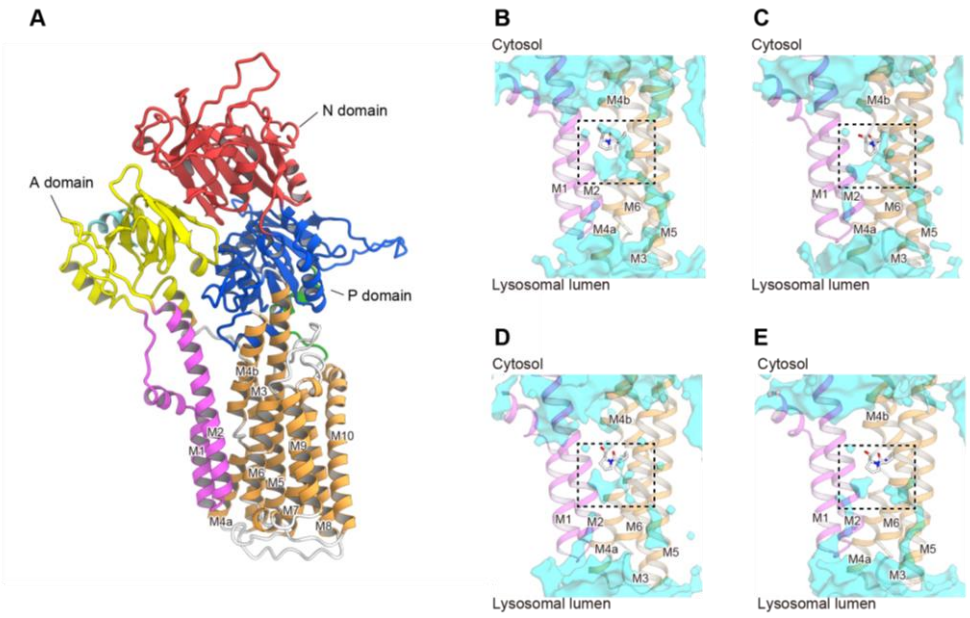

Figure 4-4 | Stably formed occlusion pocket in MD simulation of E1(apo) state.

(**A**) Ribbon model representation of the initial model of ATP13A2 for MD simulation under E1(apo) condition. (**B-E**) Water accessible cavity of ATP13A2 in the MD simulation under E1(apo) condition. Each picture represents 50 ns (**B**), 100 ns (**C**), 150 ns (**D**), and 200 ns (**E**), in 200 ns MD simulations.

4.3 Perspectives

In this thesis, I have elucidated the ATP modulated Mg^{2+} homeostasis mechanism by MgtE and the SPM uptake mechanism by ATP13A2 using ATP as a driving force. In particular, several groups reported functional and structural studies of ATP13A2 around the same time as our original paper was published, which increased our knowledge of the recognition and transport mechanisms of SPM by ATP13A2. However, several questions are still elusive.

4.3.1 ATP modulated Mg^{2+} homeostasis.

At the time of publication of our original paper, the structures of full-length MgtE in Mg^{2+} bound closed had been reported, while the structure of MgtE in the Mg^{2+} free open state had not been reported[31,43,51]. Therefore, it was still unclear how MgtE permeate Mg^{2+} under low Mg^{2+} conditions. Recently, Jin et al. reported the cryo-EM structure of MgtE-fab complex in the absence of Mg^{2+} (ref [172]). In the reported structure, only rigid transmembrane domain and fab was observed. The transmembrane domain was open to the cytoplasmic side while it was closed to the periplasmic side, indicating a partially open inactive structure. Comparison of the cryo-EM structure of MgtE in Mg^{2+} free partially open state with crystal structure of MgtE in Mg^{2+} bound closed state suggested that the kink of glycine in the TM domain is important for Mg^{2+} permeation. However, to understand the precise mechanism of Mg^{2+} permeation by MgtE, further structural studies are needed to determine the structure of MgtE in the fully open active state.

In addition to MgtE, there are many other Mg^{2+} transport proteins involved in Mg^{2+} homeostasis in the cell. Among them, the CorC/CNNM family has a CBS domain similar to that of MgtE and has been reported to be involved in ATP modulated Mg^{2+} transport[118,132]. Recently, Huang et al. reported the crystal structures of bacterial CorC transmembrane domain dimer and CorC CBS domain[173]. Huang et al. revealed Mg^{2+} recognition mechanism of CorC/CNNM family based on the crystal structure of the transmembrane domain of CorC in the presence of Mg^{2+} (ref [173]). Moreover, Huang et al. reported the binding mode of ATP to the CBS domain of CorC/CNNM family based on the crystal structure of the CorC CBS domain in complex with ATP[173]. However, how ATP modulates the transport activity of CorC is still elusive due to lack of structural information of full length CorC in the presence and absence of ATP. Further structural and functional analysis of CorC/CNNM family is still needed.

4.3.2 ATP dependent SPM uptake by ATP13A2.

Our study and studies from other groups revealed SPM recognition mechanism and structural dynamics of ATP13A2 in SPM transport cycle. However, two questions still remain.

First, the precise lipid activation mechanism is not understood as the exact binding positions of PIP_2 and PA could not be determined. In the cryo-EM map of ATP13A2, many lipid-derived

densities were observed. Since it is difficult to distinguish PIP_2 and PA from other endogenous lipids in the density map, the exact binding position of PIP_2 and PA could not be determined.
Second, How ATP13A2 release SPM is still unknown due to lack of structural information of E2 state just after release of phosphate and SPM. Although five groups including our original paper have reported the cryo-EM structures of human ATP13A2 and yeast ATP13A2 homolog, none of them has succeeded in capturing the structure during SPM release. Most of them have stated that the SPM release mechanism is not yet understood, which is one of the major remaining issues. As I described in discussion section in Chapter 3, two types of SPM release models can be proposed. It is noteworthy that Tillinghast et al. discussed channel-pump SPM release mechanism through extensive comparisons with other cation channels[171]. In our original paper, I performed 200ns MD simulation of ATP13A2 under E2Pi(SPM) condition to obtain structural insight into the SPM release after dephosphorylation (Figure 3-21). In the MD simulation, no significant structural changes involving SPM transport were observed. However, a water pathway was observed from the SPM binding site to the cytosolic side, suggesting that SPM is transported along the water pathway (Figure 3-21). Since the mutations of hydrophilic amino acids in the water pathway reduce the SPM-dependent ATPase activity, SPM is expected to be transported along the water pathway (Figure 3-14D). In order to obtain more detailed knowledge of SPM transport, it is necessary to determine the structure of the E2 state just after SPM transport and perform long time MD simulation of E2Pi(SPM) to E2 state to obtain structural dynamics of SPM release process.

4.3.3 Other remarkable studies about structural dynamics of P-type ATPases.

MD simulations of P-type ATPase have long been studied with a focus on the Ca^{2+} pump SERCA[174–177]. Since the entire transport process of P-type ATPase is on the order of milliseconds, it is difficult to study the entire transport cycle using standard MD simulations. Among the transport processes, the transition between the E1 and E2 states is a rate-limiting process with large structural changes, which is difficult to calculate in MD simulations. Recently, Kobayashi et al. successfully sampled the structural dynamics of SERCA in E1P to E2P transition, using MD simulations with the mean-force string method and umbrella sampling[178]. Moreover, Kobayashi et al. successfully revealed the free energy profile in the E1P to E2P transition. These developments in MD simulations may provide structural insights into the working principle of the pump common to P-type ATPases in the future. By calculating the entire transport cycle and the associated free energy profile through MD simulations, we may be able to understand the process by which the free energy of ATP hydrolysis is used for structural changes and substrate transport, and the process of diffusion as heat through lipids and water molecules[179]. In this way, we may be able to understand the working principle of the pump.

Acknowledgements

I would like to thank Dr. Osamu Nureki for his supervision of my PhD study. I would like to express my deepest gratitude for his willingness to welcome me to the Nureki's laboratory. Without his assistance and encouragement, my PhD study could not have been accomplished. He also provided me the excellent research environment and the opportunity to challenge difficult research on my own. I would also like to thank Dr. Ryuichiro Ishitani, Dr. Tomohiro Nishizawa, and Dr. Motoyuki Hattori for teaching me all the professional skills, knowledge, and spirit to conduct and enjoy research in the field of structural biology. Especially, Dr. Ryuichiro Ishitani provided me many insightful discussions, which inspired me developing my perspective of structural biology and biophysics. The basis of my writing and presentation skills was mostly established by Dr. Tomohiro Nishizawa, Dr. Motoyuki Hattori, and Dr. Ryuichiro Ishitani.

I am greatly indebted to many collaborators. All X-ray diffraction experiments were conducted with the help of excellent beamline scientists at SPring-8. All cryo-EM data collections were made possible with help of scientists at the cryo-EM facility at University of Tokto. Especially, I thank Dr. Rado Danev and Masahide Kikkawa for setting up the cryo-EM infrastructure. Dr. Keitaro Yamashita provided expert support and taught me the professional skills of refinement and model building. His support and insightful discussions inspired me developing my perspective of structural biology and biophysics. I would also like to thank Dr. Yan Zhiqiang and Dr. Hisashi Kawasaki for electrophysiological analysis, Dr. Koichi Ito for *in vivo* assays of MgtE by using bacterial genetics, and Dr. Naoshi Dohmae for mass spectrometry analyses.

Special thanks go to all present and past members of Nureki's laboratory. Dr. Hironori Takeda, my former mentor during the bachelor provided me the basis of my experimental skills and assisting the initial stage of this project. Dr. Hideaki Kato and Dr. Kazuki Kato provided me many insightful discussions in development of this project. Senior lab members Dr. Kaoru Kumazaki, Dr. Tsukasa Kusakizako, Dr. Reiya Taniguchi, Dr. Go Kasuya and Dr. Mizuki Takemoto helped me greatly during project design and experiments. I also thank Mr. Masahiro Hiraizumi, Mr. Hiroto Shimada, Mr. Kazuhiro Kobayashi, Ms. Chisae Nagiri, Mr. Hiroyuki Okamoto, Ms. Haon Futamata, Mr. Satoru Takeda, and Mr. Michihiro Nishimura for supporting my PhD life. I deeply thank Dr. Hisato Hirano, Dr. Hirotake Miyauchi, Dr. Seiichi Hirano, Mr. Tomoyuki Takatsuji as the four closest labmates from my undergraduate course. I would like thank Rieko Yamazaki and Noriko Toyama for administrative support, and Arisa Kurabayashi, Sae Okazaki, Kazuyo Ogomori, Chieko Harada for technical assistance.

I would like to express my deep gratitude for the financial support from Japan Student Services Organization and Japan Society for the Promotion of Science.

Lastly, I would like to express my sincere thanks to my parents for their warm support and encouragement of my career.

References

1. Betts, J. G. *et al. Anatomy and physiology*. (2017).
2. Sigel, A. *et al. Interrelations between Essential Metal Ions and Human Diseases.* **13**, (2013).
3. Romani, A. M. P. Cellular magnesium homeostasis. *Arch. Biochem. Biophys.* **512**, 1–23 (2011).
4. Nelson, N. Metal ion transporters and homeostasis. *EMBO J.* **18**, 4361–4371 (1999).
5. Gadsby, D. C. Ion channels versus ion pumps: the principal difference, in principle. *Nat. Rev. Mol. Cell Biol.* **10**, 344 (2009).
6. Ashcroft, F., Gadsby, D. & Miller, C. Introduction. The blurred boundary between channels and transporters: We dedicate this volume to the memory of Peter Läuger, a pioneer of the link between channels and pumps. *Philos. Trans. R. Soc. B Biol. Sci.* **364**, 145 (2009).
7. Drew, D. & Boudker, O. Shared Molecular Mechanisms of Membrane Transporters. *Annu. Rev. Biochem.* **85**, 543–572 (2016).
8. Wilson, J. E. & Chin, A. Chelation of divalent cations by ATP, studied by titration calorimetry. *Anal. Biochem.* **193**, 16–19 (1991).
9. Garfinkel, L., Altschuld, R. A. & Garfinkel, D. Magnesium in cardiac energy metabolism. *J. Mol. Cell. Cardiol.* **18**, 1003–1013 (1986).
10. Storer, A. C. & Cornish Bowden, A. Concentration of $MgATP^{2-}$ and other ions in solution. Calculation of the true concentrations of species present in mixtures of associating ions. *Biochem. J.* **159**, 1 (1976).
11. Chance, B., Lees, H. & Postgate, J. R. The Meaning of "Reversed Electron Flow" and "High Energy Electron" in Biochemistry. *Nature.* **238**, 330–331 (1972).
12. Alberty, R. A. *Thermodynamics of biochemical reactions.* 397 (2003).
13. Gribble, F. M. *et al.* A Novel Method for Measurement of Submembrane ATP Concentration. *J. Biol. Chem.* **275**, 30046–30049 (2000).
14. Larcombe-McDouall, J., Buttell, N., Harrison, N. & Wray, S. In vivo pH and metabolite changes during a single contraction in rat uterine smooth muscle. *J. Physiol.* **518**, 783–790 (1999).
15. Dragon, S., Hille, R., Götz, R. & Baumann, R. Adenosine 3′:5′-Cyclic Monophosphate (cAMP)-Inducible Pyrimidine 5′-Nucleotidase and Pyrimidine Nucleotide Metabolism of Chick Embryonic Erythrocytes. *Blood* **91**, 3052–3058 (1998).
16. Kawashima, S. Inhibition of rat liver transglutaminase by nucleotides. *Exp.* **47**, 709–712 (1991).
17. Yoshida, T., Kakizuka, A. & Imamura, H. BTeam, a Novel BRET-based Biosensor for

the Accurate Quantification of ATP Concentration within Living Cells. *Sci. Reports* **6**, 1–9 (2016).

18. Imamura, H. *et al.* Visualization of ATP levels inside single living cells with fluorescence resonance energy transfer-based genetically encoded indicators. *Proc. Natl. Acad. Sci.* **106**, 15651–15656 (2009).
19. Bennett, B. D. *et al.* Absolute metabolite concentrations and implied enzyme active site occupancy in Escherichia coli. *Nat. Chem. Biol.* **5**, 593–599 (2009).
20. Nicholls, D. G. & Ferguson, S. J. (Stuart J. Bioenergetics 3. 297 (2002).
21. Deckers-Hebestreit, G. & Altendorf, K. THE F0F1-TYPE ATP SYNTHASES OF BACTERIA: Structure and Function of the F0 Complex. *Annu. Rev. Microbiol.* **50**, 791–824 (2003).
22. Von Ballmoos, C., Wiedenmann, A. & Dimroth, P. Essentials for ATP Synthesis by F1F0 ATP Synthases. *Annu. Rev. Biochem.* **78**, 649–672 (2009).
23. Grüber, G., Manimekalai, M. S. S., Mayer, F. & Müller, V. ATP synthases from archaea: The beauty of a molecular motor. *Biochim. Biophys. Acta - Bioenerg.* **1837**, 940–952 (2014).
24. Zhou, L. & Sazanov, L. A. Structure and conformational plasticity of the intact Thermus thermophilus V/A-type ATPase. *Science* **365**, (2019).
25. Hochstein, L. I. & Stan-Lotter, H. Purification and properties of an ATPase from Sulfolobus solfataricus. *Arch. Biochem. Biophys.* **295**, 153–160 (1992).
26. Bateman, A. The structure of a domain common to archaebacteria and the homocystinuria disease protein. *Trends Biochem. Sci.* **22**, 12–13 (1997).
27. Kemp, B. E. Bateman domains and adenosine derivatives form a binding contract. *J. Clin. Invest.* **113**, 182 (2004).
28. Rudolph, M. J. *et al.* Structure of the Bateman2 Domain of Yeast Snf4: Dimeric Association and Relevance for AMP Binding. *Structure* **15**, 65–74 (2007).
29. Zhang, R. G. *et al.* Characteristics and Crystal Structure of Bacterial Inosine-5‘-monophosphate Dehydrogenase. *Biochemistry* **38**, 4691–4700 (1999).
30. Meyer, S., Savaresi, S., Forster, I. C. & Dutzler, R. Nucleotide recognition by the cytoplasmic domain of the human chloride transporter ClC-5. *Nat. Struct. Mol. Biol.* **14**, 60–7 (2007).
31. Hattori, M., Tanaka, Y., Fukai, S., Ishitani, R. & Nureki, O. Crystal structure of the MgtE Mg^{2+} transporter. *Nature* **448**, 1072–5 (2007).
32. Ishitani, R. *et al.* Mg^{2+}-sensing mechanism of Mg^{2+} transporter MgtE probed by molecular dynamics study. *Proc. Natl. Acad. Sci. U. S. A.* **105**, 15393–8 (2008).
33. Günther, W., Lüchow, A., Cluzeaud, F., Vandewalle, A. & Jentsch, T. J. ClC-5, the

chloride channel mutated in Dent's disease, colocalizes with the proton pump in endocytotically active kidney cells. *Proc. Natl. Acad. Sci. U. S. A.* **95**, 8075 (1998).

34. Devuyst, O., Christie, P. T., Courtoy, P. J., Beauwens, R. & Thakker, R. V. Intra-Renal and Subcellular Distribution of the Human Chloride Channel, CLC-5, Reveals a Pathophysiological Basis for Dent's Disease. *Hum. Mol. Genet.* **8**, 247–257 (1999).
35. Grieschat, M., Guzman, R. E., Langschwager, K., Fahlke, C. & Alekov, A. K. Metabolic energy sensing by mammalian CLC anion/proton exchangers. *EMBO Rep.* **21**, e47872 (2020).
36. Schrecker, M., Korobenko, J. & Hite, R. K. Cryo-em structure of the lysosomal chloride-proton exchanger clc-7 in complex with ostm1. *Elife* **9**, 1–25 (2020).
37. Hartwig, A. Role of magnesium in genomic stability. *Mutat. Res. Mol. Mech. Mutagen.* **475**, 113–121 (2001).
38. Cowan, J. A. Structural and catalytic chemistry of magnesium-dependent enzymes. *Biometals* **15**, 225–35 (2002).
39. Alexander, R. T., Hoenderop, J. G. & Bindels, R. J. Molecular determinants of magnesium homeostasis: insights from human disease. *J. Am. Soc. Nephrol.* **19**, 1451–8 (2008).
40. Groisman, E. A. *et al.* Bacterial Mg^{2+} homeostasis, transport, and virulence. *Annu. Rev. Genet.* **47**, 625–46 (2013).
41. Moomaw, A. S. & Maguire, M. E. The unique nature of mg^{2+} channels. *Physiology (Bethesda).* **23**, 275–85 (2008).
42. Dann, C. E. *et al.* Structure and mechanism of a metal-sensing regulatory RNA. *Cell* **130**, 878–92 (2007).
43. Hattori, M. *et al.* Mg^{2+}-dependent gating of bacterial MgtE channel underlies Mg^{2+} homeostasis. *EMBO J.* **28**, 3602–12 (2009).
44. Sahni, J., Nelson, B. & Scharenberg, A. M. SLC41A2 encodes a plasma-membrane Mg^{2+} transporter. *Biochem. J.* **401**, 505–13 (2007).
45. Sahni, J. & Scharenberg, A. M. The SLC41 family of MgtE-like magnesium transporters. *Mol. Aspects Med.* **34**, 620–8 (2013).
46. Goytain, A. & Quamme, G. A. Functional characterization of human SLC41A1, a Mg^{2+} transporter with similarity to prokaryotic MgtE Mg^{2+} transporters. *Physiol. Genomics* **21**, 337–42 (2005).
47. Mandt, T., Song, Y., Scharenberg, A. M. & Sahni, J. SLC41A1 Mg^{2+} transport is regulated via Mg^{2+}-dependent endosomal recycling through its N-terminal cytoplasmic domain. *Biochem. J.* **439**, 129–39 (2011).
48. Kolisek, M. *et al.* Substitution p.A350V in Na^{+}/Mg^{2+} exchanger SLC41A1, potentially

associated with Parkinson's disease, is a gain-of-function mutation. *PLoS One* **8**, e71096 (2013).

49. Chan, K. H. K. *et al.* Genetic variations in magnesium-related ion channels may affect diabetes risk among African American and Hispanic American women. *J. Nutr.* **145**, 418–24 (2015).
50. Hurd, T. W. *et al.* Mutation of the Mg^{2+} transporter SLC41A1 results in a nephronophthisis-like phenotype. *J. Am. Soc. Nephrol.* **24**, 967–77 (2013).
51. Takeda, H. *et al.* Structural basis for ion selectivity revealed by high-resolution crystal structure of Mg^{2+} channel MgtE. *Nat. Commun.* **5**, 5374 (2014).
52. Wolf, F. I. & Cittadini, A. Chemistry and biochemistry of magnesium. *Mol. Aspects Med.* **24**, 3–9.
53. Rees, D. C., Johnson, E. & Lewinson, O. ABC transporters: the power to change. *Nat. Rev. Mol. Cell Biol.* **10**, 218–227 (2009).
54. Vasanthakumar, T. & Rubinstein, J. L. Structure and Roles of V-type ATPases. *Trends Biochem. Sci.* **45**, 295–307 (2020).
55. Dyla, M. *et al.* Structural dynamics of P-type ATPase ion pumps.*Biochem. Soc. Trans.* **47**, 1247–1257 (2019).
56. Kühlbrandt, W. Biology, structure and mechanism of P-type ATPases. *Nat. Rev. Mol. Cell Biol.* **5**, 282–295 (2004).
57. Palmgren, M. G. & Nissen, P. P-Type ATPases. *Annu. Rev. Biophys.* **40**, 243–266 (2011).
58. Skou, J. C. The influence of some cations on an adenosine triphosphatase from peripheral nerves. *Biochim. Biophys. Acta* **23**, 394–401 (1957).
59. Dyla, M., Kjærgaard, M., Poulsen, H. & Nissen, P. Structure and Mechanism of P-Type ATPase Ion Pumps. *Annu. Rev. Biochem.* **89**, 583–603 (2020).
60. Ekberg, K., Palmgren, M. G., Veierskov, B. & Buch-Pedersen, M. J. A Novel Mechanism of P-type ATPase Autoinhibition Involving Both Termini of the Protein. *J. Biol. Chem.* **285**, 7344 (2010).
61. Andersen, J. P. *et al.* P4-ATPases as Phospholipid Flippases—Structure, Function, and Enigmas. *Front. Physiol.* **7**, 275 (2016).
62. Holemans, T. *et al.* A lipid switch unlocks Parkinson's disease-associated ATP13A2. *Proc. Natl. Acad. Sci. U. S. A.* **112**, 9040–9045 (2015).
63. Pedersen, P. L. & Carafoli, E. Ion motive ATPases. I. Ubiquity, properties, and significance to cell function. *Trends Biochem. Sci.* **12**, 146–150 (1987).
64. Post, R. L., Kume, S., Tobin, T., Orcutt, B. & Sen, A. K. Flexibility of an active center in sodium-plus-potassium adenosine triphosphatase. *J. Gen. Physiol.* **54**, 306–326

(1969).

65. Albers, R. W. Biochemical Aspects of Active Transport. *Annu. Rev. Biochem.* 727–756 (1967).
66. Toyoshima, C., Nakasako, M., Nomura, H. & Ogawa, H. Crystal structure of the calcium pump of sarcoplasmic reticulum at 2.6 Å resolution. *Nature* **405**, 647–655 (2000).
67. Sørensen, T. L. M., Møller, J. V. & Nissen, P. Phosphoryl transfer and calcium ion occlusion in the calcium pump. *Science.* **304**, 1672–1675 (2004).
68. Toyoshima, C. & Inesi, G. Structural basis of ion pumping by Ca^{2+}-ATPase of the sarcoplasmic reticulum. *Annual Review of Biochemistry* **73**, 269–292 (2004).
69. Olesen, C. *et al.* The structural basis of calcium transport by the calcium pump. *Nature* **450**, 1036–1042 (2007).
70. Toyoshima, C., Norimatsu, Y., Iwasawa, S., Tsuda, T. & Ogawa, H. How processing of aspartylphosphate is coupled to lumenal gating of the ion pathway in the calcium pump. *Proc. Natl. Acad. Sci. U. S. A.* **104**, 19831–19836 (2007).
71. Bublitz, M., Morth, P. J. & Nissen, P. P-type ATPases at a glance. *J. Cell Sci.* **124**, 2515–2519 (2011).
72. Axelsen, K. B. & Palmgren, M. G. Evolution of substrate specificities in the P-type ATPase superfamily. *J. Mol. Evol.* **46**, 84–101 (1998).
73. Gourdon, P. *et al.* Crystal structure of a copper-transporting PIB-type ATPase. *Nature* **475**, 59–65 (2011).
74. Li, P., Wang, K., Salustros, N., Grønberg, C. & Gourdon, P. Structure and transport mechanism of P5B-ATPases. *Nat. Commun.* **12**, 1–8 (2021).
75. Olesen, C. *et al.* The structural basis of calcium transport by the calcium pump. *Nature* **450**, 1036–1042 (2007).
76. Olesen, C., Sørensen, T. L. M., Nielsen, R. C., Møller, J. V. & Nissen, P. Dephosphorylation of the calcium pump coupled to counterion occlusion. *Science* **306**, 2251–2255 (2004).
77. Toyoshima, C., Nomura, H. & Tsuda, T. Lumenal gating mechanism revealed in calcium pump crystal structures with phosphate analogues. *Nature* **432**, 361–368 (2004).
78. Toyoshima, C. How Ca^{2+}-ATPase pumps ions across the sarcoplasmic reticulum membrane. *Biochimica et Biophysica Acta - Molecular Cell Research* **1793** 941–946 (2009).
79. Kanai, R., Ogawa, H., Vilsen, B., Cornelius, F. & Toyoshima, C. Crystal structure of a Na^+-bound Na^+,K^+-ATPase preceding the E1P state. *Nature* **502**, 201–206 (2013).
80. Shinoda, T., Ogawa, H., Cornelius, F. & Toyoshima, C. Crystal structure of the sodium-potassium pump at 2.4 resolution. *Nature* **459**, 446–450 (2009).

81. Nyblom, M. *et al.* Crystal structure of Na^+, K^+-ATPase in the Na^+-bound state. *Science* **342**, 123–127 (2013).
82. Abe, K., Irie, K., Nakanishi, H., Suzuki, H. & Fujiyoshi, Y. Crystal structures of the gastric proton pump. *Nature* **556**, 214–229 (2018).
83. Pedersen, B. P., Buch-Pedersen, M. J., Preben Morth, J., Palmgren, M. G. & Nissen, P. Crystal structure of the plasma membrane proton pump. *Nature* **450**, 1111–1114 (2007).
84. Heit, S. *et al.* Structure of the hexameric fungal plasma membrane proton pump in its autoinhibited state. *Sci. Adv.* **7**, 5255 (2021).
85. Zhao, P. *et al.* Structure and activation mechanism of the hexameric plasma membrane H^+-ATPase. *Nat. Commun. 2021 121* **12**, 1–11 (2021).
86. Hiraizumi, M., Yamashita, K., Nishizawa, T. & Nureki, O. Cryo-EM structures capture the transport cycle of the P4-ATPase flippase. *Science* **365**, 1149–1155 (2019).
87. Timcenko, M. *et al.* Structure and autoregulation of a P4-ATPase lipid flippase. *Nature* **571**, 366–370 (2019).
88. Bai, L. *et al.* Transport mechanism of P4 ATPase phosphatidylcholine flippases. *Elife* **9**, 1–20 (2020).
89. Nakanishi, H. *et al.* Transport Cycle of Plasma Membrane Flippase ATP11C by Cryo-EM. *Cell Rep.* **32**, (2020).
90. Nakanishi, H. *et al.* Crystal structure of a human plasma membrane phospholipid flippase. *J. Biol. Chem.* **295**, 10180–10194 (2020).
91. McKenna, M. J. *et al.* The endoplasmic reticulum P5A-ATPase is a transmembrane helix dislocase. *Science* **369**, (2020).
92. van Veen, S. *et al.* ATP13A2 deficiency disrupts lysosomal polyamine export. *Nature* **578**, 419–424 (2020).
93. Tabor, C. W. & Tabor, H. Polyamines. *Annu. Rev. Biochem.* **53**, 749–790 (1984).
94. Marton, L. J. & Pegg, A. E. Polyamines as Targets for Therapeutic Intervention. *Annu. Rev. Pharmacol. Toxicol.* **35**, 55–91 (1995).
95. Kanemura, A. *et al.* Opposite effect of polyamines on In vitro gene expression: Enhancement at low concentrations but inhibition at high concentrations. *PLoS One* **13**, e0193595 (2018).
96. Feuerstein, B. G., Pattabiraman, N. & Marton, L. J. Molecular mechanics of the interactions of spermine with DNA: DNA bending as a result of ligand binding. *Nucleic Acids Res.* **18**, 1271–1282 (1990).
97. Snyder, R. D. Polyamine depletion is associated with altered chromatin structure in HeLa cells. *Biochem. J.* **260**, 697–704 (1989).
98. Brüne, B., Hartzell, P., Nicotera, P. & Orrenius, S. Spermine prevents endonuclease

activation and apoptosis in thymocytes. *Exp. Cell Res.* **195**, 323–329 (1991).

99. Khan, A. U., Mei, Y. H. & Wilson, T. A proposed function for spermine and spermidine: Protection of replicating DNA against damage by singlet oxygen. *Proc. Natl. Acad. Sci. U. S. A.* **89**, 11426–11427 (1992).
100. Khan, A. U., Di Mascio, P., Medeiros, M. H. G. & Wilson, T. Spermine and spermidine protection of plasmid DNA against single-strand breaks induced by singlet oxygen. *Proc. Natl. Acad. Sci. U. S. A.* **89**, 11428–11430 (1992).
101. Ha, H. C. *et al.* The natural polyamine spermine functions directly as a free radical scavenger. *Proc. Natl. Acad. Sci. U. S. A.* **95**, 11140–11145 (1998).
102. Li, C. *et al.* Spermine synthase deficiency causes lysosomal dysfunction and oxidative stress in models of Snyder-Robinson syndrome. *Nat. Commun.* **8**, (2017).
103. LØVaas, E. Antioxidative and Metal-Chelating Effects of Polyamines. *Adv. Pharmacol.* **38**, 119–149 (1996).
104. Minois, N., Carmona-Gutierrez, D. & Madeo, F. Polyamines in aging and disease. *Aging (Albany. NY).* **3**, 716–732 (2011).
105. Ramirez, A. *et al.* Hereditary parkinsonism with dementia is caused by mutations in ATP13A2, encoding a lysosomal type 5 P-type ATPase. *Nat. Genet.* **38**, 1184–1191 (2006).
106. Dehay, B. *et al.* Loss of P-type ATPase ATP13A2/PARK9 function induces general lysosomal deficiency and leads to Parkinson disease neurodegeneration. *Proc. Natl. Acad. Sci. U. S. A.* **109**, 9611–9616 (2012).
107. Tanaka, Y., Hattori, M., Fukai, S., Ishitania, R. & Nureki, O. Crystallization and preliminary X-ray diffraction analysis of the cytosolic domain of the Mg^{2+} transporter MgtE. *Acta Crystallogr. Sect. F. Struct. Biol. Cryst. Commun.* **63**, 678–81 (2007).
108. Schneider, C. A., Rasband, W. S. & Eliceiri, K. W. NIH Image to ImageJ: 25 years of image analysis. *Nat. Methods* **9**, 671–675 (2012).
109. Battle, A. R., Petrov, E., Pal, P. & Martinac, B. Rapid and improved reconstitution of bacterial mechanosensitive ion channel proteins MscS and MscL into liposomes using a modified sucrose method. *FEBS Lett.* **583**, 407–12 (2009).
110. Kabsch, W. Xds. *Acta Crystallogr. Sect. D Biol. Crystallogr.* **66**, 125–132 (2010).
111. Collaborative Computational Project, Number 4. The CCP4 suite: programs for protein crystallography. *Acta Crystallogr. D. Biol. Crystallogr.* **50**, 760–3 (1994).
112. Emsley, P. & Cowtan, K. Coot: Model-building tools for molecular graphics. *Acta Crystallogr. Sect. D Biol. Crystallogr.* **60**, 2126–2132 (2004).
113. Adams, P. D. *et al.* PHENIX: Building new software for automated crystallographic structure determination. *Acta Crystallogr. Sect. D Biol. Crystallogr.* **58**, 1948–1954

(2002).

114. Baykov, A. A., Evtushenko, O. A. & Avaeva, S. M. A malachite green procedure for orthophosphate determination and its use in alkaline phosphatase-based enzyme immunoassay. *Anal Biochem* **171**, 266–270 (1988).
115. Scott, J. W. *et al.* CBS domains form energy-sensing modules whose binding of adenosine ligands is disrupted by disease mutations. *J. Clin. Invest.* **113**, 274–84 (2004).
116. Beis, I. & Newsholme, E. A. The contents of adenine nucleotides, phosphagens and some glycolytic intermediates in resting muscles from vertebrates and invertebrates. *Biochem. J.* **152**, 23–32 (1975).
117. Pontes, M. H., Lee, E.-J., Choi, J. & Groisman, E. A. Salmonella promotes virulence by repressing cellulose production. *Proc. Natl. Acad. Sci. U. S. A.* **112**, 5183–8 (2015).
118. Funato, Y. *et al.* Membrane protein CNNM4-dependent Mg^{2+} efflux suppresses tumor progression. *J. Clin. Invest.* **124**, 5398–410 (2014).
119. Ko, Y. H., Hong, S. & Pedersen, P. L. Chemical mechanism of ATP synthase. Magnesium plays a pivotal role in formation of the transition state where ATP is synthesized from ADP and inorganic phosphate. *J. Biol. Chem.* **274**, 28853–6 (1999).
120. Shur, S. A. & Vul'fson, P. L. Effect of ATP, ADP and magnesium ions on the activity of phosphorylase kinase from rabbit skeletal muscles. *Nauchnye Dokl. Vyss. shkoly. Biol. Nauk.* 31–5 (1985).
121. Diamant, S., Azem, A., Weiss, C. & Goloubinoff, P. Effect of free and ATP-bound magnesium and manganese ions on the ATPase activity of chaperonin GroEL14. *Biochemistry* **34**, 273–7 (1995).
122. Ignoul, S. & Eggermont, J. CBS domains: structure, function, and pathology in human proteins. *Am. J. Physiol. Cell Physiol.* **289**, C1369-78 (2005).
123. Biemans-Oldehinkel, E., Mahmood, N. A. & Poolman, B. A sensor for intracellular ionic strength. *Proc Natl Acad Sci U S A* **103**, 10624–10629 (2006).
124. Accardi, A. Structure and gating of CLC channels and exchangers. *J Physiol* **593**, 4129–4138 (2015).
125. Park, E., Campbell, E. B. & MacKinnon, R. Structure of a CLC chloride ion channel by cryo-electron microscopy. *Nature* **541**, 500–505 (2017).
126. Feng, L., Campbell, E. B., Hsiung, Y. & MacKinnon, R. Structure of a eukaryotic CLC transporter defines an intermediate state in the transport cycle. *Science* **330**, 635–641 (2010).
127. Maruyama, T. *et al.* Functional roles of Mg^{2+} binding sites in ion-dependent gating of a Mg^{2+} channel, MgtE, revealed by solution NMR. *Elife* **7**, (2018).
128. De Angeli, A. *et al.* ATP binding to the C terminus of the Arabidopsis thaliana

nitrate/proton antiporter, AtCLCa, regulates nitrate transport into plant vacuoles. *J Biol Chem* **284**, 26526–26532 (2009).

129. Lunin, V. V. *et al.* Crystal structure of the CorA Mg^{2+} transporter. *Nature* **440**, 833–837 (2006).
130. Matthies, D. *et al.* Cryo-EM Structures of the Magnesium Channel CorA Reveal Symmetry Break upon Gating. *Cell* **164**, 747–756 (2016).
131. Payandeh, J. & Pai, E. F. A structural basis for Mg^{2+} homeostasis and the CorA translocation cycle. *EMBO J.* **25**, 3762–3773 (2006).
132. Hirata, Y., Funato, Y., Takano, Y. & Miki, H. Mg^{2+}-dependent interactions of ATP with the cystathionine-beta-synthase (CBS) domains of a magnesium transporter. *J Biol Chem* **289**, 14731–14739 (2014).
133. van Veen, S. *et al.* Cellular function and pathological role of ATP13A2 and related P-type transport ATPases in Parkinson's disease and other neurological disorders. *Frontiers in Molecular Neuroscience* vol. 7 (2014).
134. Mastronarde, D. N. Automated electron microscope tomography using robust prediction of specimen movements. *J. Struct. Biol.* **152**, 36–51 (2005).
135. Zivanov, J. *et al.* New tools for automated high-resolution cryo-EM structure determination in RELION-3. *Elife* **7**, (2018).
136. Rohou, A. & Grigorieff, N. CTFFIND4: Fast and accurate defocus estimation from electron micrographs. *J. Struct. Biol.* **192**, 216–221 (2015).
137. Zivanov, J., Nakane, T. & Scheres, S. H. W. A Bayesian approach to beam-induced motion correction in cryo-EM single-particle analysis. *IUCrJ* **6**, 5–17 (2019).
138. Rosenthal, P. B. & Henderson, R. Optimal determination of particle orientation, absolute hand, and contrast loss in single-particle electron cryomicroscopy. *J. Mol. Biol.* **333**, 721–745 (2003).
139. Emsley, P., Lohkamp, B., Scott, W. G. & Cowtan, K. Features and development of Coot. *Acta Crystallogr. Sect. D Biol. Crystallogr.* **66**, 486–501 (2010).
140. Shinoda, T., Ogawa, H., Cornelius, F. & Toyoshima, C. Crystal structure of the sodium-potassium pump at 2.4 resolution. *Nature* **459**, 446–450 (2009).
141. Sanchez-Garcia, R. *et al.* DeepEMhancer: A deep learning solution for cryo-EM volume post-processing. *bioRxiv* (2020).
142. Xu, J., Mcpartlon, M. & Li, J. Improved protein structure prediction by deep learning irrespective of co-evolution information. *Nat. Mach. Intell.* **3**, 601–609 (2021).
143. Afonine, P. V. *et al.* Real-space refinement in PHENIX for cryo-EM and crystallography. *Acta Crystallogr. Sect. D Struct. Biol.* **74**, 531–544 (2018).
144. Nicholls, R. A., Tykac, M., Kovalevskiy, O. & Murshudov, G. N. Current approaches for

the fitting and refinement of atomic models into cryo-em maps using CCP-EM. *Acta Crystallogr. Sect. D Struct. Biol.* **74**, 492–505 (2018).

145. Yamashita, K., Palmer, C. M., Burnley, T. & Murshudov, G. N. Cryo-EM single particle structure refinement and map calculation using Servalcat. *bioRxiv* (2021).
146. Nicholls, R. A., Long, F. & Murshudov, G. N. Low-resolution refinement tools in REFMAC5. *Acta Crystallogr. Sect. D Biol. Crystallogr.* **68**, 404–417 (2012).
147. Söding, J., Biegert, A. & Lupas, A. N. The HHpred interactive server for protein homology detection and structure prediction. *Nucleic Acids Res.* **33**, (2005).
148. Goddard, T. D. *et al.* UCSF ChimeraX: Meeting modern challenges in visualization and analysis. *Protein Sci.* **27**, 14–25 (2018).
149. Daiho, T. *et al.* Mutations of Either or Both Cys876 and Cys888 Residues of Sarcoplasmic Reticulum Ca^{2+}-ATPase Result in a Complete Loss of Ca^{2+} Transport Activity without a Loss of Ca^{2+}-dependent ATPase Activity: Role of the Cys876-Cys 888 disulfide bond. *J. Biol. Chem.* **276**, 32771–32778 (2001).
150. Šali, A. & Blundell, T. L. Comparative protein modelling by satisfaction of spatial restraints. *J. Mol. Biol.* **234**, 779–815 (1993).
151. Sim, S. I., von Bülow, S., Hummer, G. & Park, E. Structural basis of polyamine transport by human ATP13A2 (PARK9). *Mol. Cell* **81**, 4635-4649.e8 (2021).
152. Humphrey, W., Dalke, A. & Schulten, K. VMD: Visual molecular dynamics. *J. Mol. Graph.* **14**, 33–38 (1996).
153. Stansfeld, P. J. *et al.* MemProtMD: Automated Insertion of Membrane Protein Structures into Explicit Lipid Membranes. *Structure* **23**, 1350–1361 (2015).
154. Best, R. B. *et al.* Optimization of the additive CHARMM all-atom protein force field targeting improved sampling of the backbone φ, ψ and side-chain χ1 and χ2 Dihedral Angles. *J. Chem. Theory Comput.* **8**, 3257–3273 (2012).
155. Klauda, J. B. *et al.* Update of the CHARMM All-Atom Additive Force Field for Lipids: Validation on Six Lipid Types. *J. Phys. Chem. B* **114**, 7830–7843 (2010).
156. Kim, S. *et al.* CHARMM-GUI ligand reader and modeler for CHARMM force field generation of small molecules. *J. Comput. Chem.* **38**, 1879–1886 (2017).
157. Jo, S., Kim, T., Iyer, V. G. & Im, W. CHARMM-GUI: A web-based graphical user interface for CHARMM. *J. Comput. Chem.* **29**, 1859–1865 (2008).
158. Feller, S. E., Zhang, Y., Pastor, R. W. & Brooks, B. R. Constant pressure molecular dynamics simulation: The Langevin piston method. *J. Chem. Phys.* **103**, 4613–4621 (1995).
159. Darden, T., York, D. & Pedersen, L. Particle mesh Ewald: An N·log(N) method for Ewald sums in large systems. *J. Chem. Phys.* **98**, 10089–10092 (1993).

160. McGibbon, R. T. *et al.* MDTraj: A Modern Open Library for the Analysis of Molecular Dynamics Trajectories. *Biophys. J.* **109**, 1528–1532 (2015).
161. Waskom, M. *et al.* seaborn: v0.7.1 doi:10.5281/ZENODO.54844 (2016).
162. Liu, Y., Schmidt, B. & Maskell, D. L. MSAProbs: multiple sequence alignment based on pair hidden Markov models and partition function posterior probabilities. *Bioinformatics* **26**, 1958–1964 (2010).
163. Robert, X. & Gouet, P. Deciphering key features in protein structures with the new ENDscript server. *Nucleic Acids Res.* **42**, W320-4 (2014).
164. Li, P., Wang, K., Salustros, N., Grønberg, C. & Gourdon, P. Structure and transport mechanism of P5B-ATPases. *Nat. Commun. 2021 121* **12**, 1–8 (2021).
165. Ho, B. K. & Gruswitz, F. HOLLOW: Generating accurate representations of channel and interior surfaces in molecular structures. *BMC Struct. Biol.* **8**, 49 (2008).
166. Drew, D. & Boudker, O. Shared Molecular Mechanisms of Membrane Transporters. *Annu. Rev. Biochem.* **85**, 543–572 (2016).
167. Liu, F. *et al.* Molecular Structure of the Human CFTR Ion Channel Article Molecular Structure of the Human CFTR Ion Channel. *Cell* **169**, 85–95 (2017).
168. Number of Released PDB Structures per Year. https://www.rcsb.org/stats/all-released-structures.
169. Kühlbrandt, W. The resolution revolution. *Science* **343**, 1443–1444 (2014).
170. Chen, X. *et al.* Cryo-EM structures and transport mechanism of human P5B type ATPase ATP13A2. *Cell Discov.* **7**, 1–12 (2021).
171. Tillinghast, J., Drury, S., Bowser, D., Benn, A. & Lee, K. P. K. Structural mechanisms for gating and ion selectivity of the human polyamine transporter ATP13A2. *Mol. Cell* **81**, 4650-4662.e4 (2021).
172. Jin, F. *et al.* The structure of MgtE in the absence of magnesium provides new insights into channel gating. *PLOS Biol.* **19**, e3001231 (2021).
173. Huang, Y. *et al.* Structural basis for the Mg^{2+} recognition and regulation of the CorC Mg^{2+} transporter. *Sci. Adv.* **7**, 6140 (2021).
174. Komuro, Y., Re, S., Kobayashi, C., Muneyuki, E. & Sugita, Y. CHARMM force-fields with modified polyphosphate parameters allow stable simulation of the ATP-bound structure of Ca^{2+}-ATPase. *J. Chem. Theory Comput.* **10**, 4133–4142 (2014).
175. Rui, H., Das, A., Nakamoto, R. & Roux, B. Proton Countertransport and Coupled Gating in the Sarcoplasmic Reticulum Calcium Pump. *J. Mol. Biol.* **430**, 5050–5065 (2018).
176. Fernández-De Gortari, E. & Espinoza-Fonseca, L. M. Preexisting domain motions underlie protonation-dependent structural transitions of the P-type Ca^{2+}-ATPase. *Phys. Chem. Chem. Phys.* **19**, 10153–10162 (2017).

177. Nagarajan, A., Andersen, J. P. & Woolf, T. B. The role of domain: domain interactions versus domain: water interactions in the coarse-grained simulations of the E1P to E2P transitions in Ca-ATPase (SERCA). *Proteins* **80**, 1929–1947 (2012).
178. Kobayashi, C., Matsunaga, Y., Jung, J. & Sugita, Y. Structural and energetic analysis of metastable intermediate states in the E1P–E2P transition of Ca^{2+}-ATPase. *Proc. Natl. Acad. Sci. U. S. A.* **118**, (2021).
179. Kjelstrup, S. & Lervik, A. The energy conversion in active transport of ions. *Proc. Natl. Acad. Sci.* **118**, (2021).

Original papers

Tomita, A., Zhang, M., Jin, F., Zhuang, W., Takeda, H., Maruyama, T., Osawa, M., Hashimoto, K., Kawasaki, H., Ito, K., Dohmae, N., Ishitani, R., Shimada, I., Zhiqiang, Y., Hattori, M., & Nureki, O. (2017). ATP-dependent modulation of MgtE in Mg^{2+} homeostasis. *Nature communications* **8**, 148.

Tomita, A., Daiho, T., Kusakizako, T., Yamashita, K., Ogasawara, S., Murata, T., Nishizawa, T. & Nureki. O. (2021). Cryo-EM reveals mechanistic insights into lipid-facilitated polyamine export by human ATP13A2. *Molecular Cell* **81**, 4799–4809.